BEEM IMAGING AND SPECTROSCOPY OF BURIED STRUCTURES IN SEMICONDUCTORS

V. NARAYANAMURTI, M. KOZHEVNIKOV

Gordon Mckay Laboratory of Applied Science, Harvard University, 9 Oxford Street, Cambridge, Massachusetts 02138, USA

N·H

ELSEVIER

AMSTERDAM – LONDON – NEW YORK – OXFORD – PARIS – SHANNON – TOKYO

BEEM imaging and spectroscopy of buried structures in semiconductors

V. Narayanamurti*, M. Kozhevnikov

Gordon Mckay Laboratory of Applied Science, Harvard University, 9 Oxford Street, Cambridge, MA, 02138, USA

Contents

* Corresponding author. Tel.: 617-495-5829; fax: 617-496-5264.

E-mail addresses: venky@deas.harvard.edu (V. Narayanamurti), mkozhevn@deas.harvard.edu (M. Kozhevnikov).

Abstract

Ballistic Electron Emission Microscopy (BEEM) has been shown to be a powerful tool for nanometer-scale characterization of the spatial and electronic properties of semiconductor structures. In this article, we will discuss general aspects of BEEM experiment and theory in true ballistic and quasi-ballistic hot carrier transport. We will review the current state and recent progress in the use of the BEEM imaging and spectroscopy to study metal-semiconductor and metal-insulator-semiconductor interfaces, buried semiconductor heterojunctions and novel quantum objects. Various theoretical BEEM models are discussed, and their ability to describe BEEM experiments is examined. Special attention is drawn to the role of the electron scattering in the metal base layer, at the metal–semiconductor interface and in the semiconductor heterostructure on BEEM spectra. © 2001 Elsevier Science B.V. All rights reserved.

1. Introduction

The current trend of developing small-size electronic devices requires high resolution in the characterization and control of metal–semiconductor (m–s) heterostructures. To improve device characterization and performance, and for a better understanding of the basic physics of semiconductor interfaces, there is an increasing demand for nanometer-scale probes, all the way down to the atomic level, of the spatial and electronic properties of m–s junctions and semiconductor heterostructures.

Among the variety of scanning probe microscopy techniques, Ballistic Electron Emission Microscopy (BEEM), a three-terminal modification of Scanning Tunneling Microscopy (STM), is a powerful low-energy tool for nondestructive local characterization of semiconductor heterostructures. The STM metal tip (emitter) injects electrons across the tunneling gap into the metal (base) layer deposited on a semiconductor. A third terminal on the sample back is used to collect those electrons, which traverse the interface. A schematic of the BEEM experimental set-up is shown in Fig. 1. In the conventional STM study of semiconductors, the tunneling is usually between the metal tip and the doped semiconductor layers. In contrast, the BEEM technique provides the carrier filtration at the m–s interface, since only the electrons that can traverse the metal base and overcome the Schottky barrier will be collected at the semiconductor substrate (collector). A schematic band diagram for BEEM is shown in Fig. 2. In this way, the energy and angular distribution of hot electrons can be controlled independently on the semiconductor structure by simply varying the tip potential. In addition, the BEEM technique holds the extremely high spatial resolution of the scanning tunneling microscopy ($\sim$few nm). Thus BEEM provides, in complement to the surface morphology, a combination of low-energy electron microscopy and spectroscopy with high-spatial and energy resolution.

Since the pioneering work of Kaiser and Bell [1], applications of BEEM to various semiconductor surfaces and interfaces have already produced many interesting results (early BEEM research was previously reviewed in Refs. [2,3]). It was shown that the magnitude of the transmitted current into the substrate depends strongly on the local properties of the interface [4,5] as well as the scattering properties of the overlying metal film [6,7]. In epitaxial $CoSi_2/Si$ structures, atomic BEEM resolution was observed [8], and this effect of electron beam focusing was attributed to be due to the silicide band structure [9]. The capability of BEEM to probe the electronic properties of semiconductors on the local scale has been demonstrated in several systems including InAs/GaAs [10], Si p–n junction [11] and SiGe strained layers [12]. It was shown that the high-bias BEEM spectroscopy could be used as a local density-of-states (DOS) spectroscopy in semiconductors [13,14]. By using BEEM, Schottky barrier and band structure characterization was conducted in technologically important semiconductors such as GaP [7], GaInP [15,16], GaN [17–19], GaAsN [20] and SiC [21,22].

Although the BEEM technique was originally invented as a unique microscopic and spectroscopic method to probe the Schottky barriers on a local scale [23], it has been successfully used to study the electronic properties of *buried* heterojunctions [24]. BEEM was successfully applied to metal–insulator–semiconductor (MIS) structures to study the transport related oxide properties on a microscopic scale in buried CaF_2/Si [25] and SiO_2/Si [26]. In SiO_2-based metal-oxide–semiconductor (MOS) structures, BEEM was used to study the quantum interference effects and trapped charge distribution that is very important for the operation of MOS field-effect transistors
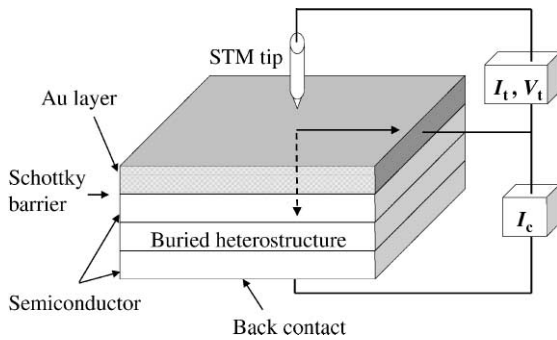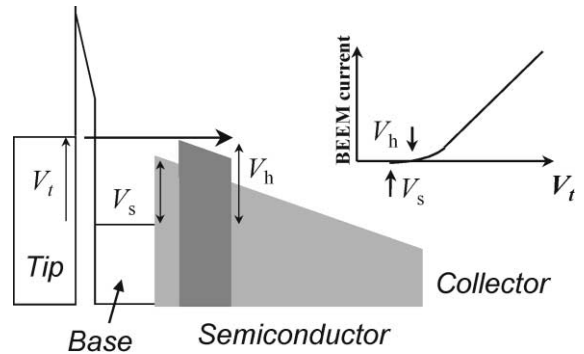
Fig. 1. A schematic of BEEM experimental setup.

Fig. 2. Schematic band diagram of a BEEM experiment. Inset shows a generic BEEM spectrum.

[27,28]. Recently, significant progress was accomplished in establishing BEEM as an effective method for measuring semiconductor heterojunction offsets [29–31], for measuring resonant transport through single barrier [32], double-barrier [33] and superlattice resonant tunneling heterostructures [34,35], for investigation of hot carrier transport in low-dimensional nanostructures such as quantum wires [36,37] and quantum dots [38–40], as well as for imaging of defects buried below the surface [41–43]. In order to amplify the BEEM capabilities, some apparatuses are operated in ultra high vacuum (UHV) [8,25,44] (the main advantages are cleaning of the semiconductor surface, metal deposition under UHV conditions, Schottky contacts and STM tips by using the metals and semiconductors that are unstable towards oxide formation) and at low (helium) temperatures [45,46] (the main advantages are enhanced energy resolution of BEEM and reduction of thermal noise and lateral drift).

2. BEEM transport

2.1. General BEEM description

The spectral shape of the BEEM current has to be known in order to derive a Schottky barrier height or heterostructure band alignment. A number of the theoretical models have been proposed to describe the BEEM spectrum in the threshold region. Two commonly used models, based on a planar tunneling formalism [47] and on transverse momentum conservation at the m–s interface, are the Bell-Kaiser (BK) model [1] and the Ludeke-Prietsch (LP) model [48]. In the BK model, for parabolic energy bands in the semiconductor, the near-threshold BEEM current varies as $I_c \sim (V_t - V_s)^2$, where V_t is the applied tip-to-base voltage and V_s is the Schottky barrier magnitude [2]. This model was found to adequately describe the BEEM spectra for the Au/Si system [1]. In the LP model, the theory is extended to include the energy-dependent electron mfp in the metal base layer and quantum mechanical transmission (QMT) at the m–s interface. The near-threshold dependence $I_c \sim (V_t - V_s)^{5/2}$ in this model differs somewhat from the BK model

result. It was reported in Ref. [48] that the best fit for metal/GaP BEEM data was obtained with the 5/2-power law. Also, the BEEM spectra of Au/GaAs were fitted by the 5/2-power law [49]. However, even though the BEEM correction due to the QMT is important, the quantitative difference between the BK and the LP models is comparable with the experimental error, and both of them can frequently fit the experimental data reasonably well [2,29,50,51]. Note that the assumption about $I_c \sim (V_t - V_s)^2$ (or $I_c \sim (V_t - V_s)^{5/2}$ in the case of the square-root contribution of the QMT) dependence is valid only close to threshold, while increasing deviations are expected for higher tip-to-base voltages. The main mechanisms responsible for these deviations are a voltage-dependent energetic distribution of the tunneling current, carrier scattering in the metal overlayer as well as carrier scattering and impact ionization in the semiconductor substrate [2].

A method for computation of the quantum mechanical transmission probability (QMTP) from plane interfaces was presented in Ref. [52]. This method was applied to calculate the QMTP at the metal/Si(100) and metal/Si(111) interfaces at the Schottky barrier maximum. It was shown that the QMTP depends on the crystal orientation and the location of the band maximum. Later, a more accurate BEEM model was developed [53,54] and was compared with the experimental results for Au/Si(100) [55] and Au/Si(111) [56,57]. The model employs an effective mass approach generalized to permit for non-diagonal mass tensors and for indirect conduction band minima. The impact of this quantum mechanical modeling on the BEEM current has been probed by Monte Carlo simulations (adopting the course developed in Ref. [56]) using bulk material parameters for all layers, and an average reduction of the BEEM current of 20% was obtained.

Recently, an extension of the BEEM theory for the case of buried heterostructures, was performed by Smith and Kogan (SK) [58]. In the SK model, the authors considered the QMT at the buried heterojunction interface in addition to the m–s interface. In addition, the authors have shown that the second voltage derivative of the BEEM spectra should reflect the transmission probability of the semiconductor heterojunction, and, therefore, is very informative for the characterization of the structure. For the case of the GaAs/AlGaAs systems [5,33], the experimentally obtained second derivatives (SD) of the BEEM current give peaked structure, which could be associated with the various calculated heterostructure transmission channels.

In the generalized BEEM description, four consecutive processes are usually considered: (i) tunneling from the tip to the metal base layer, (ii) hot electron transport through the metal base layer, (iii) transmission across the m–s interface (carriers must have enough energy and appropriate momentum in order to cross the Schottky barrier and reach the semiconductor), and (iv) transport inside the semiconductor that can include the transmission across the heterojunction interfaces. For the case of a buried heterostructure, only those electrons that pass through the m–s interface and are also transmitted by the heterostructure contribute to the collector current. In this case, the collector current can be written as a product of the electron flux distribution right before the semiconductor and the transmission coefficients of the m–s interface and heterostructure [59]:

$$I_c = eA \sum_{\mathbf{k}^t} F_\perp^t(\mathbf{k}^t) T^{V_t}(\mathbf{k}^t, \mathbf{k}^b) D(\mathbf{k}^b) T^i(\mathbf{k}^b, \mathbf{k}^{sb}) T^h(\mathbf{k}^{sb}) , \tag{1}$$

where A is the sample area, e is the electron charge, $F_\perp^t$ is the surface normal electron flux in the tip due to the state labeled by wavevector $\mathbf{k}^t$, $T^{V_t}(\mathbf{k}^t, \mathbf{k}^b)$ is the voltage-dependent transmission coefficient for the state in the STM tip with wavevector $\mathbf{k}^t$ to tunnel through the vacuum into the base

state with wavevector k^b (determined from k^t by energy and surface normal wavevector conservation) calculated using the WKB approximation. $D(k^b) = e^{-\delta_b/\xi}$ is the probability of the electron traversing the base without scattering, where δ_b is the thickness of the base and ξ is the mean free path in the base. The product $F^t_\perp(k^t)T^V(k^t, k^b)D(k^b)$ is the interface normal electron flux incident on the m–s interface due to the state in the STM tip labeled by k^t. $T^i(k^b, k^{sb})$ is the transmission coefficient for the m–s interface and $T^h(k^{sb})$ is the transmission coefficient for the semiconductor heterostructure.

Note that, since there is a certain electron filtration for each of the aforementioned four steps, the collected BEEM current is typically smaller than the tunneling current by several orders of magnitude, depending on the structure under study. Also, applying forward tip-to-base bias (the tip is more positive than the metal base layer), electron tunneling is possible from the base to the tip, creating the ballistic hole distribution in the base. Therefore, allowing the collector to be a p-type semiconductor substrate, one can collect the above-threshold hole current in a manner quite similar to the case of electron injection. In this way, the BEEM theory can be extended for the case of hole injection, with a slight difference that the energy distribution of ballistic holes are peaked towards the base Fermi level. The details of the ballistic hole emission microscopy (BHEM) and spectroscopy (BHES) can be found, for example, in Refs. [60,61].

2.2. Impact ionization effect in semiconductors

Impact ionization in the semiconductor can contribute to the BEEM current at high voltages if energy loss in the metal film is weak so that the electrons reach the interface with the energy above the threshold for impact ionization in the semiconductor [62]. An additional onset of impact-ionized electrons in the BEEM current was observed at $V_t \sim 3V$ in Au/Si [51] and CoSi$_2$/Si [63]. For Au/GaP [7], this effect was found to be important in describing the BEEM data for 12 Å Au film whereas for 50 Å film, impact ionization was not important, due to strong inelastic scattering of hot electrons in the metal layer at high voltages.

The effect of impact ionization was studied in NiSi$_2$/Si(111)7 × 7 over a wide energy range (up to $V_t \sim 8V$) [44,64]. To eliminate the effect of elastic and inelastic scattering in the metal film, the BEEM spectra were taken in pinholes of thin NiSi$_2$ films where the modified Si(111)7 × 7 surface being an ultrathin metallic layer. Fig. 3 shows a representative BEEM spectrum taken in a pinhole of a 22 Å thick B-type NiSi$_2$ film. The spectrum is decomposed into a primary- and a secondary-electron part resulting from impact ionization. The quantum yield of impact ionization in Si (curve (c) in Fig. 3) was determined by decomposition of the BEEM current into secondary- and primary-electron contributions, and a good agreement with Monte Carlo simulations [65] was found. In addition, it was found that the secondary electron current starts at $eV_t \approx 1.5E_g$, where E_g is the semiconductor bandgap, in accordance with the theoretical predictions [66].

2.3. Image potential effect

The effect of phonon scattering in the semiconductor on the ballistic transport across the Schottky barrier was studied theoretically [67] and experimentally [55,68]. The authors distinguished between the metallurgical m–s interface and the Schottky barrier maximum resulting from the image potential effect. In this way, the Schottky barrier is not spatially abrupt, but exhibits
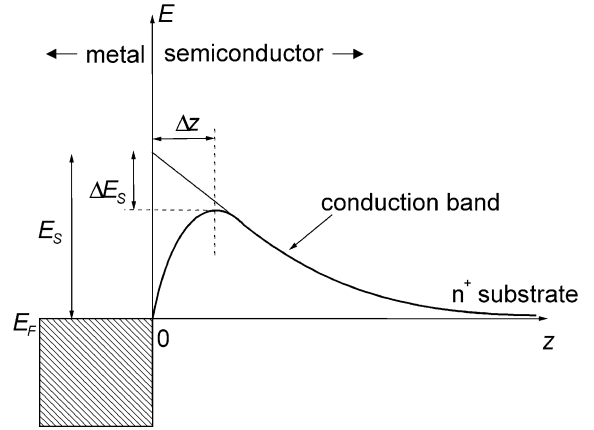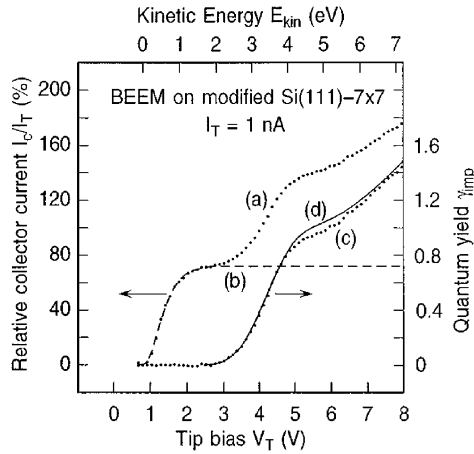
Fig. 3. BEEM spectrum for a 22 Å B-type NiSi$_2$ layer on Si(1 1 1)7 × 7 taken within a pinhole, curve (a). The dashed curve (b) is a fitted spectrum of the primary electron current. The difference (a)–(b) represents the secondary electron current arising from electron–hole pairs generated through impact ionization. This difference divided by (b), shown as the dotted curve (c), is the experimentally determined quantum yield γ_{imp}. The solid curve (d) is a calculation based on the model in Ref. [66] (from Ref. [64]).

Fig. 4. The effect of the image potential on the Schottky barrier lowering and on the shift of the potential maximum of the barrier.

a smooth hydrogen-like variation (see Fig. 4). In the case of band bending, this results in a lowering of the effective barrier height by $\Delta E_s \approx \sqrt[4]{e^6 N_D E_s/(8\pi^2(\varepsilon_s\varepsilon_0)^3)}$, where N_D is the doping concentration of the semiconductor, and in the barrier maximum shifting away from the interface by $\Delta z \approx \sqrt[4]{e^2/(2^{10}\pi^2\varepsilon^s\varepsilon N E_s)}$ [2]. Electrons with energies just over the threshold for transmission that excite phonons in the region before the Schottky-barrier maximum are expected to have a high probability of reentering the metal [55]. It was shown that while QMTP alone adds $\sim E^{1/2}$ dependence, the combined effect of optical phonon scattering and quantum mechanical scattering gives a much weaker energy dependence than for either effect alone for the cases of Au/Si and Au/GaAs at both $T = 77$ and 300 K [67].

While the image potential effect on the effective Au/GaAs Schottky barrier is mostly insignificant, its effect on the barrier maximum shift has much more important consequences. Indeed, assuming $N_D = 5 \times 10^{15}$ cm^{-3}, $\varepsilon_s = 12$, $E_s = 0.95$ eV at $T = 300$ K for a typical Au/GaAs Schottky contact, we obtain $\Delta E \approx 20$ meV and $\Delta z \approx 30$ Å. ΔE_s of 20 meV will not noticeably affect our measurements since it is only $\sim 2\%$ of the Schottky barrier height and is comparable with the experimental error of ~ 30 meV. On the other hand, Δz of 30 Å is comparable, and even longer, than the expected mfp length for the X-electrons (~ 10 Å at $T = 300$ K [43]), and, therefore, can affect this transport channel very effectively. It was confirmed in our BEEM study of the Au/GaAs system, where a strong attenuation of the electron transport through the X valley was observed [5].

The effect of phonon scattering beyond the Schottky-barrier maximum on the magnitude of the BEEM current depends on the build-in electric field strength, i.e. on the doping density of the

semiconductor. The effect of the image potential on the Schottky barrier reduction under reverse bias applied was studied in Au/Si [68]. The increase of the collection efficiency under applied reverse-bias ($\sim 10\%$ increase of the collection efficiency at a 3 V reverse-bias voltage) was explained by a reduction of the energy-dependent backscattering of electrons in the depletion layer. In another study, it was also shown that the electron backscattering into the metal due to the interactions with phonons inside the depletion layer near the interface is very important for an adequate description of the BEEM spectra in the Au/Si system [69].

2.4. Carrier scattering at the metal–semiconductor interface

While the original model has been subsequently generalized to include effects such as quantum mechanical transmissions at the m–s interface and in buried semiconductor heterostructures, the assumption of transverse wavevector conservation at the m–s interface has been mostly maintained. Using such models good fits to threshold data have been achieved for a number of metal/semiconductor systems. However, even if the assumption of transverse wavevector conservation at the metal-semiconductor interface may be optimistically justified at epitaxial interfaces such as $CoSi_2/Si$ and $NiSi_2/Si$, it is very questionable for the case of nonepitaxial m–s interfaces where the interface is far from the atomically abrupt, such as Au/GaAs or Au/Si that are prototypes for nonepitaxial metal interfaces on direct and indirect bandgap semiconductors, respectively. In this case, the carrier transport across the m–s interfaces may be quasi-diffusive rather than ballistic due to the carrier scattering at these interfaces.

2.4.1. Nonepitaxial Au/Si and Au/GaAs

Tunneling predominantly injects forward-directed electrons with small interface parallel wavevector components into the metal film. As shown in Fig. 5, for Si(111), for which all of the CBM have large parallel wavevectors, there are no states available for transmission at the center of the interface Brillouin zone (BZ), while for Si(100), for which two of the conduction valleys have zero parallel wavevector, there are states available both at the zone center and in off-axis band minima. Thus, the Au/Si(111) BEEM current is expected to be much weaker than that for Au/Si(100) if the electron transport is essentially ballistic through the m–s interface [59]. This predicted difference was not confirmed in the BEEM experiments. A deviation from the ballistic picture was experimentally observed for Au/Si [1,70,71], and Pd/Si [13] systems, where essentially the same BEEM spectra were observed for Si(001) and Si(111) substrates (see Fig. 6(a)), in conflict with conventional BK theory which predicts a significantly different spectra for the two orientations.

With the same argumentation for the case of Au/GaAs(100), the calculated current into valleys with zero parallel wavevector at the minimum (e.g., the Γ valley), is predicted to be much larger than the calculated current into valleys with large parallel wavevector at the minimum (e.g., the L valleys) [59]. In BEEM experiments on Au/GaAs, three thresholds were observed and were attributed to the electron transmission into Γ, L and X valleys [29,49]. Six fitting parameters were commonly used to describe the BEEM measurements in GaAs (AlGaAs), one threshold energy and one scaling factor for each of the three valleys. And though the comparison of the multiple BEEM thresholds with the expected composition dependence of the GaAs Γ, L, and X conduction band position yielded reasonably good agreement over the entire compositional range, the scaling factors differ significantly from the expected ones, as shown in Fig. 6(b). In fact, the Γ channel
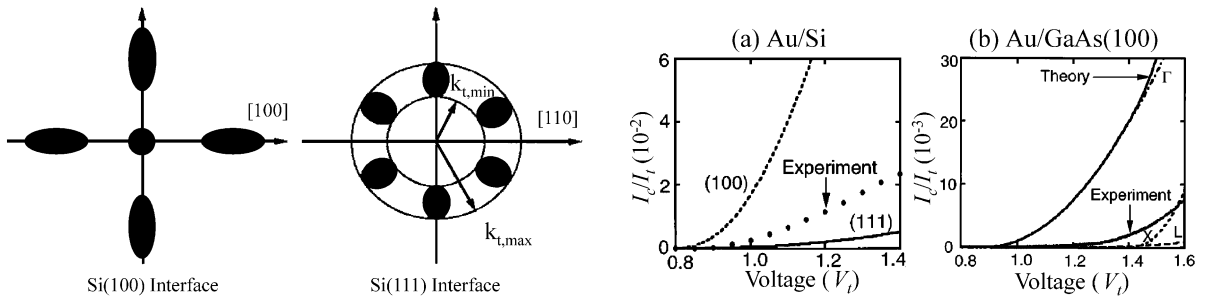
Fig. 5. Schematic representation in k space of the projection of the six Si CBM onto the (1 0 0) and (1 1 1) interfaces. The transverse wave vectors of the incident electrons must lie within the shaded regions in order to satisfy energy and transverse momentum conservation laws. It is clear from the diagram that for energies just above the CBM, electrons with near zero transverse momenta can cross a Si(1 0 0) interface but are reflected back into the metal at a Si(1 1 1) interface [72].

Fig. 6. (a) Comparison of the calculation for Au/Si(1 0 0) (dashed line) and Au/Si(1 1 1) (solid line) with the experimental results for Au/Si of Refs. [86,87]. These measurements were made on Au/Si(1 1 1) but measurements for Au/Si(1 0 0) are very similar to those for Au/Si(1 1 1) (see Refs. [70,102]). (b) Comparison of the calculation for Au/GaAs(1 0 0) with the experimental results of Ref. [29]. The dot-dashed line shows the Γ, the long-dashed line shows the L, the short-dashed line shows the X contribution to the BEEM current, and the solid line shows the sum of the three [85].

contribution to the collector current was found to be much smaller than the L channel contribution [1,29,49]. The BEEM current into the L valley was explained in terms of possible breakdown of the transverse momentum conservation at the m–s interface [5,29,49]. In Au/GaAs/AlAs [49], two thresholds were associated with the contribution from the X and L valleys of AlAs. Complementary Monte Carlo simulations give a good agreement with the experiment if one assumes transverse momentum conservation at the GaAs/AlAs interface and its non-conservation at the Au/GaAs interface.

2.4.2. Epitaxial $CoSi_2$/Si and $NiSi_2$/Si

Epitaxial metallic disilicide-silicon films such as $NiSi_2$ and $CoSi_2$ on Si can be grown with atomically abrupt and structurally perfect interfaces either by the Tung template method [72,73] or by stoichiometric coevaporation of Co and Si at room temperature and subsequent annealing [74,75]. In these systems, the role of the transverse momentum conservation at the m–s interface was explicitly studied in a number of BEEM experiments. While the assumption of transverse momentum conservation was justified in some cases, a certain deviation from the behavior, expected if transverse momentum $k_{||}$ is conserved, was observed in other cases.

The BEEM current depends strongly not only on the Schottky barrier but also on the electronic band structure of the material under study. Based on their band structure calculations, Stiles and Hamann [76] have predicted a delayed onset of the BEEM current for the $CoSi_2$/Si(111) system where there are no states in the silicide with $k_{||}$ large enough to match the silicon CBM up to 0.85 eV above E_F (Schottky barrier for this system is ~ 0.66 eV). Fig. 7 shows schematically part of the distribution of states in both materials in terms of their energy and parallel wavevector in the
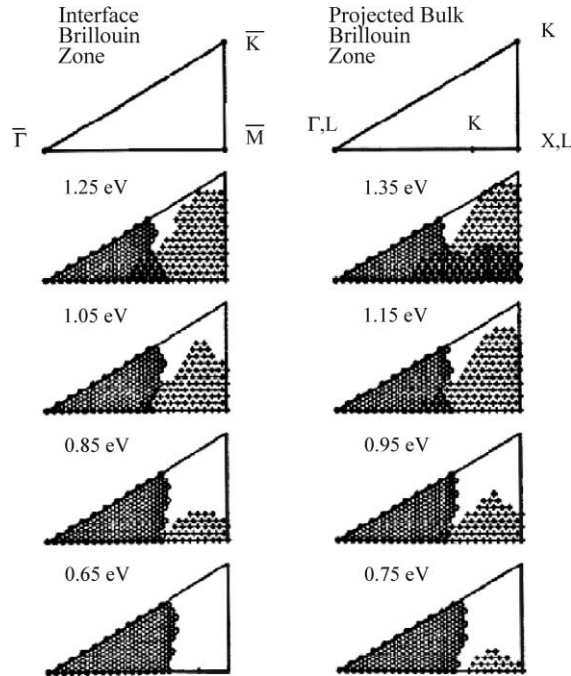
Fig. 7. Phase space for electron transmission through a $CoSi_2/Si(1\,1\,1)$ interface. The panels show the irreducible wedge of the interface Brillouin zone of both $CoSi_2$ and the Si. At each parallel wave vector used in the calculation there is an open circle if there is at least one state at that energy in the $CoSi_2$ and a plus if there is at least one state in the Si. If there is a state in both, the open circles fill in and become closed circles [76].

interface BZ. In agreement with this prediction, Kaiser et al. [74] have measured the BEEM spectra in this system in a glove box and found a delayed onset of ~ 0.85 eV, close to the calculated value. The observation of this effect was considered as a strong evidence for the transverse momentum conservation in the $CoSi_2/Si(111)$ system.

Later, Sirringhaus et al. [75,77,78] observed individual interfacial dislocations by conducting the BEEM imaging and spectroscopy on strain-relaxed $CoSi_2$ layers. The dislocations were also observed in STM images because the strain field around each dislocation at the interface causes a distortion of the surface. The sharp BEEM dislocation profiles (~ 10 Å resolution for a 25 Å $CoSi_2$ film) in $CoSi_2/Si(111)$ imply that the electron transport in the silicide is essentially ballistic. This was also corroborated by the observation of the quantum size effect [8,79]. Thus it was concluded that most of the electrons reach the $CoSi_2/Si$ interface with $k_{||} \sim 0$. The increase of the BEEM current on the dislocation was explained by increased interfacial scattering at the dislocation core that supplies electrons with a large transverse momentum to transmit into the silicon CBM. This scattering broadens the $k_{||}$ momentum distribution, and thus facilitates the electron transmission. In addition, if $k_{||}$ is conserved away from dislocations, the electron scattering will not be beneficial in the case of positive biasing of $CoSi_2/p$-$Si(111)$, where holes are injected into the zone-centered valence band. In accordance with expectations, in the latter case the BEEM current at dislocations and at isolated defects was lower than that in a defect-free region [80].
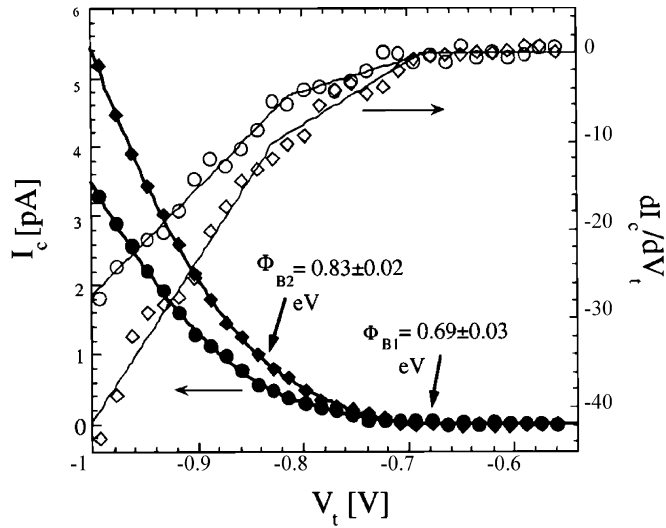
Fig. 8. Average of 14 BEEM spectra, and corresponding first derivative spectra, taken on top of an interfacial point defect (diamonds) and in a defect-free area (circles). The spectra were measured with a tunneling current of $I_t = 20$ nA, and are normalized to $I_t = 1$ nA [82].

However, in all in-situ measurements of Sirringhaus et al. [81], a homogeneous BEEM onset of ∼0.66 eV was found (corresponding to the Schottky barrier) in dislocation- and defect-free regions, and it was explained by a small but finite scattering probability everywhere at the epitaxial $CoSi_2/Si$ interface. Later, better-spatially resolved BEEM measurements (where I_t was increased to 20 nA to allow less averaging to obtain a high signal-to-noise ratio), revealed that both onsets (∼0.69 and ∼0.83 eV) should be invoked to fit the BEEM spectra [82], as shown in Fig. 8. One can see from Fig. 9 that the amplitude weight of the lower onset is highly increased in the presence of the interfacial defects, indicating an enhanced scattering probability. Also, in the case of epitaxial $CoSi_2/Si(111)$ and $CoSi_2/Si(100)$, similar BEEM current magnitude at the near threshold region was observed [41]. This discrepancy from the behavior expected if $k_{||}$ is conserved was explained by the combined effect of small interface transmission at the $CoSi_2/Si(100)$ interface and the broad momentum distribution injected by the atomically sharp STM tip.

Another epitaxial system with an abrupt interface is $NiSi_2/Si(111)$. In contrast to $CoSi_2/Si(111)$, in this system there is overlap between $NiSi_2$ and Si states at all energies above the Schottky barrier, and transverse momentum conservation cannot be manifested just from a shifted threshold position. However, if transverse momentum is conserved, a very soft threshold is expected for electron transport through the X valley with large parallel wavevector, and, indeed, a soft threshold was found in Ref. [44]. Another manifestation of transverse momentum conservation in $NiSi_2/Si(111)$ is the increase of BEEM current at the edges of the Si triangles on top of the $NiSi_2$ terraces [44]. In the presence of a step (at the edges of the islands) the injected electrons are dispersed, and the angular distribution is expected to be broader thus leading to a larger transmission. In another study of epitaxial $NiSi_2/Si(111)$ system, however, the deviations of the transmittance spectra of $NiSi_2/Si(111)$ from the theoretical predictions of Ref. [83] were observed

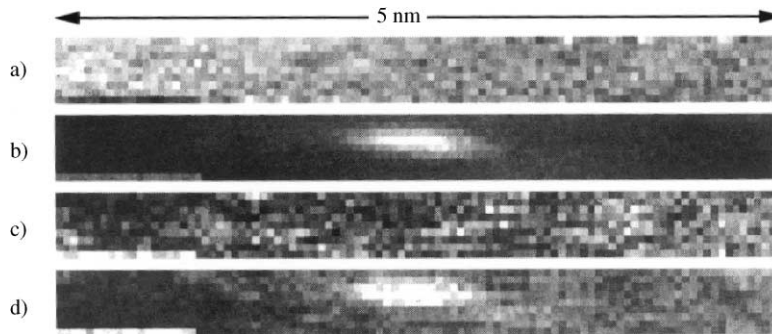Fig. 9. Topographic STM image (a) and corresponding BEEM image (b) obtained for $V_t = 1.7$ V and $I_t = 20$ nA. A total of 100×9 BEEM spectra was recorded at a nominal spacing of 0.05 nm. The elongated shape of the point defect is due to microscope drift during the measurement. Each spectrum was fitted to $I_c(V_t) = R_1(V_t - \Phi_{B1})^2 + R_2(V_t - \Phi_{B2})^2$ keeping the barriers fixed at $\Phi_{B1} = 0.69$ eV and $\Phi_{B2} = 0.83$ eV. The scale factor R_2 deduced from the fit is shown in (c). Similarly, the scale factor R_1 is displayed in (d). Gray-scale ranges were 0.1 nm, $\Delta I_c = 200$ pA, $R_2 = 28–84$ pA/(eV)^2, and $R_1 = 14–42$ pA/(eV)^2 in (a), (b), (c) and (d), respectively [82].

and were attributed to the elastic scattering in the silicide layer [71]. It was found that while the cross-sectional TEM and X-ray scattering data show good epitaxial interfaces and silicide layers, a 10% scattering in the silicide should be assumed (in the isotropic point defect scattering model) to describe the experimental BEEM data. It was concluded that scattering broadens the momentum distribution and thus averages and smoothes the effect of band structure predicted by theory.

2.4.3. Scattering models

Several models were employed to describe the observed deviation from the ballistic picture in BEEM experiments on metal/Si and metal/GaAs systems.

Ke et al. [49] used a Monte Carlo technique to simulate the I–V curve of the BEEM measurements in Au/GaAs and Au/GaAs/AlAs. Four physical processes were taken into account: electron tunneling from the tip to metal surface, elastic and inelastic scattering in the metal base layer, electron transmission through the interface and impact ionization inside the semiconductor depletion layer. It was shown that the experimentally observed large BEEM current through the L valley can be explained only assuming strong scattering at the m–s interface. Good agreement between Monte Carlo simulations and experimental data was obtained by assuming the square-root energy dependence of the electron transmission at the interface for all valleys, regardless of their projection in the (001) direction.

Guthrie et al. [84] have developed a dynamic BEEM model, where in addition to directional (kinematic) constraints, the amplitude effects were incorporated by considering the quantum mechanical transmittance and elastic scattering in the base and at the m–s interface. It was shown that as the scattering probability increases (i.e. a planar distribution is replaced by an isotropic distribution) the Au/Si(111) BEEM current increases whereas the Au/Si(100) current decreases. In addition, the BEEM spectral shape is also sensitive to the scattering probability. The model gives a good fit to the experimental data for both Au/Si(111) and Au/Si(100) if the scattering probability at the m–s interface exceeds 50%. Also, including the effect of an energy-dependent quantum

transmittance improves the fit in the near-threshold region. In the case of Au/GaAs(100), the BEEM current through the Γ valley decreases strongly as the scattering strengthens, without any spectral shape change. From fitting the experimental data, it was difficult to determine the extent of the electron scattering since the BEEM spectral shape is not sensitive to the scattering, and the scaling factor can be strongly modified by the surface passivation and the effect of electron scattering in the metal overlayer.

To analyze quantitatively the experimental data, the m–s interface-induced scattering (MSIS) model was proposed in Ref. [85]. The authors showed that the experimental data for Au/Si and Au/GaAs systems could be fitted only by taking into account of the strong carrier scattering at the m–s interface. Recently, to quantitatively analyze the electron scattering at the m–s interface, this model was modified to include anisotropy of the electron effective mass, the energy dependence of the electron mfp in the metal base, and finite temperature [59]. In this model, the conduction process is described by carrier multivalley transport with corrections due to the scattering at the m–s interface, which depends on the m–s scattering probability. When interface scattering is considered, the BEEM current is given by [59]

$$I_c = eA \sum_{\boldsymbol{k}^t} F_\perp^t(\boldsymbol{k}^t) T^{V_t}(\boldsymbol{k}^t, \boldsymbol{k}^b) D(\boldsymbol{k}^b)$$

$$\times \left[\left(1 - \sum_f P_{\boldsymbol{k}^b, \boldsymbol{k}^f} \right) T^i(\boldsymbol{k}^b, \boldsymbol{k}^{sb}) T^h(\boldsymbol{k}^{sb}) + \sum_f P_{\boldsymbol{k}^b, \boldsymbol{k}^f} T^i(\boldsymbol{k}^b, \boldsymbol{k}^{sb}) T^h(\boldsymbol{k}^{sb}) \right], \tag{2}$$

where $P_{\boldsymbol{k}^b, \boldsymbol{k}^f}$ is the probability for the electron with the wavevector $\boldsymbol{k}^b$ to be scattered into the state labeled by the wavevector $\boldsymbol{k}^f$. The first and second terms in brackets correspond to electrons that are not scattered and that are scattered, respectively. In the weak scattering limit, the MSIS model is essentially equivalent to the SK model.

In this model, if scattering at the m–s interface is strong, the injected electron flux is redistributed, and valleys with zero interface transverse wavevector at their energy minimum are not preferentially weighted. Instead the weighting goes like the density of final states for the scattering process. Fig. 10 compares the calculated BEEM current in the strong and in the weak scattering limits for Au/Si with the experimental results of Refs. [86,87]. One can see that the experimental data can be described adequately without fitting parameters only in the strong scattering limit. In BEEM on Au/GaAs, the calculated Γ channel contribution is much larger than the L channel contribution to the collector current in the weak scattering limit, whereas the L channel contribution is much larger than the Γ channel contribution in the strong scattering limit (see Fig. 11). Scaled threshold shapes are similar in the weak and strong scattering limits for conduction band valleys that make a circular projection on the interface plane, such as Γ and X valleys. For conduction band valleys that make a strongly anisotropic projection on the interface plane, such as the L valleys of GaAs(100), the calculated L channel currents have significantly different threshold shapes in the two limits, as shown in Fig. 12. When the calculations are done in a spherical approximation, the threshold shapes are similar in the two limits and look like the result of the more complete anisotropic model in the strong scattering limit.

Recently, the electron scattering at the m–s interface was studied experimentally in the Au/GaAs/Al$_x$Ga$_{1-x}$As system by using SD-BEEM spectroscopy [5]. The SD-BEEM spectrum is proportional to the heterostructure transmission coefficient [58], and is particularly useful both for
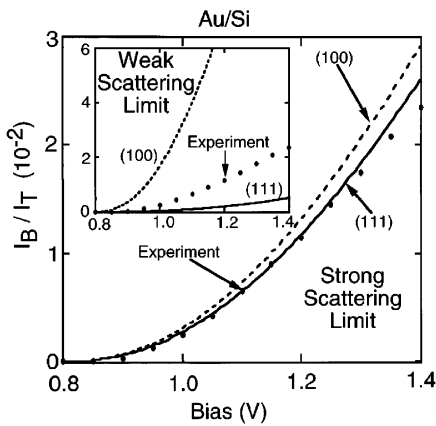
Fig. 10. Comparison of the calculation in the strong scattering limit for Au/Si(1 0 0) (dashed line) and Au/Si(1 1 1) (solid line) with the experimental results for Au/Si of Refs. [86,87]. These measurements were made on Au/Si(1 1 1) but measurements for Au/Si(1 0 0) are very similar to those for Au/Si(1 1 1) (see Refs. [70,102]). The inset (referenced earlier in our paper as Fig. 6(a)) compares the calculation in the weak scattering limit to the same experimental results [85].
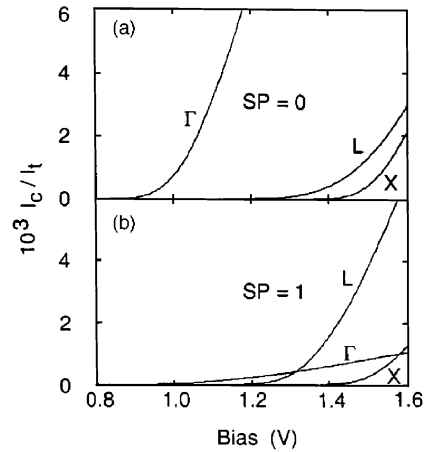
Fig. 11. Calculated ratio of collector to tunneling current as a function of bias for the three conduction band channels of Au/GaAs(1 0 0) in the weak scattering limit (upper panel) and in the strong scattering limit (lower panel) [59].

separating the contributions from various conduction band channels and for analyzing the threshold shapes. The analysis of the SD-BEEM spectral shape is more effective than just the BEEM current magnitude because the absolute value of the BEEM current could be scaled by the fluctuations in both the metal layer and semiconductor epilayer thickness. In GaAs, conduction bands with both zero and large interface parallel wavevector coexist in the same material. Thus direct and indirect transport channels can be investigated in the same sample. The observed SD-BEEM spectral shape shows obvious deviation from the calculations that assume transverse momentum conservation. In Fig. 13, we compare the calculated (dashed lines) collector current and its second voltage derivatives with the corresponding measured quantities (solid lines) for a Au/GaAs sample at room temperature. (Sample structures and the measurement technique are described in Ref. [5].) The SD-BEEM spectrum was extracted from the experimental BEEM spectrum in Fig. 13(a) by numerical differentiation with a 10 meV window, as shown in Fig. 13(b). The probability of electron scattering at the m–s interface (SP) was adjusted to fit the SD-BEEM spectra. The SD-BEEM spectra clearly separate the contributions from Γ and L electrons; thus, the weighting of the relative Γ and L channel contribution is a sensitive test of the model. The best fit to the SD-BEEM spectrum gives a 85% probability for electron scattering at the m–s interface. For comparison, theoretical curves for the cases without scattering and with 100% scattering are also shown. The measured relative contribution of the L-electrons is different than that calculated for the L channel in the weak scattering limit. Specifically, the L-electron collector current is found to be the strongest one, whereas, assuming transverse momentum conservation, the contribution of
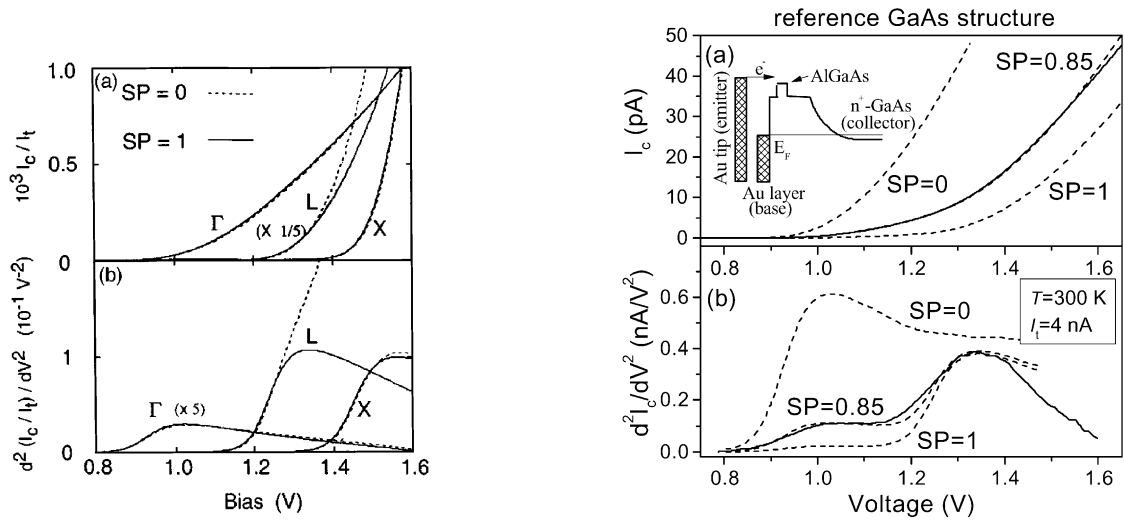
Fig. 12. Scaled ratio of collector to tunneling current (upper panel) and scaled second voltage derivative of the ratio of collector to tunneling current (lower panel) as a function of bias for the three conduction band channels of Au/GaAs(1 0 0). The scaling factors for all the valleys were chosen so that the currents for two limits overlap well in the near-threshold region. The strong scattering limit results (solid lines) are as calculated and the weak scattering limit results (dashed lines) are scaled by: Γ channel, divide by 31; L channel, multiply by 4.5; X channel, divide by 1.7 [59].

Fig. 13. The room-temperature BEEM (a) and SD-BEEM (b) spectra of the 1 μm undoped GaAs layer grown on n^+ GaAs substrate. The MSIS model calculations (dashed lines) are also presented for three values of SP, the electron scattering probability at the m–s interface. The inset in (a) shows a schematic band diagram of the samples under study [5].

the L band (which does not project to the zone center of the interface BZ) can give only a small BEEM current onset. The Γ and L channel contributions are included in the calculation but the X channel contribution is not included. In this experimental structure, the absence of the X conduction minimum contribution at room temperature is due to the image potential-induced strong electron scattering in the spacer between the metallurgical m–s interface and the maximum of the barrier height [2,67]. Fig. 14 presents the MSIS model fits to the BEEM and SD-BEEM spectra for a number of Au/GaAs/Al$_x$Ga$_{1-x}$As single barrier structures. In this case, the best fits are obtained with the scattering probability at the m–s interface varying between 85% and 92% among these samples. This small variation in the scattering parameter indicates that our diode fabrication procedure is reproducible and results in approximately the same quality of the m–s interface. Intervalley scattering at the GaAs/AlGaAs heterojunction interfaces is assumed to be minor in comparison with the scattering at the m–s interface. Indeed, intervalley scattering in GaAs/AlGaAs heterojunctions was studied both experimentally [88,89] and theoretically [90,91], and conservation of the transverse momentum is expected for this epitaxial heterojunction interface. For epitaxial growth, the GaAs/Al$_x$Ga$_{1-x}$As interface is a near perfect heterojunction interface, with a lattice mismatch of less than 0.8%. In contrast, metal deposition is not epitaxial,
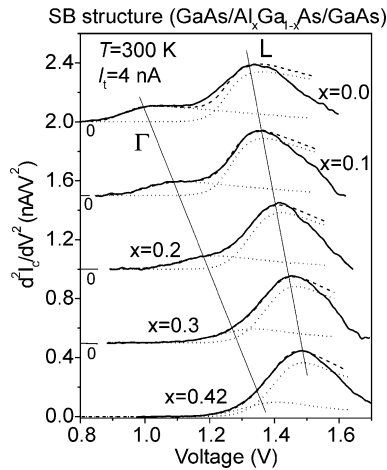
Fig. 14. Room-temperature SD-BEEM spectra for five different Al compositions (solid lines). For clarity, the SD-BEEM spectra are shifted along the vertical axis. Thin solid lines are eye-guides for the peaks position development. The MSIS model calculations are also presented. The model calculations show the separate Γ and L valley contributions (dotted lines) and their sum (dashed lines) [5].

and, therefore, the quality of the Au/GaAs interface is not as good as the quality of the GaAs/ $Al_xGa_{1-x}As$ heterojunction interface. The possible effect of electron multiple reflection either in the metal (the metal layer is thick enough that a multiply reflected component is strongly attenuated) or at the heterostructure interfaces (this mechanism would amplify mainly the current of the Γ-electrons since they are the electrons with the longest mfp in the semiconductor heterostructure) is small and cannot explain the observed strong L-electron and comparatively weak Γ-electron contributions.

2.5. Metal base layer effect on BEEM transport

2.5.1. Effect of carrier scattering in metals

The BEEM current transmitted through the metal base layer attenuates strongly as the metal film thickness increases. The survey of the experimental and theoretical data is presented in Fig. 15. The total attenuation length λ in the metal can be described by $1/\lambda = 1/\lambda_I + 1/\lambda_e$, where λ_e is the electron elastic mfp and λ_I is the electron inelastic mfp in the metal. The energy dependence of λ is due to the energy dependence of λ_I that, at low voltages, results from inelastic electron–electron scattering processes [2,86]. λ_I is usually given in the form of $\lambda_I(E) = E/[A(E - E_F)^2]$, expected for the electron–electron scattering mechanism [69], where A is the electron–electron scattering strength parameter. Taking into account the Au band structure, Reuter et al. [69] studied the energy dependence of the inelastic mfp (due to the electron–electron interactions), using a Green-function approach and complementary Monte Carlo simulations. The authors found that λ_I predicted by the standard Fermi-liquid theory provides excellent agreement between theoretical and experimental BEEM spectra (giving $\lambda_I(E - E_F = 1 \text{ eV}) = 252$ Å). In contrast, a relatively weak linear energy dependence in the empirical form of $\lambda_I(E) = 1.5\lambda_{i0}[1 - (E - E_F)/3]$ was deduced
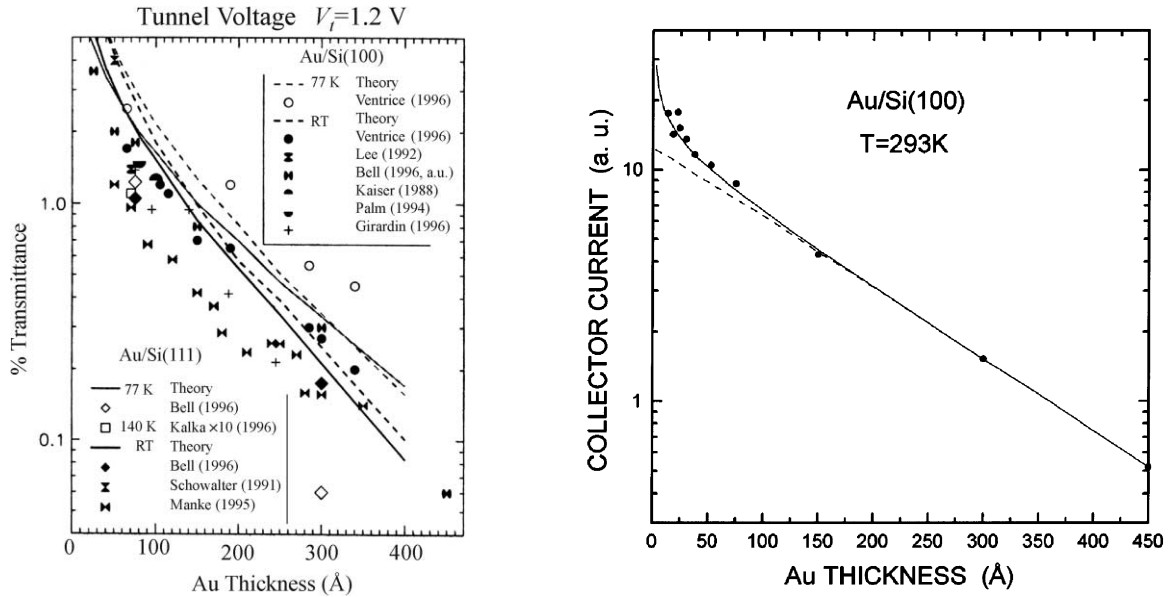
Fig. 15. Transmittance of the Au/Si interface at a tunnel voltage of 1.2 eV as a function of the Au-layer thickness [103].

Fig. 16. Experimental BEEM attenuation length measurement (circles) for Au/Si(100) samples. I_c was measured at $V_t = 1.2$ V. The solid (dashed) line is the dependence, which results if boundary reflections within the Au film are allowed (not allowed) [86].

from the fitting procedure for the Au/Si system [86], where λ_{i0} is the inelastic mfp length for electrons at $E - E_F = 1$ eV, using $\lambda_e = 400$ Å and $\lambda_{i0} = 220$ Å. The fitted total attenuation length of $\lambda \sim 130$ Å at 1 eV above the Fermi energy is in a good agreement with $\lambda = 133$ Å at $T = 300$ K and $\lambda = 147$ Å at $T = 77$ K obtained in Au overlayers on Si(100) over the energy region of 0.92–1.2 eV above the Fermi level [55], even though a certain distribution in λ values is also expected [92,93].

If λ_I is much shorter than λ_e, λ will also be energy dependent, namely, will decrease with the electron energy (tip-to-base voltage) increase. It will induce, according to Eq. (1), a certain additional decrease of the BEEM current as the tip-to-base voltage increases, therefore, changing the BEEM spectral shape. Comparison of Monte Carlo simulations with the experiment shows that the strong variations in the spectral shape of the BEEM current in metal/GaP at $V_t < 4$ V are mainly due to the energy dependence of the mfp for inelastic scattering in the metal. Ludeke et al. [64] showed for the case of Pd/GaP that, when the base layer is much thicker than the mfp of electrons, the multiple collisions with phonons will reduce effectively the injected electron energy and induce the delay of the onsets observed in the BEEM current. For thin metal layers, the effect of the electron scattering in the metal (Cr, Pd and NiSi$_2$ at thickness < 100 Å) was mainly the attenuation of the BEEM current without the spectral shape change. While the truly ballistic transport in the metal film is obscure in most experiments [7], the ballistic characteristic would strengthen if experiments were performed in ideal conditions using clean tips and samples at low

temperatures and low voltages. In fact, features due to standing waves in thin metal films were observed in experimental BEEM spectra [77].

By studying the dependence of BEEM spectral shape on Au thickness, Bell [86] argued that the contribution of multiple electron reflections within the metal layer is the primary factor preventing previous BEEM observations of $k_{||}$ conservation in thin metal films. To illustrate the effect of multiple electron reflections in the metal layer, the authors plotted the collector current dependence on the Au thickness in Au/Si(100) system, as shown in Fig. 16. The deviation from the logarithmic dependence in the limit of thin metal layers was attributed to the presence of multiple electron reflections. Recently, Reuter et al. [69] have used a more advanced model to fit the experimental data of Ref. [86], and the importance of the multiple electron reflection in describing the spectral shape and amplitude of the BEEM current was confirmed.

2.5.2. Metal band structure effect

Previously discussed models to explain the lack of BEEM sensitivity to the Si orientation in the Au/Si systems have usually invoked strong elastic scattering of the ballistic electrons, either at the Au/Si interface, and/or in the bulk or at the surface of the Au overlayers. In contrast, by using the Keldysh Green-function method, Garcia-Vidal et al. [94,95] suggested that the Au band structure might be responsible for the observed similarity of Au/Si(100) and Au/Si(111) BEEM spectra (at least both mechanisms, i.e. $k_{||}$ non-conservation and Au band structure effect, should be weighted). It was pointed out that the Au films often grow (111) oriented on Si surfaces after the first four or five layers are completed, and that there are no propagating Bloch electron states in the cone centered on the (111) direction, from below the Fermi surface to several eV above it. This requires that electrons injected into such an overlayer must propagate at angles considerably away from the normal if they are to travel ballistically through the metal to the Au/Si interface. This approach
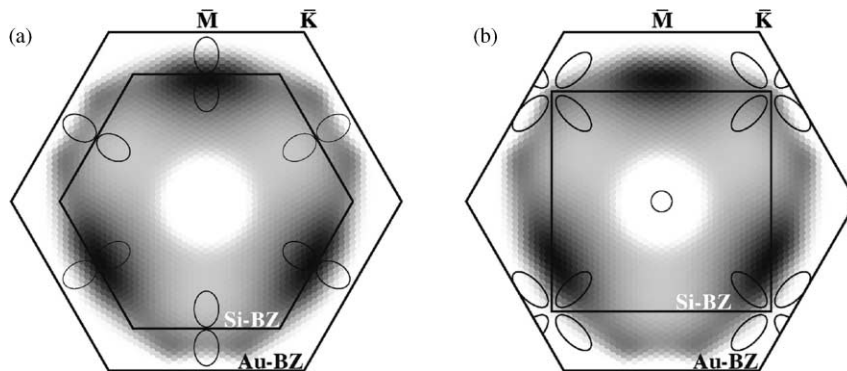

Fig. 17. Matching of the obtained semiclassical k-space BEEM current distribution with the available CBM states in the semiconductor, which are approximated by projected parabolic bands. Projected gold surface BZ is given by external hexagon, whereas Si(1 1 1) and Si(1 0 0) BZs are, respectively, given by the hexagon and the square inside. Current can only enter into the Si through the area enclosed by the ellipses ($E = E_F + 1$ eV). (a) Au/Si(1 1 1), $E_s = 0.86$ eV, (b) Au/Si(1 0 0), $E_s = 0.82$ eV. Note that the different lattice parameters of Au and Si require remapping of the Si ellipses inside the larger Au BZ. $\bar{\Gamma}$–$\bar{M}$ corresponds to the [1 0 1] direction in k space [95].
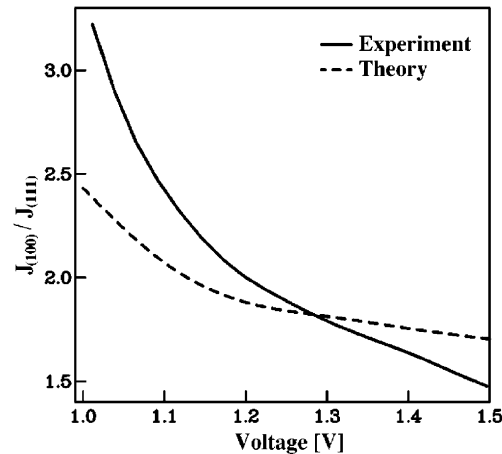
Fig. 18. Ratio of current injected in Si(1 0 0) and Si(1 1 1) after propagation through thin Au films of approximately equal thickness (1 0 0 Å Au/Si(1 0 0) and 75 Å Au/Si(1 1 1), chosen to compare with available experimental data). Elastic electron propagation is used in the theory (dashed line); experimental data taken from Refs. [86,96] (solid line) [95].

differs from the free-electron treatment of the existing model [1] that allows an electron beam propagating in normal direction through the metal film grown in the [111] direction on either Si(111) or Si(100). For Au(111) on Si(100) and Si(111), the allowed (in the metal) wavevector and the silicon conduction band minima projections on the interface BZ overlap partially, to essentially the same extent for both Si(100) and Si(111) faces, as shown in Fig. 17. Thus the ballistic electrons, even when injected with a small transverse momentum component, will, if passing through a sufficient thickness of Au, reach the interface with substantial transverse momentum. It was concluded that the Au band structure itself could provide the required transverse momentum to facilitate interfacial ballistic transport in the Au/Si(111) system. Fig. 18 compares the theoretical calculations of Ref. [95] and the experimental data of Refs. [86,96] for the ratio of current injected in Au/Si(100) and Au/Si(111). Despite general agreement in the magnitude and in the overall trend with energy, a discrepancy up to 30% was obtained between the theory and the experiment. In some contradic- tion to the dependencies shown in Fig. 18, Weilmeier et al. [93] have found experimentally that BEEM current for Si(111) is more than 50% higher than that for Si(100) substrates for Au(111)/Si(111) and Au(111)/Si(100) studied at UHV conditions. To explain their findings, Weil- meier et al. suggested that in their experiment the Au(111) grains are aligned not in-plane but randomly with the Si(100) substrate.

Ripard et al. [97] have lately demonstrated the filtering effect of the Co/Cu interface by conducting a BEEM study on Co/Cu/Co trilayers. The strong reduction of the BEEM current when ∼2–3 Å of Co is evaporated on top of the Cu/Au/Si system was attributed to the band structure mismatch at the Co/Cu interface [Cu(111) has no propagating momentum states in a much larger cone around the film normal than Co(111)].

Recently, two cases of electron scattering (reflective vs. diffusive) in the metal have been considered by Menegozzi et al. [53] for the Au/Si system. A satisfying agreement of the model with
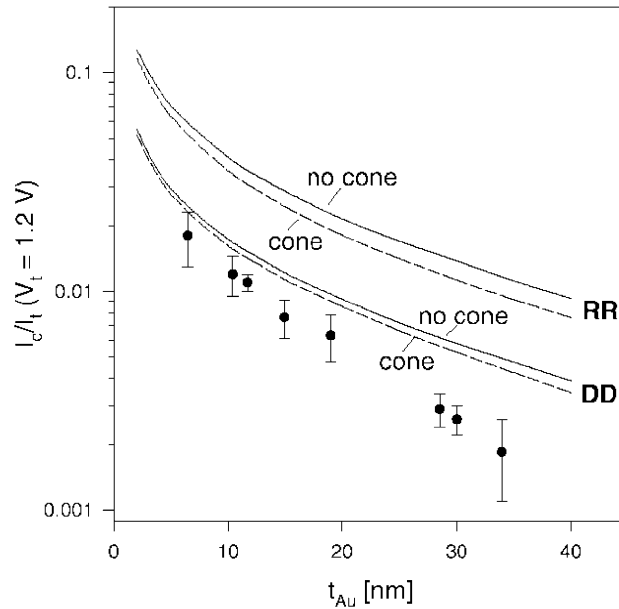
Fig. 19. The value of the BEEM characteristics I_c/I_t at the tunneling voltage of 1.2 V versus the Au film thickness t_{Au} for Au/Si(0 0 1). Curves are calculated for reflecting (RR) or diffuse (DD) interface structure as indicated by assuming an isotropical Fermi surface ("no cone", *solid line*) and a forbidden cone in the Fermi surface ("cone", *dashed line*). Measured data points are taken from Ref. [55] (from Ref. [53]).

the experiment on Au(111)/Si(111) was obtained, although it seems that a different interface scattering should be assigned to different experiments. The results for Au(111)/Si(100) exceeded at least by factor of 2 the experimental data. To improve the matching, the authors considered the effect of the Au band structure. However, the implementation of the Au(111) band structure gave only minor suppression of the BEEM current ($\sim 5\%$), as shown in Fig. 19, and thus cannot explain the mismatch.

Summarizing the results presented in this section, the effect of the hot electron scattering at the m–s interface was intensively studied both theoretically and experimentally. Experimentally, the BEEM transport was found to deviate significantly from the simplified picture of transverse momentum conservation at the m–s interface in the BK model, for the non-epitaxial Au/Si and Au/GaAs interfaces, and, to some extent, even for the more perfect epitaxial $CoSi_2$/Si system. Although certain upgrading in the theoretical description was achieved by elaborating the metal overlayer effect (e.g. metal band structure effect as well as effects of the electron scattering and multiple electron reflection in the metal layer on the BEEM transport), the proposed models suffered from the lack of the quantitative description of the experimental BEEM data. A real improvement of the theoretical fit to the experimental data was obtained by assuming a strong electron scattering at the m–s interface. Among the m–s interface scattering models, the MSIS model is the most developed model and allows a qualitative analysis of the electron scattering at the m–s interface. Using the MSIS model, the electron scattering probability was estimated to be ~ 85–95% at the non-epitaxial Au/GaAs interface.
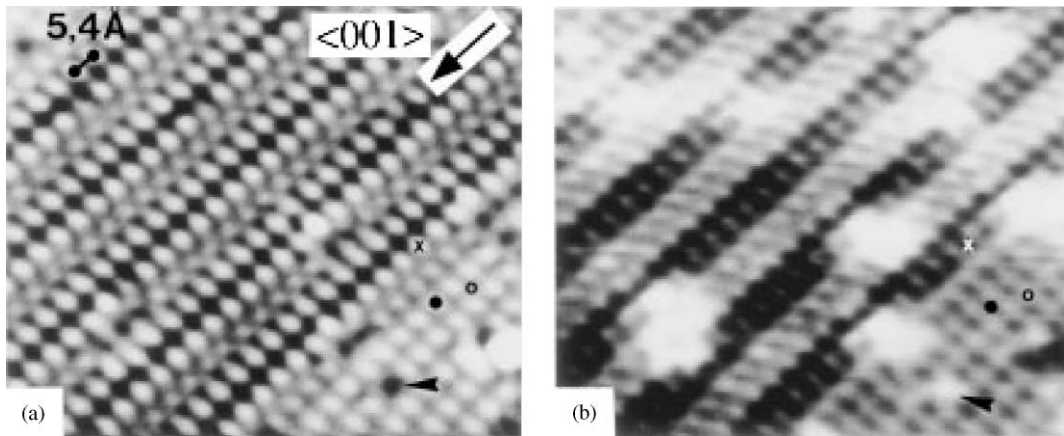
Fig. 20. STM topographic image (a) and simultaneously recorded forward BEEM image (b) on the Si-rich $CoSi_2$/n-Si (1 0 0) surface ($V_t = 1.5$ V, $I_t = 3$ nA, film thickness $d = 38$ Å). The center part displays a $3\sqrt{2} \times \sqrt{2}$ $R45°$ reconstruction, whereas the lower right is $\sqrt{2} \times \sqrt{2}$ $R45°$ reconstructed. The $\sqrt{2}$ topographic corrugation is 0.15 Å. The BEEM contrast ranges from 25 pA (black) to 55 pA (white) [98].

3. BEEM resolution

3.1. Spatial resolution

Sirringhaus et al. [8,98] have succeeded to image periodic surface structures at atomic resolution by in-situ BEEM on the Au/Si system, as shown in Fig. 20. The superior resolution (~ 10–20 Å) of the BEEM technique was demonstrated in imaging of microfabricated Au/SiGe diodes [99] and in imaging the Schottky barrier inhomogeneities for the $Au/Co/GaAs_{0.67}P_{0.33}$ system [100]. Also, a spatial resolution of ~ 10 Å (see Fig. 21) was obtained by in-situ BEEM in imaging the interfacial defects in 30 Å $CoSi_2$/Si(111) system at $V_t \sim 1.5$ V [77]. This resolution is reduced at high tip voltages due to the secondary electrons that have broad energy and momenta. For example, for $V_t = 6$ V, the spatial resolution of BEEM reduced to ~ 100 Å [101].

The observed high spatial resolution in BEEM experiments is to a certain extent an unexpected result. Indeed, the nanometer-scale resolution (~ 15 Å) was obtained after propagation through Au films as much as 100–150 Å in the case of the Au/Si system [102], whereas the free-electron model for the metals [56,102] predicts a BEEM resolution for relatively thick 100–150 Å Au films of at best ~ 100 Å. To explain the high spatial resolution observed in BEEM experiments, the metal band structure effect was examined as a possible candidate. In the case of epitaxial $CoSi_2$ layers on Si(111) substrates, Reuter et al. [9] showed by using the Keldysh Green-function method that hot electrons injected from a STM tip into a $CoSi_2$/Si(111) system form a highly focused beam due to the silicide band structure. It was calculated (see Fig. 22) that the current spatial distribution at $V_t = 1.5$ V remains highly focused (FWHM is 8.9 Å) after propagating through a 30 Å $CoSi_2$(111) film (the free-electron propagation in the metal would result in ~ 25 Å resolution). This spatial resolution is in a good agreement with the resolution of ~ 10 Å with which interfacial point defects
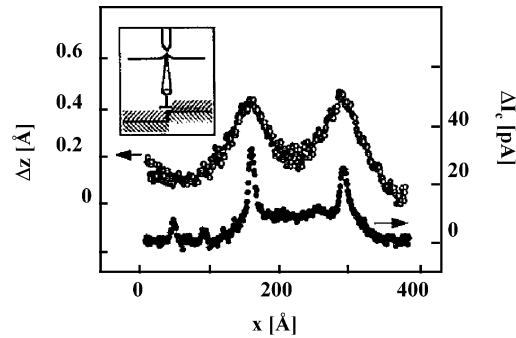
Fig. 21. STM topography (top) and BEEM (bottom) cross sections perpendicular to two parallel dislocation lines, together with a schematic drawing (inset) ($V_t = 1.5$ V, $I_t = 2$ nA, film thickness $d = 30$ Å) [77].
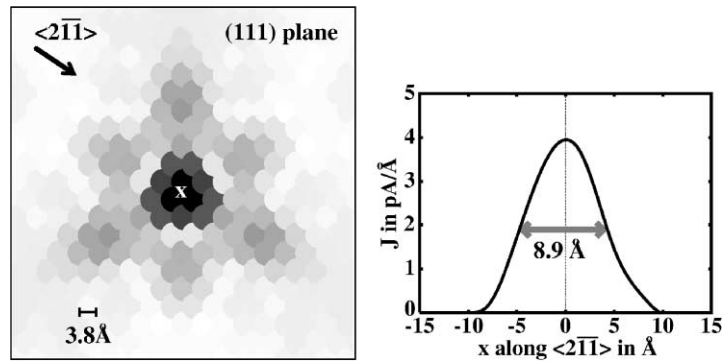

Fig. 22. Current distribution in a Si2 layer parallel to the surface after propagation through a 30 Å CoSi$_2$(111) film. Injection from the tip at 1.5 eV occurred in the center of the shown plane (white X), where the maximum current propagating in a focused beam along the $\langle 111 \rangle$ direction can still be found. The linear gray scale indicates current intensity at each atomic site: black maximum to white zero current. The right-hand panel displays a cut through the focused beam in the $\langle 2\text{-}1\text{-}1 \rangle$ direction from which a FWHM of 8.9 Å can be derived [9].

were resolved experimentally [77,81]. In the case of Au(111) on Si, the immediate consequence of the propagational gap of Au in the [111] direction is the opening up of the injected beam as the depth increases [95]. The deeper the chosen layer, the more spread over a larger ring (more precisely a spreading triangle considering the symmetry of a fcc (111) crystal) the current would be, but the sideward-directed propagation remains sharply focused (see Fig. 23). Thus, the real space distribution in any layer parallel to the surface would be a spreading triangle with the effective triangle side thickness of ~ 10 Å after propagating through ~ 60 Å of Au, in good agreement with the experiment [102]. Also, the results of the ensemble-Monte-Carlo simulations, where the effect of the metal band structure on the electron propagation was incorporated by cutting off the forbidden directions arising from gaps in the constant-energy surface, agree qualitatively with the (widely scattered) experimental BEEM data on the Au/Si system [103]. It should be noted though
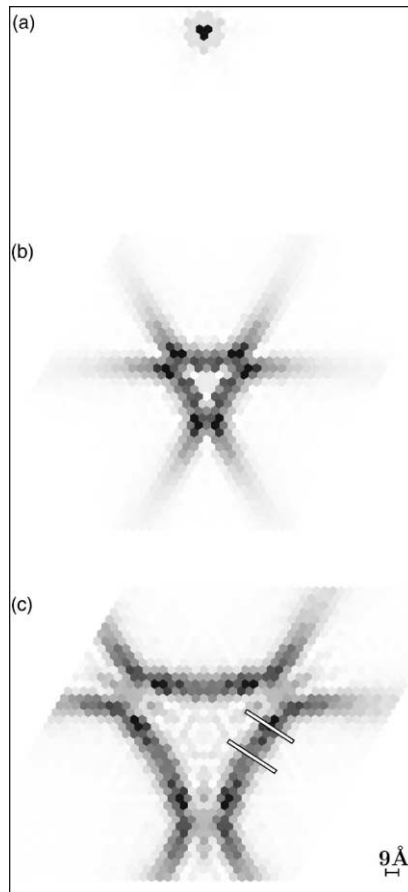
Fig. 23. Real-space BEEM current distributions for Au(1 1 1) after injection of current in one atom in the first layer (located in the center of the drawn layer). The tip is positioned at $5.0\,\text{Å}$ height on top of the active atom, with $V_t = E_F + 1$ eV. Distribution in (a) 2nd layer ($2.35\,\text{Å}$), (b) 10th layer ($21.19\,\text{Å}$), and (c) 25th layer ($56.51\,\text{Å}$). Each dot represents one atom in the corresponding layer and the gray scale indicates the amount of current passing through the atom: black for maximum current to white for zero current [95].

that, according to Fig. 23, the calculations predict "multiple images" of the interface objects, since a tip scan would sweep each of these lines across the interface object, each time leading to a focused signal. However, this effect was not observed experimentally.

3.2. Energetic resolution

3.2.1. Low-temperature BEEM

To fully exploit the BEEM capabilities, it is very beneficial to perform the BEEM experiments at cryogenic temperatures. There are at least three advantages to use the low-temperature BEEM technique: (i) improvement of the energy resolution due to the reduced thermal broadening of the

Fermi distribution, (ii) thermal noise is greatly reduced and (iii) thermal drift of the STM tip position is reduced.

The first successful BEEM operation at low temperatures (7 K) was reported in 1995 in the Au/Si(100) system [45]. It was shown that the vertical resolution was 0.3 Å and the positional drift of the microscope was less than 2 Å/h for operation at 7 K and 7 Å/h for operation at 77 K. In contrast, the usually observed room-temperature drift is much higher, of the order of several Å/min at $T = 300$ K [104].

Later, BEEM was performed on Au/GaAs [84] and Au/GaAs/Al$_{0.2}$Ga$_{0.8}$As/GaAs single-barrier structures [32] at $T = 7$ and 77 K. The SD-BEEM spectra (in the near-threshold region up to the onset of the L valley of GaAs) were used to analyze the electron-wave interference effect. The low background noise (<3 fA rms) and high spectral resolution ($k_B T \sim 0.5$ meV (6 meV) at $T = 7$ K (77 K)) enables the detection of features (additional peaks and dips) that cannot be reproduced by the Au/Al$_{0.2}$Ga$_{0.8}$As single-interface model, since this model describes only the average shape of the SD-BEEM spectra. A more complete model [84] that incorporates the interference effects (reflections) at the Au/GaAs, GaAs/Al$_{0.2}$Ga$_{0.8}$As and Al$_{0.2}$Ga$_{0.8}$As/GaAs interfaces is shown to describe the data more accurately and consistently over many spatial locations and samples.

As was pointed out by Henderson et al. [50], a main difficulty at very low temperatures (<10 K) is related to carrier freeze-out in the semiconductor, which leads to charging effects in the collector electrode. In contrast to bulk samples, satisfactory BEEM measurements in liquid He can be obtained with the use of a low-dimensional electron gas layer as a collector electrode. Eder et al. [46] have studied the laterally patterned quantum wires fabricated on modulation-doped GaAs/AlGaAs heterostructures by BEEM at $T = 4.2$ and 300 K, using a 2D electron layer at the AlGaAs/GaAs interface to collect the BEEM current. At $T = 4.2$ K, no decrease of STM resolution was found in comparison with room-temperature measurements.

3.2.2. Semiconductor STM tips for BEEM

The use of degenerate semiconductors as the STM tip is potentially very useful to increase significantly the BEEM energy resolution, since the electron distribution is limited to the small range between the conduction band edge and the Fermi level. This allows a quasi-monochromatic energy distribution of the injected electrons, in contrast to the case of the conventional metal tips where the energy distribution of injected electrons is defined by the combined effect of the tunneling probability and the wide Fermi-distribution function of the tip electrons. In the literature, degenerate semiconductor tips such as highly doped GaAs and Si were already used for STM experiments [105,106]. Recently, BEEM experiments with n-doped InAs tips (InAs is a very promising material for semiconductor tips since it has a natural surface accumulation layer of electrons [107]) were reported at room temperature [108,109]. The InAs tips were fabricated by cleaving the InAs wafer, and then the cleaved piece of InAs was glued on the tilted holder so that one corner of the InAs piece can be used as a tunneling tip. In the experiment, BEEM spectra of modulation-doped Au/GaAs/AlGaAs sample at 300 K and in liquid helium obtained with InAs tip are of comparable amplitude with the spectra obtained using standard Au tips. While the spectral shape of the BEEM spectra obtained with InAs tips is somewhat different from the reference curves measured with Au tips, the expected enhanced energy resolution was not observed with InAs tips. Possible reasons for this were attributed to hot electron scattering processes in the Au film. We

believe that future BEEM study of structures, which give qualitatively different BEEM spectral shapes for metal and semiconductor STM emitters (for example, buried resonant heterostructures) should provide an experimental support for the energy-resolution effect of semiconductor STM tips.

3.3. Depth resolution

The hot electron transport in BEEM experiments can be considered to be ballistic only with certain restrictions. The real picture is certainly different because of consecutive scattering processes in the metal base film, at the m–s interface and in the semiconductor itself. Even for the case of a perfectly clean device and extremely low temperatures, the carrier mean free path is usually comparable with the device thickness. Therefore, the ballistic description of the electron transport is restricted to layers close to the surface. As a consequence, BEEM can be characterized by its depth resolution.

Monte Carlo simulations [110] of electron transport in the Γ, L and X valleys of GaAs were performed using the MSIS model [85]. With increasing object depth beneath the Au/GaAs interface, the Monte Carlo simulations predict (a) significant cooling of hot electrons, on the order of ~ 3 meV/nm at 1.5 eV, and (b) significant redistribution of electrons among the conduction bands (see Fig. 24). In order to show experimentally that scattering inside the semiconductor structure affects the BEEM spectra, in Ref. [5] we compared the BEEM spectra for several pairs of Au/GaAs/AlGaAs single barrier (SB) samples with the same SB composition but with different cap thickness of 50 and 300 Å. The obtained SD-BEEM spectra of the GaAs/Al$_{0.2}$Ga$_{0.8}$As/GaAs SB samples are shown in Fig. 25 for $T = 85$ and 300 K (these data are representative for all samples pairs). Since the expected mfp lengths for the Γ, L and X electrons at $T = 300$ K are ~ 1000, ~ 100 and ~ 10 Å, respectively [43], manipulations with the heterostructure thickness in the range of 100–300 Å should affect mainly the L-electrons contribution to the BEEM current (the effective heterostructure thickness, that will affect the BEEM current collection, is the combined thickness of the GaAs cap layer and the SB layer). Indeed, as one can see from Fig. 25, the L-electrons contribution for the sample with 300 Å-cap layer (with the SB thickness of 50 Å, the total effective heterostructure thickness is ~ 350 Å) is reduced by factor of 3 as compared with the 50 Å-cap layer sample (the total effective thickness of ~ 100 Å), whereas the Γ contribution has remained intact. As the temperature decreases from 300 to 85 K, in addition to the spectrum shift expected from the temperature dependence of the energy gap, a strong increase of the signal is observed for the L-electrons in the SB sample with the 300 Å-cap layer, whereas the SD-BEEM spectral shape remains essentially the same for the SB sample with the 50 Å-cap layer. These experimental results are in agreement with the expected increase in the mfp of the electrons with the decreasing temperature. As the temperature decreases from 300 to 85 K, the calculated mfp near the energy threshold increases from ~ 1000 to ~ 1500 Å for Γ electrons and from ~ 100 to ~ 300 Å for the L electrons [43]. The X-electrons contribution is completely obscured in the room-temperature BEEM spectra presented in Fig. 25 due to their effective scattering in the GaAs cap layer. Indeed, the X-electrons mfp (~ 10 Å at $T = 300$ K and ~ 30 Å at $T = 85$ K) is shorter than the effective heterostructure thickness for all samples (≥ 100 Å). Thus, while the initial electron distribution among the conduction bands of the semiconductor is specified by transport through the metal base layer and by the m–s interface scattering, further electron transport is governed by the difference in
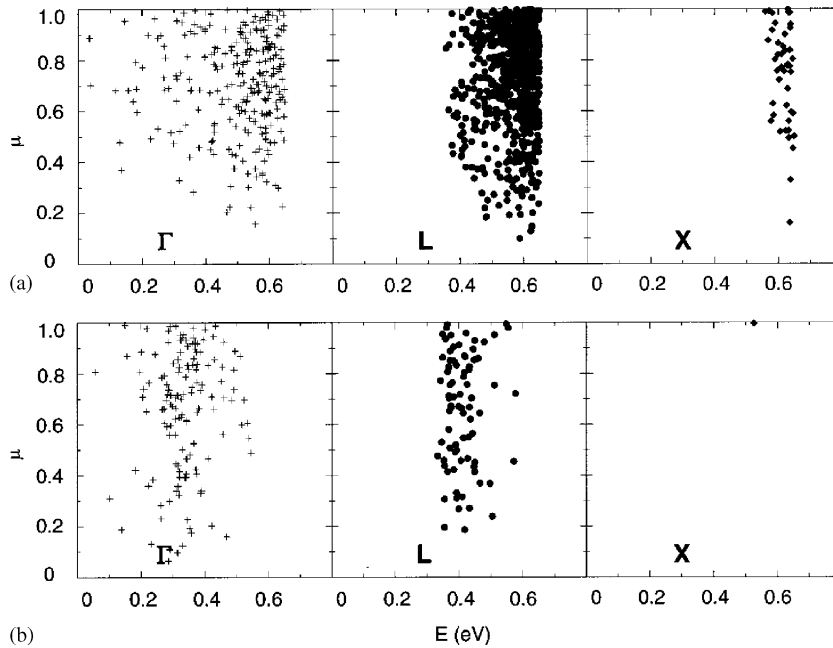
Fig. 24. For the populations of the electrons in GaAs resulting from a BEEM experiment of Au–GaAs, the energy and angular distributions are shown. The y-axis is the cosine, denoted by μ, of the angles of the velocities of the electrons with respect to the interface normal and the x-axis is the kinetic energy E of the electrons with respect to the Γ-valley minimum. The condition is the strong scattering limit of the MSIS theory at 300 K and at a bias of 1.53 V. Initially, 1000 electrons are injected at the Au–GaAs interface. (a) The initial electron distributions of Γ-(left panel and crosses), L-(middle panel and circles), and X-(right panel and diamonds) valley electrons at the Au–GaAs interface. (b) The distributions at 600 Å below the Au–GaAs interface (from Ref. [110]).

the electron mfp length for the Γ, L and X electrons. In imaging the buried semiconductor structures, the mfp length (in the case of GaAs-based structures, the mfp length of Γ-electrons as the longest one) will determine the depth resolution of BEEM. It implies that the BEEM contrast will be not enough to resolve a semiconductor structure buried much deeper than the electron mfp length (~ 1000 Å for the Γ-electrons of GaAs). Therefore, as the heterostructure, characterized by several transport channels, is buried deeper, the information about these conduction channels is gradually gone, starting from the transport channel with the shortest electron mfp length.

Lee et al. [111] have performed Monte Carlo simulations of the transport of electrons injected into the Γ valley of GaAs for BEEM imaging and spatially resolved spectroscopy of model quantum dots (QD) and quantum wires (QW) buried beneath the Au/GaAs interface. For Monte Carlo simulations, a modified BK model was used, with the buried object forming a local barrier for the electron transmission (such as AlSb and GaSb dots grown on GaAs). The collection plane was located at 2000 Å below the Au/GaAs interface, and the QD (QW) was modeled as a thin disk 300 Å in diameter (a thin 300 Å wide stripe), which specularly scatters electrons of all energies. Fig. 26 shows the calculated BEEM current as a function of lateral displacement between the STM tip and the center of the buried dot (wire), for three depths of the QD (QW) from the Au/GaAs
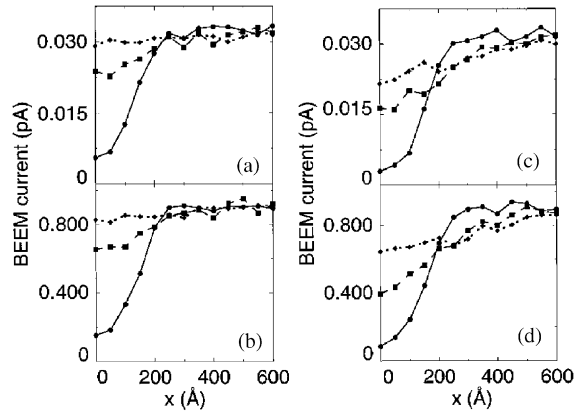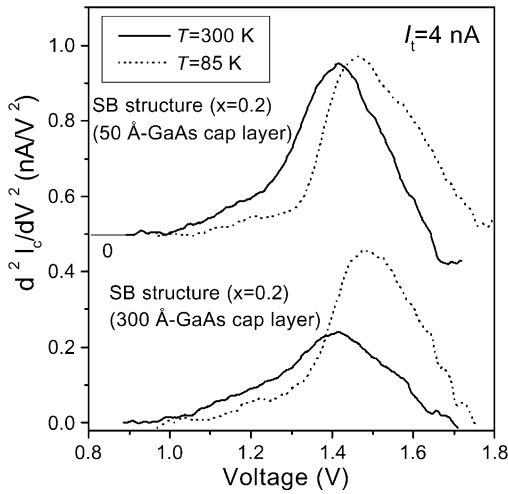
Fig. 25. SD-BEEM spectra for GaAs/Al$_{0.2}$Ga$_{0.8}$As/ GaAs single barrier (SB) samples with 50 and 300 Å GaAs cap layers, taken at $T = 300$ K (solid curves) and $T = 85$ K (dotted curves). For clarity, the spectra are shifted along the vertical axis [5].

Fig. 26. The BEEM current as a function of lateral displacement at a tip-to-sample bias of 1 V (a) and 1.25 V (b) for a perfectly reflecting quantum dot 300 Å in diameter, and at a tip-to-sample bias of 1 V (c) and 1.25 V (d) for a perfectly reflecting 300 Å wide quantum wire. The lines are drawn as a guide for the eye. In all cases, the solid line (circle) is for $d = 100$ Å, the dashed line (square) is for $d = 300$ Å, and the dotted line (diamond) is for $d = 600$ Å [111].

interface. One can see that the BEEM contrast decreases with the depth of the object. At a depth of 600 Å, a QD is hardly detectable by BEEM whereas the QW still shows significant contrast, due to the added dimension. In addition, it was shown that due to an interplay between a geometric filtering effect and the role of the electron–phonon scattering (assuming electron transverse momentum conservation at the m–s interface), there is a range of optimum depths for the sharpest crystal momentum and energy distribution of the electrons incident upon the buried structure.

As an example of BEEM imaging of deeply buried localized objects, a study of misfit dislocations at the In$_x$Ga$_{1-x}$As/GaAs interface buried 400–700 Å below the m–s interface was conducted in our laboratory [42,43,112]. The cross-hatch misfit dislocation network in In$_x$Ga$_{1-x}$As/GaAs was ideally suited for BEEM as the dislocation core beneath the surface gives rise to a perturbation at the surface easily visible by AFM or STM. Samples consist of In$_x$Ga$_{1-x}$As of different thickness grown on (001) GaAs substrates and were designed such that the dislocations will exist (Indium concentrations of $x = 0.15$–0.3 and InGaAs thickness of $d = 400$–750 Å were examined [112]). Simultaneous STM and BEEM imaging, shown in Fig. 27, revealed a decrease in the BEEM current directly associated with the cross-hatch pattern in the STM. The minimum in the BEEM current, through analysis of line scans, was found to be shifted ~ 400 Å from the maximum of the STM image, indicating that the loss in BEEM current is not simply a surface affect, but one that arises from the dislocation core located ~ 600 Å beneath the surface (see Fig. 28). This is in agreement with the theory that the dislocation core comes to the surface not along the growth
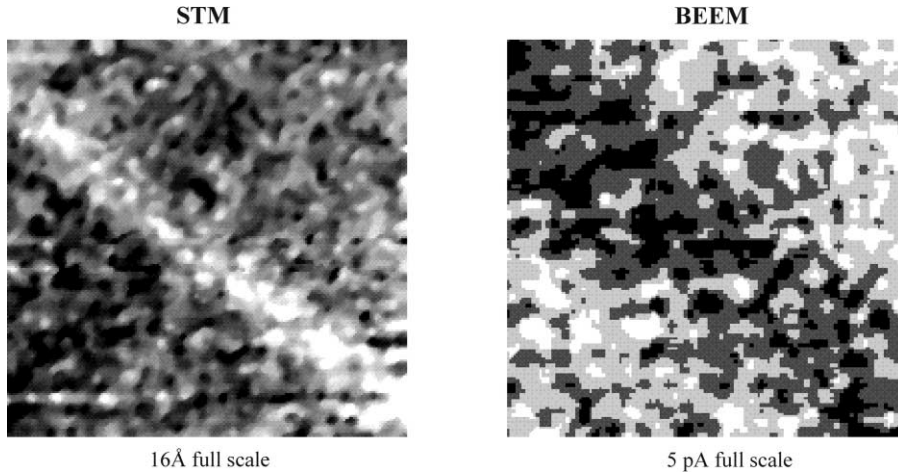
STM

BEEM

16Å full scale

5 pA full scale

Fig. 27. 1 μm × 1 μm STM (left) and BEEM (right) images of $In_xGa_{1-x}As/GaAs$ heterostructure ($x = 0.2$, $d = 600$ Å). The STM image shows the growth perturbation caused by the dislocation core. The BEEM image shows the decrease in current at the presence of the cross-hatch [112].
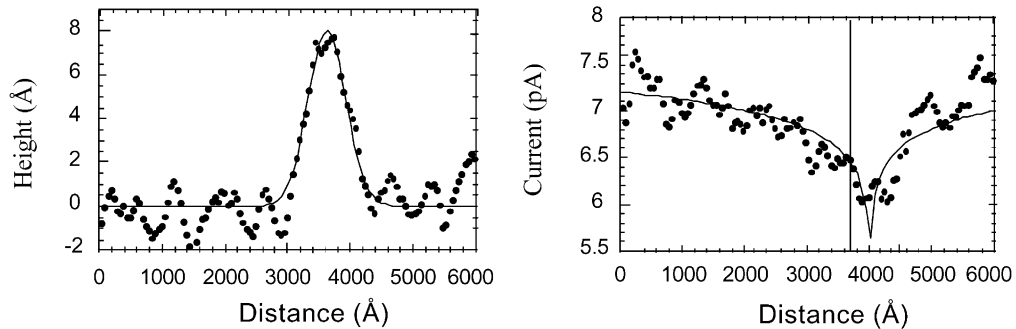
Fig. 28. STM (left) and BEEM (right) linescans taken over dislocation images. The STM linescans show a Gaussian peak while the BEEM linescans show a drop in the BEEM current shifted from the peak in the STM image [112].

direction, but along the glide plane (111), which is 54.7° off of the (100) direction. Monte Carlo calculations were used to understand the mechanism responsible for this decrease [112]. The simulation of the charged model fit closest to the experimental data suggesting that backscattering off of line charges to the metal base is responsible for the loss in BEEM current.

4. Homogeneity of BEEM transport

4.1. BEEM dependence on the m–s interface quality

The importance of interface chemistry for BEEM was underlined by Fernandez et al. [4], who showed on example of Au/Si interfaces that when Au is deposited in-situ on a UHV-cleaned Si

surface, no BEEM current can be detected through the resulting Au/Si interface. This was explained in terms of additional scattering from the Au–Si disordered alloy formed by Au–Si interdiffusion. The interface transmittance can be increased to some extent by HF-treatment of the substrate surface prior to the Au deposition. In this case, the residual impurity at the interface can act as a barrier, which passivates the Au–Si interaction enhancing the ballistic transmittance. For the Au/GaAs(100) system, Hecht et al. [113] showed that the MBE termination of the GaAs surface by a 2 monolayer (ML) AlAs diffusion barrier prior to the Au deposition results in a significant increase of the interface areas, which support BEEM transport, and produces a high-quality Schottky barrier.

It is well known that the Schottky barrier height depends on the chemical and mechanical pretreatment during the diode preparation. Chemical pretreatment in aqueous HF or HCl solutions and subsequent rinses in deionized water resulted in the Schottky barrier height variations up to 10–20% in Au/III–V (GaAs, AlGaAs, InP and InGaAs) [114] and Au/Si [115]. Everaert et al. [116] have found by using BEEM that mechanical polishing of the etched GaAs substrate prior to the Au deposition produces an increase of the Au/GaAs Schottky barrier. This increase was explained by the passivation of the interfacial defects by hydrogen and the consequent pinning of the Fermi level. Schottky barrier variations in Au/n-GaAs due to reactive ion etching by using $SiCl_4$ was studied by Vanalme et al. [117] who found the Schottky barrier reduction (by $\sim 6\%$) due to the change of the stoichiometry of the surface region produced by the reactive ion etching. In addition, Stockman et al. [118] showed that the BEEM current homogeneity and stability over time is very sensitive to the interface flatness, namely that the interface formed on the flat (110) cleavage plane of a GaAs(100) wafer, is more homogeneous than the interface formed on the as-grown (100) plane and transmits ballistic electrons for months without any significant deterioration. In general, the Schottky barrier homogeneity is a very important device characteristic, since in its absence, the integrated macroscopic Schottky barrier height extracted from the $I–V$ measurements might be quite different from the averaged BEEM threshold [119].

4.2. BEEM dependence on the surface topography

In the case of epitaxial $CoSi_2$ layers on Si, the average BEEM current depends on the surface reconstruction [120]. On the atomic scale, the BEEM corrugation was out of phase with the STM topography. This surface-induced contrast of BEEM was attributed to the atomic-scale variations of the energy distribution of tunneling electrons (local variations of the tunneling barrier). The in-situ BEEM measurements [93] of Au/Si(111) and Au/Si(100) interfaces show the BEEM current variations that correlate with the surface slope (larger BEEM current at atomic steps and grain boundaries), as shown in Fig. 29. This result was explained in terms of the larger density of surface states at flat Au surfaces. Electrons, tunneling from the STM tip to such surface states, will have a substantially lower probability of reaching the interface before scattering inelastically than those electrons that tunnel directly to empty bulk states. It was noted that the BEEM contrast effect has generally not been seen previously for Au on Si, possibly due to the morphology or orientation of the Au grains in those studies [121].

Recently, Weilmeier et al. [122] have successfully imaged the variations in the density of unoccupied surface states by conducting BEEM on Cu/Au, Ag/Au and Au/Cu/Au (111) overlayers UHV-grown on Si(100) and Si(111) substrates (a second (Cu or Ag) film overlayer, typically
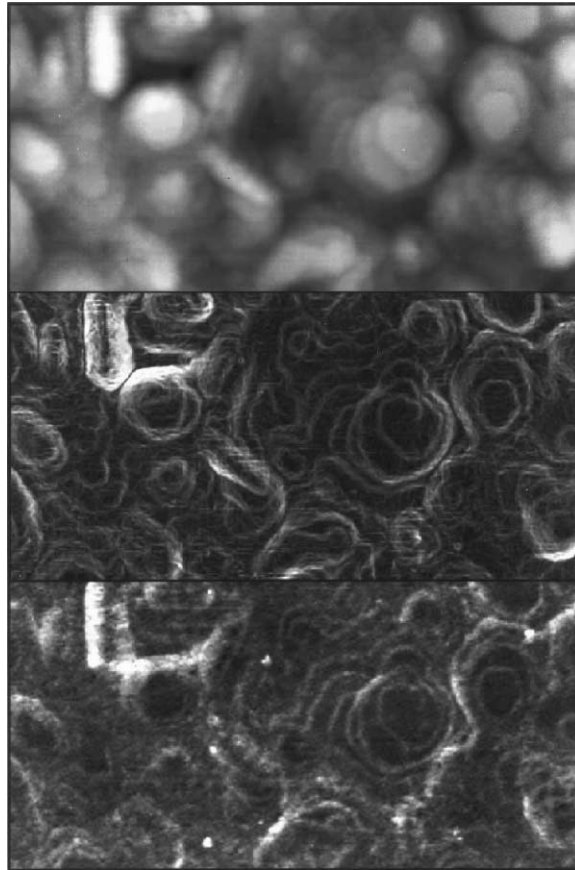
Fig. 29. STM and BEEM images of a 200 Å Au/Si(1 0 0) sample. The 100 nm × 350 nm images are obtained at $V_t = 1.1$ V and $I_t = 1$ nA. The top image is the STM surface height (17 Å white to black), the middle image is its calculated surface slope, and the bottom image is a map of BEEM current, I_c. The mean BEEM current is 2.25 pA, and total range shown is 2.4 pA. BEEM contrast is about 30% [93].

30–100 Å thick, was deposited on an initially deposited 100 Å Au(111) layer). The BEEM results were confirmed by STM spectroscopy that yields a high density of the conduction-electron surface states on the flat areas of the spiral-like Cu/Au,Ag/Au and Au/Cu/Au (111) grains. The BEEM current increased on grain boundaries where the density of the surface states is small. This effect was explained to be due to the preferentially (111) oriented growth of the Au film under UHV conditions. As a consequence of the Au band structure restrictions on the electron propagation in the normal-to-surface direction, higher current flows through the unoccupied surface states.

With polycrystalline metal films on GaP(110) [7,123] and GaAs(110) [118] substrates, the BEEM current was attenuated at grain boundaries, and this effect was attributed to elastic scattering decreasing the transmission rate into the semiconductor conduction-band-centered substrate. In those cases the metal band structure did not forbid electron transport normal to the surface, and thus there was no involvement of surface states.

4.3. BEEM-induced modification of carrier transport

The variation of interface transmission properties under hot electron injection was reported in BEEM experiments. Fernandez and Hellen et al. [4,124] first reported that the transmission properties of some specific Au/Si interfaces could be modified on the nanometer-scale when the energy of injected electrons was a few eV higher than the Fermi level of the metal base. It was pointed out that irreversible modification in the transmission rates for the buried interface can occur when the system is stressed with electrons injected at $V_t > 3$ V above the Schottky barrier. Spatially, the modification typically consists of a region of decreased transmittance of a few
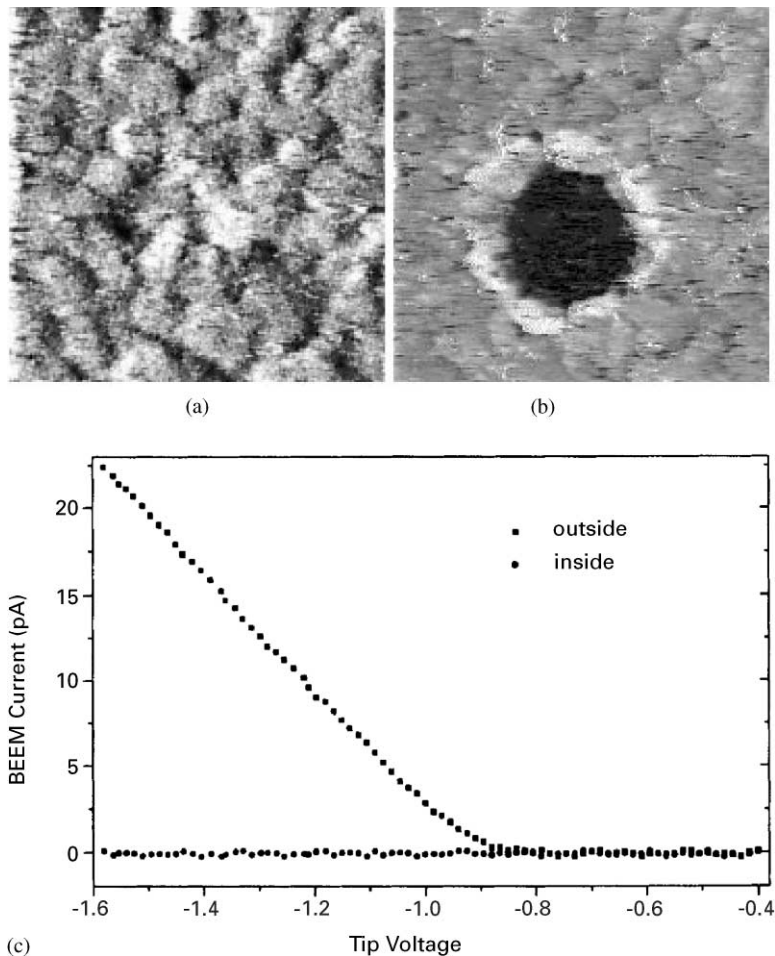

Fig. 30. Topographic and simultaneously acquired BEEM images with a tip bias $V_t = -1.30$ V and tunneling current $I_t = 2.5$ nA of an Au/n-Si(1 1 1) sample after modification operation. The image area is $800\,\text{Å} \times 800\,\text{Å}$. The applied voltage pulse is -4.0 V with a duration of 10 s. (a) STM topography of the Au surface. The gray-scale range is 20 Å. (b) Corresponding BEEM current image. The gray scale covers a range of 3–30 pA. (c) Spectroscopic measurements performed inside and outside the modified region reveal significant differences [125].

hundred Å in diameter surrounded by a ring of increased transmittance. A model was proposed in which the tunneling current at high bias enhances diffusion at the interface resulting in a change in the local atomic distribution.

Qiu et al. [125] reported on the observation of a series of fabricated interfacial features with significantly different characteristics. Under applied negative tip bias $V_t > 2.5$ V for several seconds in the Au/n-Si(100) and Au/n-Si(111) systems, a strong modification of the BEEM image occurred without noticeable change in the surface topography, as shown in Fig. 30. At the center of the modified zone there is a dark "hole" with zero BEEM current surrounded by a ring with enhanced BEEM current. The area of this hole increased nearly linearly with the exposure time (diameter increased from ~ 300 Å to ~ 450 Å when exposure time increased from 5 to 30 s at $V_t = -4$ V). A threshold pulse voltage of about 2.5–2.8 V has been observed in such a modification. When the electron energy was lower than this value, little change could be observed in the interface BEEM image, even with $I_t = 12$ nA and exposure time of several minutes. Thus the mechanism responsible for the modification requires an activation energy with the following accumulation of injected electrons (this is evident from the increase of the modified area with the exposure time). Also, surprisingly, when a voltage pulse of higher amplitude, $V_t = -5$ V for 20 s, was applied, the modified area shows higher transmittivity than the unmodified surface (Schottky barrier remains essentially the same). The authors concluded that the mechanisms proposed earlier (stacked Au terraces and Au/Si interdiffusion [124]) to explain the interface modification are not sufficient to account for all the observations.

Recently, Hasegawa et al. [121] have conducted BEEM study on Au/Si(111) where the Si substrate was chemically treated by dipping into 5% HF solution prior to gold deposition. They have shown that by applying a negative voltage of $V_t > 3$ V on the tip for several seconds, a local region was created where no BEEEM current flows at the interface. The modified area can be erased by applying a voltage with the opposite polarity (see Fig. 31). It is found that the minimum size of writing and erasing corresponds to Au grains, suggesting a method of rewritable memory on a nanometer scale. The possible origin of this effect is due to vacancies or due to the charging effects at the interface.

5. BEEM on buried semiconductor heterostructures

Although originally the BEEM technique was invented as a unique microscopic and spectroscopic method to probe the Schottky barriers on a local scale, the BEEM technique can be successfully used to study the electronic properties of *buried* heterojunctions. If there is an additional potential barrier (higher than the Schottky barrier) in the path of the injected carriers, the threshold should correspond to the height of this barrier. This is the essence of the heterojunction experiments using BEEM to probe the semiconductor band structure (spatially) beneath the m–s interface. The modeling of the BEEM transport in interference filter structures clearly demonstrated the potential of BEEM to probe buried quantum structures [126]. Recent research has proven that BEEM is a very powerful method for imaging and electron spectroscopy of buried defects and low-dimensional quantum structures.
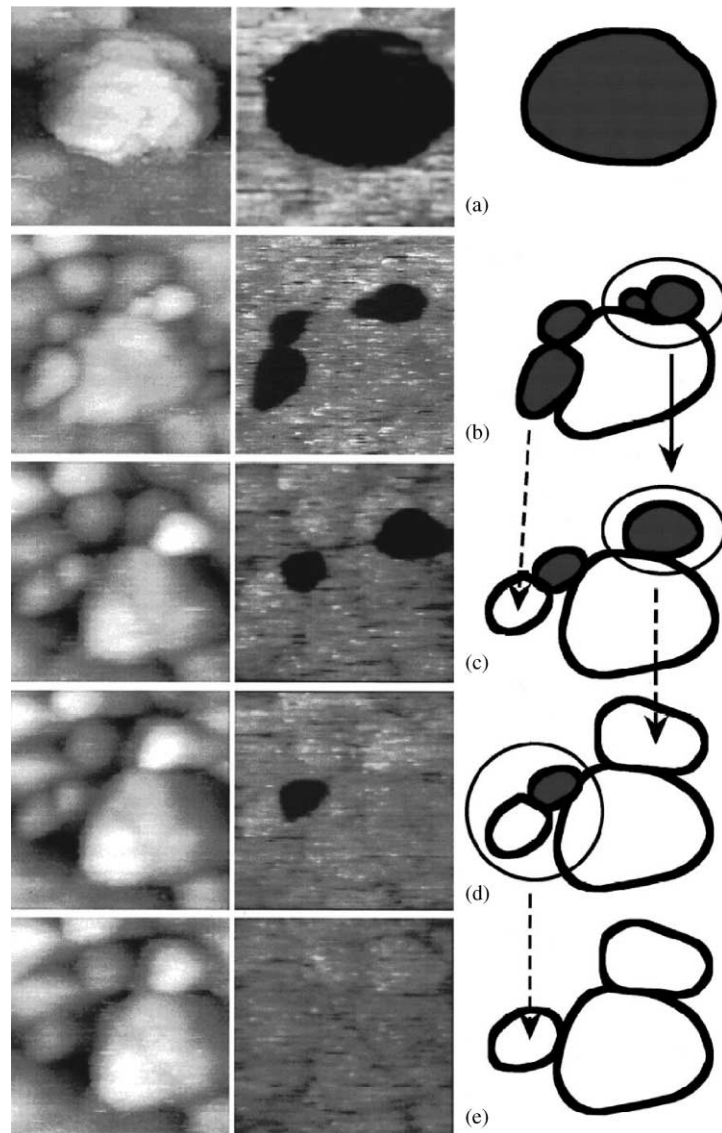
Fig. 31. Series of STM (left) and BEEM (middle) images during an erasing process of the Au/Si(1 1 1) interface. (a) Images taken before the process and (b)–(e) images taken after every scanning with a positive voltage of 1.34 V. The size of the images is 47 nm × 47 nm. Schematics shown on the right demonstrate a variation of Au grain structures with the BEEM current contrast together [121].

5.1. BEEM in simple metal/semiconductor structures

5.1.1. Metal/II–VI- and metal/IV-semiconductor systems

So far, only few BEEM studies were reported on metal/II–VI semiconductor systems. The BEEM technique was applied to measure the Schottky barrier contacts fabricated by evaporating

Au on as-grown n-ZnSe [104] and on chemically etched n-ZnSe [127] and CdTe [119]. BEEM studies in as-grown-prepared Au/ZnSe give relatively narrow Schottky barrier height distribution (1.32–1.43 eV) [128], in contrast to wide Schottky barrier height distribution (1.53–2.15 eV) found in Au/ZnSe diodes prepared by chemical etching [129].

For metal/IV semiconductor systems, one of the first applications of BEEM was the nanometer-scale study of ballistic transport in the metal/Si Schottky barrier system [23], and today this system is probably the most studied system in BEEM experiments and model calculations. Some BEEM results for this system were reviewed in Sections 2 and 3 of the current paper (see also previous review articles [2,3]).

Recently, BEEM study of group-IV semiconductors was extended to SiGe and SiC compounds. Bell et al. [12,130] had applied BEEM to study the effect of strain in metal/$Si_{1-x}Ge_x$/Si structures. The 500 Å $Si_{1-x}Ge_x$ layers ($x = 0.18$ and 0.25) were pseudomorphically strained (well below the critical thickness). The presence of strain modifies the $Si_{1-x}Ge_x$ band structure. Whereas Au/ Si(100) BEEM spectra show a single threshold, the Au/$Si_{1-x}Ge_x$/Si BEEM spectra usually exhibited two thresholds (a splitting of ~ 0.3 eV at $x = 0.25$). These thresholds were attributed to the strain-induced conduction band splitting of $Si_{1-x}Ge_x$. The threshold positions as a function of the splitting were found to follow the theoretical work of Van de Walle and Martin [131], who predicted that the four strain-equivalent conduction band minima in the layer plane are lowered in energy, while the two minima normal to the plane are raised in energy. Based on BEEM results, the spatial distribution of strain in $Si_{1-x}Ge_x$ layers was found to be very heterogeneous (conduction band splitting varied from 0 to 0.35 eV from point to point across the sample surface). This characteristic was explained in terms of the Au/$Si_{1-x}Ge_x$ interface roughening by Au–Si interdiffusion. Indeed, in the case of Ag/$Si_{1-x}Ge_x$ where the interface is smooth, the observed splitting was uniform [130].

In the case of SiC, which is a technologically important IV–IV compound wide-bandgap semiconductor, the Schottky barrier height was studied for (Pd,Pt)/6H-SiC (1.27 eV, 1.34 eV) and (Pd,Pt)/4H-SiC (1.54 eV, 1.58 eV) [21,22]. In 4H-SiC, an additional CBM was observed at ~ 0.14 eV above the lowest conduction band minimum. Enhanced ballistic transmittance (without significant change of the Schottky barrier) was observed over a region intentionally stressed by injecting high-kinetic-energy hot electrons (10 eV above the Fermi level) using BEEM in the Pt/4H-SiC system.

5.1.2. Metal/III–V semiconductor systems

The BEEM technique was extensively applied to study Schottky barriers and hot electron transport peculiarities in many metal/III–V semiconductor structures, e.g. Au/GaAs [5, 29, 49, 84, 116], (Au,Mg,Cr)/GaP [7,64], Au/InAs [132–134], (Au,Co)/$GaAs_{0.67}P_{0.33}$ [100] and Al/AlSb [135]. In this section, we will discuss the very recent BEEM results in several important compound semiconductors such as GaN, GaInP and GaAsN.

5.1.2.1. GaN. Although GaN exhibits high-efficiency optical performance despite its extremely high dislocation densities [136], the dislocations are very likely to have significant electrical and structural impact on high-power electronic devices.

Recent study of Brazel et al. [18] has revealed high BEEM current densities and low effective Schottky barrier heights in small localized areas around dislocations with a screw component. The GaN-films used in that study were grown by metal organic vapor deposition (MOCVD) at
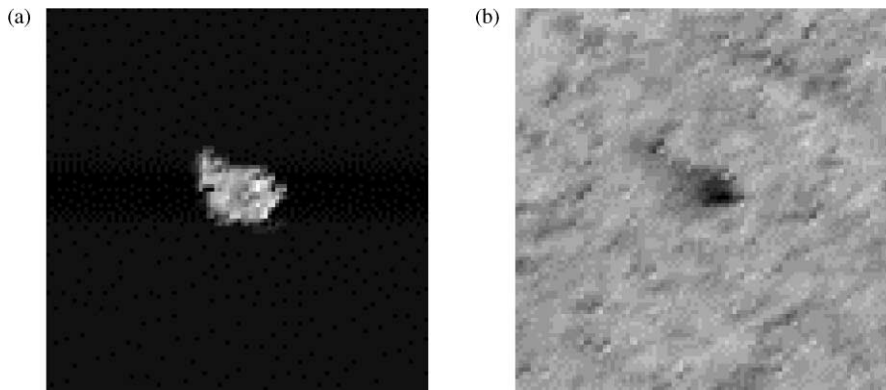
Fig. 32. Collector current image (a) and simultaneously taken STM image (b) of the 70 Å Au cap layer of a 2500 Å × 2500 Å area ($I_t = 1$ nA, $V_t = -1.8$ V). The small high-current area (~ 500 pA, bright spot) surrounded by areas with zero collector current (< 0.2 pA) shown in (a) is typical for the investigated GaN-films. The Au layer (right) exhibits a pit (dark) at the location of the high-current area (bright spot (a)) [18].

atmospheric pressure. For these measurements unintentionally doped, n-type GaN-films of thickness ranging from 1 up to 3 μm were deposited on c-plane sapphire substrates. Fig. 32(a) shows a typical collector current distribution for the MOCVD-grown GaN films deposited on c-plane sapphire substrates. From most parts of the sample no collector current was detectable (dark area), and only in small localized spots, like the shown light area, high collector currents could be observed. In this representative case, the measured current was ~ 500 pA, which is half of the injected 1 nA tunneling current. To localize the high current areas on the sample surface and possibly correlate them with surface features, images of the current distribution and the topography were taken simultaneously. Fig. 32(b) shows the STM image of the Au cap-layer, which corresponds to the collector current image in Fig. 32(a). The 70 Å thick Au-layer exhibits a ~ 500 Å wide pit at exactly the same position of the high current area in the collector current image. An AFM-image taken of the same sample shows several of these pits that represents the surface terminations of mixed and pure screw dislocations. Thus, it was concluded that the high BEEM current areas are located at dislocations with screw character. To get information about the Schottky barrier heights, the BEEM spectroscopy in both high and low currents areas was carried out. The low current areas do not show any measurable collector current, whereas for the high current areas, we have found barrier heights in the range from ~ 0.3 up to ~ 0.95 eV. The threshold values vary within one high-current area and from area to area. In addition, it was possible to reverse the tunneling voltage and inject holes into the very same high current areas as well, with the observed threshold energy of ~ 0.3 to 1.3 eV, as shown in Fig. 33. The observed thresholds for carrier injection do not seem to be typical Schottky barriers, but rather capturing barriers of trap states in the vicinity of the dislocations. These results definitely suggest that acceptor- and donor-like trap states coexist in the same area, and are being filled during carrier injection into the GaN. The maximum threshold energies observed for electrons (0.95 eV) and holes (1.3 eV) add up to 2.25 eV, remarkably close to the parasitic yellow luminescence commonly observed in GaN. In the future, we plan to conduct more experiments to answer the question whether the same
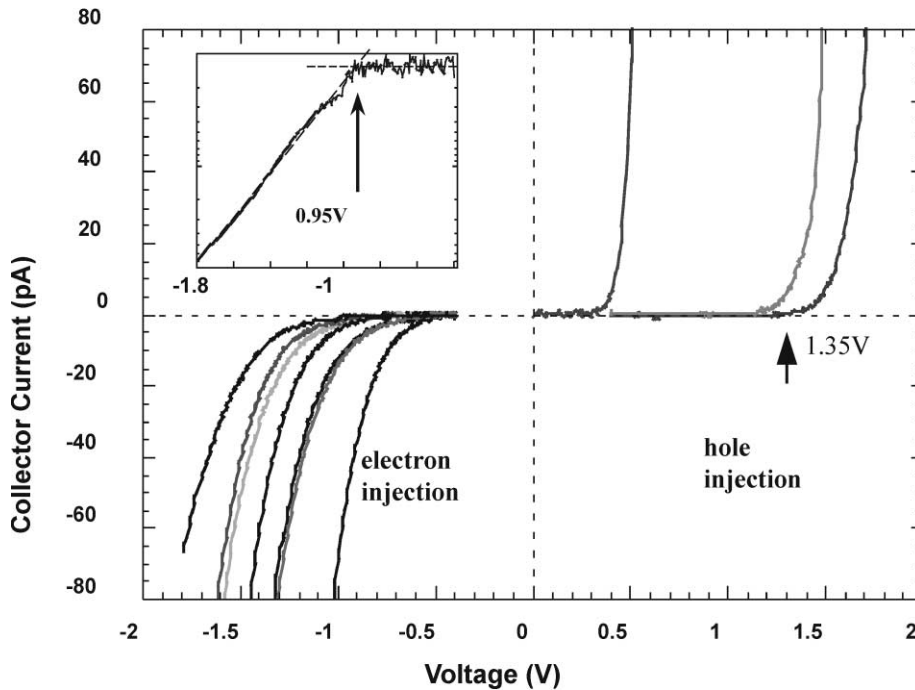
Fig. 33. BEEM spectra for electron and hole injection. Log-plots like the one shown in the inset were used to approximately determine the threshold voltage necessary for current injection into the high-current areas [18].

electronic states, which are causing the high current densities are also responsible for the yellow luminescence.

Bell et al. [17,19,137] also studied metal/GaN Schottky barriers. The GaN layer of ~ 2 μm thickness was grown by MOCVD on a (000 1) sapphire substrate. After several attempts, they succeeded in measuring the BEEM current in the Au/GaN and Pd/GaN systems if the GaN surface had been spin etched using 1:10 HCl:ethanol solution prior the metal deposition. Two thresholds were observed in the BEEM spectra (~ 1 and 1.2 eV) [17]. The first threshold was interpreted to be the Schottky barrier (consistent with the conventional macroscopic I–V measurements), while the origin of the second threshold might be due to the strain-induced conduction band splitting. Imaging of the Au/GaN interface reveals transmission in nearly all areas, although the magnitude is small and varies by an order of magnitude (0.2–2 pA at $I_t = 2$ nA), as shown in Fig. 34. It was shown that if the HCl/ethanol treatment of the GaN surface is followed by sample annealing in UHV or in N_2 prior Au deposition, much higher and more uniform transmission across the Au/GaN interface can be achieved [19]. However, while the GaN annealing resulted in more than one order of magnitude increase of the BEEM current, it also resulted in undesired alteration of the Schottky barrier height. Fig. 35 shows to reduction of the Schottky barrier from ~ 1.06 V to ~ 0.92 and to ~ 0.69 V after UHV annealing for 15 min at 340 and 580°C, respectively. These barrier height changes were interpreted in terms of creation of vacancies or their diffusion toward the GaN surface.
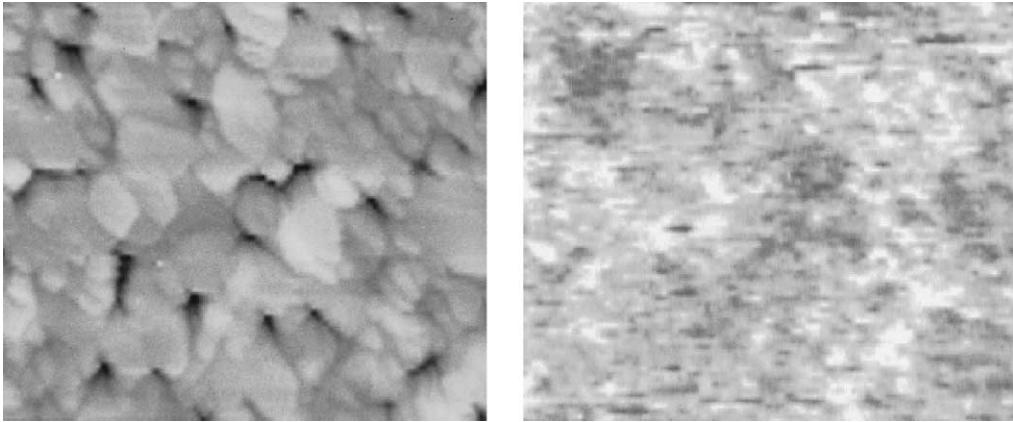
Fig. 34. STM topography/BEEM image pair for a Au/GaN sample. The topography of the Au surface was obtained at $V_t = 0.5$ V, $I_t = 1$ nA, and the BEEM image was recorded at $V_t = 1.8$ V, $I_t = 2$ nA. Topographic height range is 9 nm, and I_c ranges from about 0.2 to 2 pA; imaged area is 190×160 nm [137].
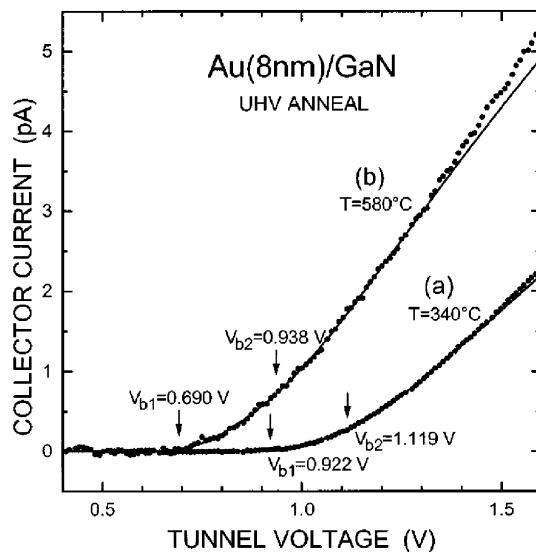

Fig. 35. BEEM spectra for two different Au (8 nm)/GaN samples. (a) Spectrum for a sample annealed in UHV at 340°C for 15 min. (b) Spectrum for a sample annealed at 580°C. Here transmission is increased, and barrier height is substantially decreased [19].

5.1.2.2. GaInP. In the past decade, spontaneous CuPt ordering of many III–V alloys has been widely observed in vapor phase growth on (001) substrates. In $Ga_{0.52}In_{0.48}P$ (written as $GaInP_2$ for simplicity), extensive theoretical [138,139] and experimental [140] work has been carried out to study the effect of the ordering-induced reduction of the crystal symmetry on the structural, optical and transport properties of the ordered material. Ordering induced changes in the band structure

of GaInP$_2$ are important for its application in advanced solar cells with very high conversion efficiency, for potential band-gap engineering and for fundamental studies of atomic ordering.

Perfectly ordered material has not been observed. The electronic states of a partially ordered structure can be interpolated from those of the totally disordered and the perfectly ordered semiconductor [139]. The degree of ordering is usually described by the ordering parameter η, where $E_g(\eta) = E_g(\eta = 0) - \eta^2 \Delta E_g(\eta = 1)$, with $\eta = 0$ and 1 to describe perfectly disordered and perfectly ordered material, respectively. $E_g(\eta = 0)$, the bandgap of disordered GaInP$_2$, is 2.01 eV at low temperature [141] and $\Delta E_g(\eta = 1)$, the maximum bandgap reduction for perfectly ordered GaInP$_2$, is 0.47 eV [142]. In the most ordered GaInP$_2$ structures, the highest ordering parameter $\eta \sim 0.6$ [143], and the degree of ordering is nonuniform on the local scale.

To characterize the structural and electronic properties of GaInP$_2$, we have applied the BEEM technique [15,16]. The undoped GaAs/GaInP$_2$ structures on n$^+$- and p$^+$- GaAs substrates were grown by MOCVD at $T_g = 650°$C. The structures consist of a 500 Å undoped GaAs buffer layer, a 1 μm GaInP$_2$ and a 50 Å GaAs cap layer. The details of the diode fabrication procedure have been published elsewhere [29]. A detailed analysis is presented here for the GaInP$_2$ samples grown on a (511) GaAs substrate and on a (001) GaAs substrate misoriented 6° toward [111]$_B$. From the low-temperature photoluminescence, the bandgap energy (after correction on the exciton binding energy) is ~2.00 eV for GaInP$_2$ grown on a (511) GaAs substrate and ~1.88 eV for GaInP$_2$ grown on a 6°[111]$_B$-(001) GaAs substrate. Therefore, we conclude that the GaInP$_2$ layer grown on a (511) GaAs substrate is highly disordered (hereafter, disordered GaInP$_2$) and the GaInP$_2$ grown on a (001) GaAs substrate misoriented 6° toward [111]$_B$ is highly ordered, $\eta \sim 0.5$ (hereafter, ordered GaInP$_2$) [139].

Fig. 36 shows room-temperature 1 μm × 1 μm STM images of the disordered (a) and ordered (b) GaInP$_2$ layer grown on n$^+$-GaAs substrates. One can see that the surface of ordered material forms [110]-oriented steps. For ordered GaInP$_2$ grown on misoriented substrates, the [110] steps are usually observed to form only single CuPt variant [144,145]. For disordered GaInP$_2$, the surface is found to be much flatter than that of ordered GaInP$_2$. The complementary BEEM images are also shown in Fig. 36. The observed contrast of the BEEM image for the ordered GaInP$_2$ sample is in direct correlation (antiphase) with the surface morphology, indicating high sensitivity and high spatial resolution of the BEEM technique.

To study the heterostructure transmission coefficient, we analyze the SD-BEEM spectra rather than the original BEEM spectra [16]. Fig. 37 shows the SD-BEEM spectra obtained from the experimental BEEM data by numerical differentiation with a 10 meV window. We associate two clearly pronounced features in the 77 K SD-BEEM spectra of disordered GaInP$_2$ with the Γ and L conduction minima contribution in GaInP$_2$. Theoretical fits to the SD-BEEM spectrum for the disordered GaInP$_2$ sample, using the MSIS model [5,85], are shown in Fig. 37 by the dashed line. The MSIS model fit describes the experimental BEEM spectrum reasonably well, giving ~90% probability of the electron scattering at the m–s interface, similar to our previous results for GaAs/AlGaAs structures [5]. The absence of a contribution from the X conduction minimum is due to strong X-electron attenuation in the GaAs cap layer [5].

The SD-BEEM spectrum of the ordered GaInP$_2$ sample presented in Fig. 37 show a very important difference from that of the disordered GaInP$_2$. Namely, we observe two high-energy peaks instead of one peak in disordered GaInP$_2$. We assign both high-energy peaks to be associated with the L valley contribution. In CuPt-type ordered GaInP$_2$, one of the four L valleys
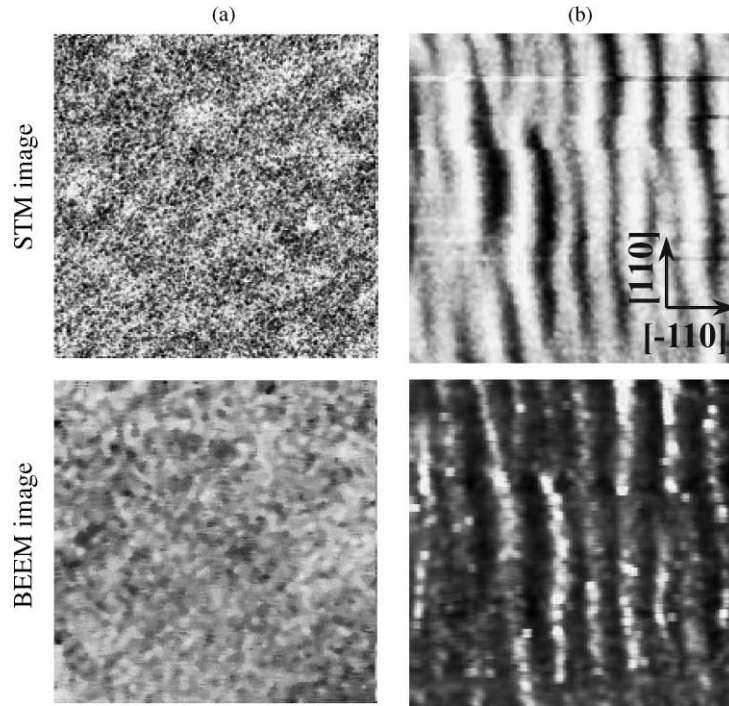
Fig. 36. Room-temperature 1 μm × 1 μm STM image (top) and BEEM image (bottom) of GaAs/GaInP$_2$ layer grown by MOCVD on (a) (5 1 1) n-GaAs substrate, (b) on n-GaAs substrate misoriented by 6° to [111]$_B$. A tip bias is − 1.7 V and a tunnel current is 4 nA [16].
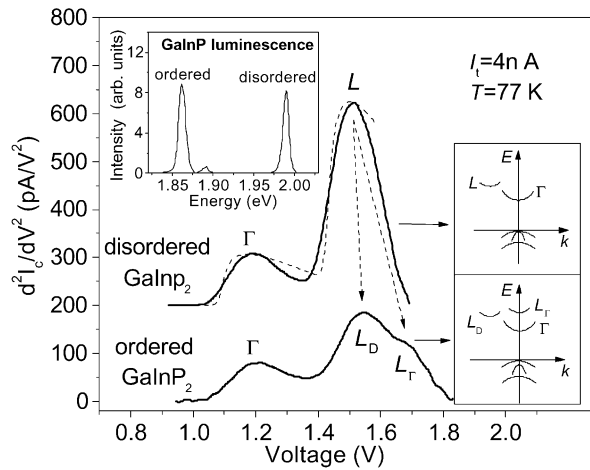

Fig. 37. SD-BEEM spectra for two GaAs/GaInP$_2$ (ordered and disordered) samples with 50 Å GaAs cap layers, taken at $T = 77$ K. For clarity, the spectra are shifted along the vertical axis. The MSIS model calculations are also presented (dashed line). The top inset shows the photoluminescence spectra for both ordered and disordered GaInP$_2$ samples, whereas two bottom insets show the schematic of the GaInP$_2$ band structure [16].

folds onto the $\bar{\Gamma}$ point (hereafter L_Γ), and the other three are folded onto the $\bar{D}$ point (hereafter L_D). A strong repulsion between the Γ valley and the folded L_Γ valley results in the bandgap reduction and in the increase of the Γ–L_Γ separation, while the energetic position of the L_D remains almost the same. Therefore, we conclude that the two observed high-energy peaks for the ordered sample are the contribution of the L valleys that are split due to ordering.

The "folded" zone-edge bands were observed experimentally in electro-reflectance [146] and Raman spectroscopy [147] measurements. In the recently reported electro-absorption experiments on ordered GaInP$_2$ ($\eta \approx 0.45$) [148], an additional feature was observed at ~ 0.48 eV above the fundamental bandgap transition, and this feature was attributed to the back folded L conduction band. As the ordering decreases, this peak shifts to lower energies, with an asymptotic value of ~ 0.33 eV above the fundamental bandgap transition for a totally disordered sample. In Refs. [146–148], due to the selection rules, only the contribution from the L valley folded onto the $\bar{\Gamma}$ point was observed. In contrast, we observe the contribution from all L valleys and, as a consequence, can measure directly the Γ–L separation in disordered GaInP$_2$ as well as the ordering-induced L valley splitting in ordered GaInP$_2$. According to our results, $\Delta(\Gamma$–$L) \cong 0.35$ eV for a disordered sample, $\Delta(\Gamma$–$L_\Gamma) \cong 0.47$ eV and $\Delta(L_\Gamma$–$L_D) \cong 0.13$ eV for an ordered sample. These results are in a good agreement with the theoretical predictions. Indeed, as pointed out by Zunger [149], it is possible to obtain the dependencies $\Delta(\Gamma$–$L_\Gamma) = \Delta(\Gamma$–$L)_{\eta = 0} + 0.50\eta^2$ and $\Delta(L_\Gamma$–$L_D) = 0.42\eta^2$, using Table 1 and Fig. 3(b) of Ref. [150]. Then, taking $\eta = 0.5$ and $\Delta(\Gamma$–$L)_{\eta = 0} = 0.35$ from our experiment, $\Delta(\Gamma$–$L\Gamma) \cong 0.475$ eV and $\Delta(L_\Gamma$–$L_D) \cong 0.11$ eV.

5.1.2.3. GaAsN. Recently, a new class of III–V alloys, where small amounts of nitrogen replace the group V-element, has attracted a great deal of attention because of the observation of a giant bandgap reduction. In the case of dilute GaAs$_{1-x}$N$_x$, for example, the bandgap is reduced by more than 0.4 eV at $x \sim 0.04$, indicative of a colossal bandgap bowing parameter [151–155]. Such a large tuning range suggests also a great potential for such alloys for a variety of optoelectronic applications [156,157].

To shed new light on the GaAs$_{1-x}$N$_x$ band structure we have applied the BEEM technique to study the electron transport in the conduction band of GaAs$_{1-x}$N$_x$ alloys [20]. A 1000 Å undoped GaAs$_{1-x}$N$_x$ layer and 1000 Å n$^+$-GaAs buffer layer were grown on n$^+$ (001)-oriented GaAs substrates by gas source molecular beam epitaxy at 420°C (the details of the growth conditions were published elsewhere [158]). A detailed analysis is presented here for a set of Au/GaAs$_{1-x}$N$_x$/n$^+$-GaAs with the nitrogen compositions of $x = 0, 0.003, 0.005, 0.007, 0.012, 0.017$ and 0.021. The composition of GaAs$_{1-x}$N$_x$ layers was determined from dynamic simulations of the X-ray diffraction spectra. High-resolution X-ray diffraction data also demonstrated that these layers are indeed single-phase alloys, in accordance with previous photoluminescence studies that have indicated the alloy formation already at $x > 0.001$–0.0025 [159,160]. To make the Schottky contacts, Au layers (65 Å thick) were deposited by thermal evaporation through a shadow mask at a background pressure of 2×10^{-7} Torr. The details of the diode fabrication procedure have been published elsewhere [29].

Fig. 38 shows the room-temperature BEEM spectra of GaAs$_{1-x}$N$_x$ for seven different nitrogen compositions. For all nitrogen compositions except $x = 0$, one can distinguish two thresholds in BEEM spectra. As the nitrogen concentration increases, the low-energy threshold shifts towards lower voltages whereas the high-energy threshold shifts towards higher voltages (the thresholds'
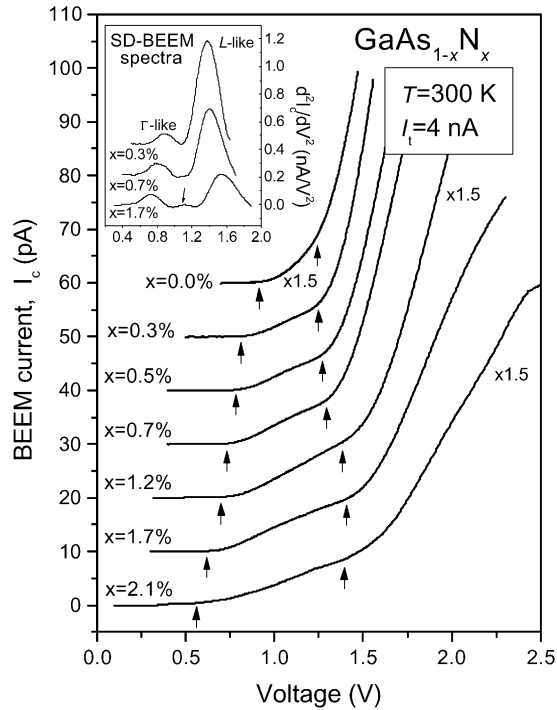
Fig. 38. Room-temperature BEEM spectra for seven different nitrogen compositions (from 0 to 0.021). For clarity, the BEEM spectra are shifted along the vertical axis. Arrows are eye-guides for the peaks position development. Insert shows the corresponding representative SD-BEEM spectra for three different nitrogen compositions (0.003, 0.007 and 0.017) [20].

development is shown by arrows in Fig. 38). This behavior is very different from our previously reported BEEM studies of AlGaAs [5] and GaInP$_2$ [16], where only the first threshold (counting from low voltages) can be unambiguously seen from the original BEEM spectra (all additional thresholds are visible to the naked eye only in the SD-BEEM spectra).

The representative room-temperature SD-BEEM spectra extracted from the experimental BEEM spectra by numerical differentiation with a 10 meV window are shown in the inset of Fig. 38. Two main features (peaks) observed in the SD-BEEM spectra we associate with the Γ-like and L-like conduction minima in GaAs$_{1-x}$N$_x$. Indeed, it is apparent from Fig. 38 that these peaks originate from gradually moving apart the Γ and L peaks of GaAs identified in our previous study [5]. The BEEM weighting of the different bands is proportional to their DOS's [85], and since nitrogen substitution results in the splitting of the fourfold L valley into the $a_1(L_{1c})$ singlet and $t_2(L_{1c})$ triplet states [161,162], the L-like band in the BEEM experiments is mostly weighted on the $t_2(L_{1c})$ triplet state. The SD-BEEM spectra of two GaAs$_{1-x}$N$_x$ samples, $x = 1.2$ and 1.7 (see inset of Fig. 38), reveal an additional weaker peak (indicated by the arrow), located ~ 0.40 and ~ 0.43 eV above the Γ-like state, respectively. (At lower nitrogen concentrations, this peak is probably masked due to the insufficient Γ-like and L-like peaks separation, whereas at higher nitrogen concentrations, due to the alloy-scattering-induced signal decrease, our sensitivity is too low to extract reliably the SD-BEEM spectra). This peak might represent the contribution from the
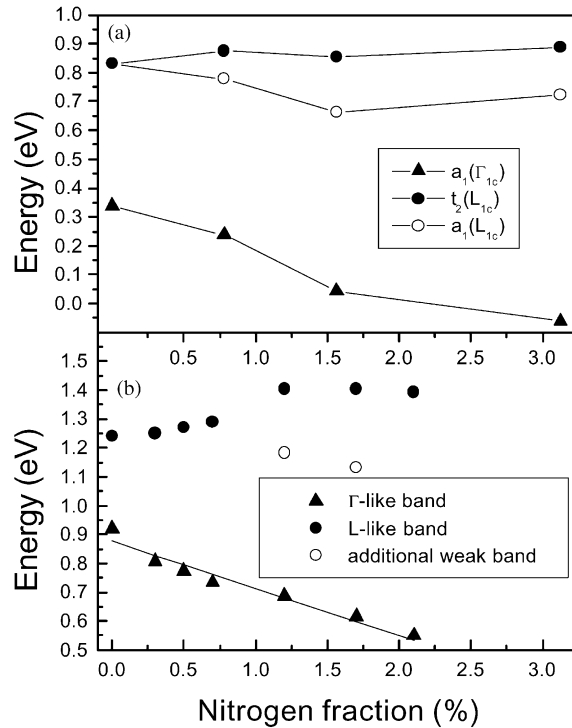
Fig. 39. (a) First-principles LDA calculations of the Γ_{1c} and L_{1c} compositional dependencies of GaAs$_{1-x}$N$_x$. (b) The compositional dependencies of the thresholds observed in the SD-BEEM spectra of GaAs$_{1-x}$N$_x$. The solid line is the best linear fit to the Γ-like threshold giving a slope of -16.4 eV [20,164].

$a_1(L_{1c})$ singlet state. The weaker amplitude of this peak matches the expected small DOS due to the increasing Γ-character of the $a_1(L_{1c})$ state in the alloy limit [163]. The compositional dependencies of the thresholds observed in the SD-BEEM spectra plotted in Fig. 39(b) are in a good agreement with recent first-principles theoretical calculations [164] presented in Fig. 39(a). The alternative L-like band identification as a localized resonant nitrogen level (see Ref. [165]) is very unlikely because in this case one would expect a resonant nitrogen-level contribution to increase with the nitrogen concentration (larger DOS), whereas the experimentally observed high-energy peak amplitude decreases with the nitrogen concentration. The absence of the X conduction minimum contribution in GaAs$_{1-x}$N$_x$ is due to the image potential-induced strong electron scattering in the spacer between the metallurgical m–s interface and the maximum of the barrier height [2], similar to our previously reported results [5].

As the nitrogen concentration increases, the Au/GaAs$_{1-x}$N$_x$ Schottky barrier (Γ-like threshold) decreases considerably, from ~ 0.92 eV at $x = 0$ down to ~ 0.55 eV at $x = 0.021$, as shown in Fig. 39(b). The solid line in Fig. 39(b) is the best linear fit to the experimental data (with a slope of -16.4 eV). Using $E_g(\text{GaAs}) = 1.42$ eV and $E_g(\text{GaN}) = 3.5$ eV at room temperature, the same slope of $E_g(\text{GaAs}_{1-x}\text{N}_x)$ would correspond to the bowing parameter of -18.9 eV. This value of the E_g bowing parameter is in a good agreement with the experimental estimates [152,166,167]. Thus, we conclude that the nitrogen-induced Schottky barrier reduction follows approximately the

bandgap reduction in $GaAs_{1-x}N_x$. This result, that is very important for device applications, indicates that the effect of the nitrogen incorporation on the valence band is small, in agreement with other studies [156,161].

5.2. BEEM spectroscopy to study band offsets in buried semiconductor heterostructures

To engineer useful heterojunction-based devices and predict their performance, the values of the band offsets must be accurately known. While originally invented to study Schottky barriers, BEEM spectroscopy can be effectively employed for the band offset measurements by comparative study of a reference metal/semiconductor system (e.g. Au/GaAs) and of an essentially similar system but with a buried semiconductor barrier beneath the m–s interface (e.g. $Au/GaAs/Al_xGa_{1-x}As$). In such a way, the band offset is obtained by subtracting the BEEM threshold of the reference sample from the BEEM threshold of the sample with the buried heterojunction barrier. Such structures have the advantage that the m–s (e.g. Au/GaAs) interface is invariant and allows a systematic comparison to be made as one varies the nature of heterostructure and alloy composition. In addition, BEEM offers certain advantages as compared to the standard techniques for the heterojunction band offset measurements, such as interband optical and macroscopic electrical techniques. Namely, BEEM allows independent measurements of the conduction band offset (ΔE_c) and the valence band (ΔE_v) offsets of "unbiased" heterojunctions as well as allows a high locality of the band-offset measurements. Spatially resolved BEEM spectroscopy is especially useful to study the band offsets of localized buried heterostructures, which are too small to contact by traditional methods (for example, see Section 5.4.3.2 for the BEEM study of buried GaSb quantum dots embedded into the GaAs matrix).

O'Shea et al. [29] have applied BEEM spectroscopy to measure band offsets in buried $GaAs/Al_xGa_{1-x}As$ heterojunction for $0 \leq x \leq 1$. For the single barrier case (see Fig. 40(a)), the $Al_xGa_{1-x}As$ barrier height was altered by systematically varying the Al composition. The barrier thickness was 100 Å and the GaAs capping layer was also 100 Å. Be δ-doping in the GaAs capping layer was used to flatten the conduction band. The conduction band offset first rises linearly to a maximum of ∼0.35 eV at $x \sim 0.4$ and then falls gradually to ∼0.3 eV at $x = 1.0$. This behavior is a consequence of the fact that $Al_xGa_{1-x}As$ is a direct semiconductor at $x \leq 0.42$ and an indirect one at $x \geq 0.42$. In the direct regime ($x \leq 0.42$), it was shown that the band offset of $\Delta E_c/\Delta E_g = 0.68$ measured by BEEM spectroscopy (see Fig. 40(c)) is in a good agreement with previous measurement by other techniques, thus demonstrating the accuracy of the BEEM spectroscopy technique. It was found that the conduction band-offsets are the same at $T = 300$ and 77 K. This result is in reasonable agreement with another BEEM study that was performed on a $Au/GaAs/Al_{0.2}Ga_{0.8}As/GaAs$ single-barrier structure at $T = 7$ and 77 K [32], $Q_c = 0.58$ (0.60) at $T = 77$ K (7K). Note that, in addition to the band-offset measurements, the Au/GaAs/$Al_xGa_{1-x}As$ system was extensively studied for different aspects of multivalley electron transport in $Al_xGa_{1-x}As$ (Refs. [29,49,168]) as well as for quantitative analysis of the electron scattering at the m–s interface (see Section 2.4).

O'Shea et al. [169] have also employed BEEM to study the conduction band and valence band offsets in $GaInP_2/GaAs$ single barrier heterostructures that are very promising to use in lasers, light-emitting diodes, heterojunction bipolar transistors, and solar cells. (To optimize these devices, control and understanding of the interface properties are essential. Yet, such fundamental
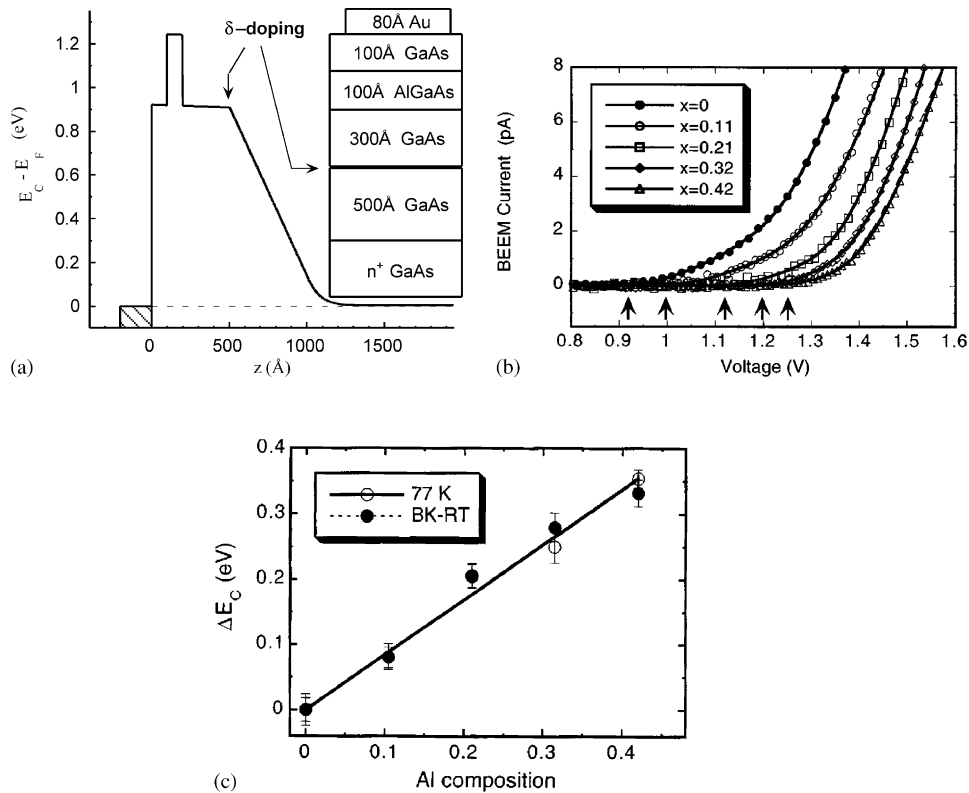
Fig. 40. (a) Calculated conduction band profile for $Al_xGa_{1-x}As$ ($x = 0.42$) single barrier structure assuming a Au/GaAs Schottky barrier of 0.92 eV. $T = 300$ K. The δ-doped sheet (Be, 1.1×10^{12} cm^{-2}) was used to flatten the bands. The MBE layer structure is shown in the inset. (b) Comparison of room-temperature (RT) BEEM spectra (point) for $Al_xGa_{1-x}As$ single barriers. Also shown are BK fits to the data (lines). Note the shift in the initial BEEM threshold (arrows) with Al composition gives the conduction-band offset. (c) RT and 77 K $Al_xGa_{1-x}As$ conduction-band offsets (points) measured by BEES. Linear fits (lines) at both temperatures give $\Delta E_c = (0.84$ eV$)x$, or a fractional band offset of $Q_c = \Delta E_c / \Delta E_g = 0.68$. The linear curve fits and some data points are overlapping [29].

parameters as heterojunction band offsets are not well understood. Experimentally, values of conduction band offsets ranging from 30 to 390 meV have been reported [170]. Since the bandgap of $GaInP_2$ changes with the ordering parameter, it is likely that ordering is responsible for some of the variation in previous ΔE_c measurements.) The calculated band profiles and layer structures for the n- and p-type $GaInP_2$/GaAs single barrier samples grown by MOCVD at atmospheric pressure are given in the upper panel of Fig. 41. The δ-doping sheet concentration was calculated to cancel the band bending at room temperature near the Schottky barrier enabling a measurement of flat-band heterointerfaces. The GaAs buffer layers were grown at 650°C, and the susceptor temperature was ramped down to 610°C after the δ-doping for the $GaInP_2$ layer growth. BEEM spectra for the $GaInP_2$ single barriers on n- and p-type GaAs substrates are shown in the lower panel of Fig. 41. The BK model was used as a consistent procedure to determine the thresholds. Although the exact value of each threshold will depend on the model applied, the difference
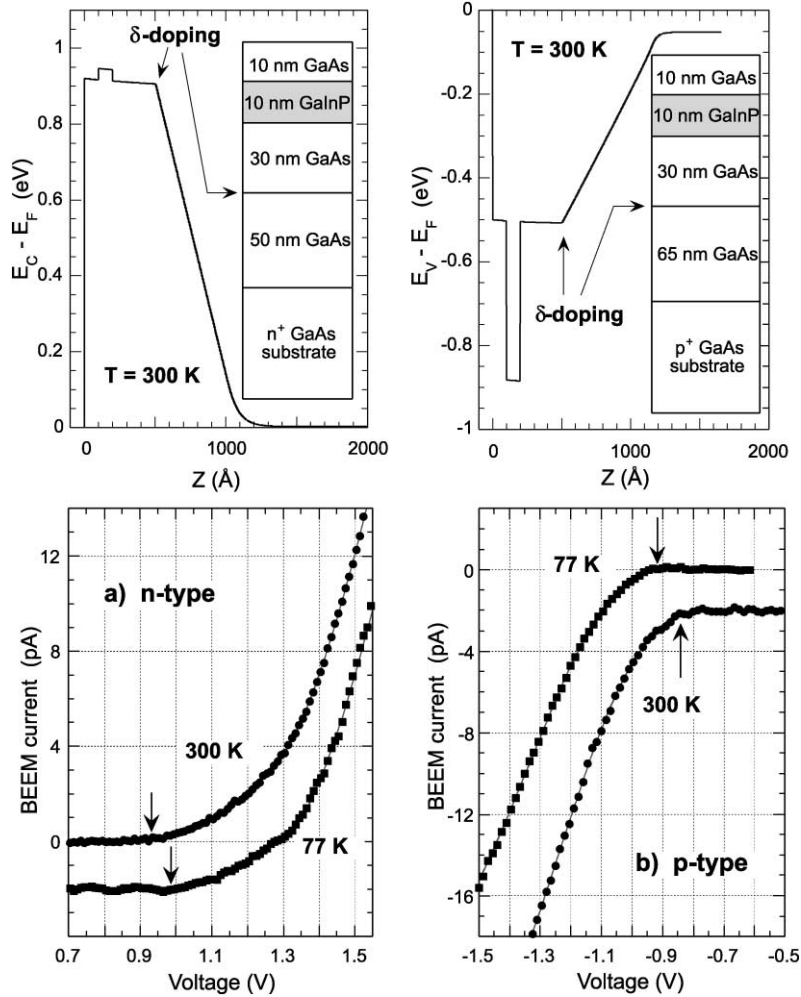
Fig. 41. Upper panel shows the calculated band profiles for n- and p-type GaInP$_2$ single barrier structures (the MOCVD layer structures are given in the inserts). Lower panel shows representative BEEM spectra (points) for (a) n- and (b) p-type samples containing GaInP$_2$ layers grown at 610°C. Lines are fits to the BK model to determine the thresholds, indicated by arrows. Curves offset by 2 pA for clarity [169].

between the BEEM thresholds of the single barrier sample and the reference sample should be model-independent. Thus, the band offsets are obtained by subtracting the BEEM threshold of the GaAs reference samples from the BEEM threshold of the GaInP$_2$/GaAs samples. GaInP$_2$/GaAs band offsets of 30 and 350 meV in the conduction and valence bands, respectively, were found at room temperature. Similarly, 77 K band offsets are 30 and 390 meV in the conduction and valence bands, respectively. Also, using the above BEEM results, it was possible to estimate the ordering parameter in the samples under study. Assuming that the sum of the n- and p-type BEEM thresholds should correspond to the GaInP$_2$ band gap, the BEEM measurements at

both 77 and 300 K give a bandgap reduction of ~ 0.1 eV compared to fully disordered GaInP, and this corresponds to an order parameter of $\eta \sim 0.45$.

The BEEM technique has been also applied to the Au/n-InAs/GaAs system to study the conduction band offset formation between InAs and GaAs as the thickness of the InAs was varied between 0 and 40 monolayers [132,133]. The band offset between InAs and GaAs was found to decrease with the InAs thickness. One monolayer of InAs lowers the barrier from ~ 0.9 (original Au/GaAs barrier) to ~ 0.8 eV. As the thickness of the InAs layer increases to three monolayers, the barrier was found to decrease further to ~ 0.74 eV. The barrier height remains approximately constant for up to 27 monolayers, and then it reduces to ~ 0.63 eV for the case of 33 monolayers (100 Å) and beyond. The detailed variation of the band offset was shown to correlate with the relaxation of the InAs layer, i.e. conduction band offset between strained InAs on GaAs depends on the strain, and it decreases as the strain relaxates through islanding.

Recently, BEEM spectroscopy has been successfully applied to determine the conduction band offset between AlInGaAs strained layer (active layer in 850 nm vertical cavity lasers) and a AlGaAs barrier located beneath the surface [30]. Also, BEEM spectroscopy has been used to study both the conduction and valence band offsets between InAs and AlAsSb at $T = 77$ and 300 K [31]. It was found that with the addition of As to AlSb, the conduction band offset between InAs and AlAsSb decreases despite the increase in the bandgap. The resulting decrease in the valence band position causes the InAs/AlAsSb band lineup to change from a staggered (type II) to a straddling (type I).

5.3. BEEM spectroscopy to study resonant semiconductor structures

5.3.1. Double barrier structures

The first BEEM study of resonant transport through a double barrier resonant tunneling structures (DBRTS) was conducted by Sajoto et al. [33] on GaAs/Al$_x$Ga$_{1-x}$As heterostructures buried beneath the Au/GaAs interface. Fig. 42 (left) shows the layer structure and calculated band profile of the DBRTS structure whose design included the δ-doped Be sheet to flatten the band profile at room temperature. A comparison of 77 K BEEM spectra for (a) the GaAs reference sample, (b) the DBRTS and (c) the 100 Å Al$_x$Ga$_{1-x}$As ($x = 42$) single barrier is given in the right panel of Fig. 42. The threshold for the DBRTS is clearly lower than that for the single barrier sample, which has the same barrier height, and the threshold position is in a good agreement with the calculated value of the quasi-bound state energy (~ 1.2 eV). At higher voltages, additional features are observed in the DBRTS spectra, and they were attributed to the opening of additional conduction channels associated with the higher-lying L and X valleys.

The above first study, where the temperature dependence of the BEEM spectra was used to investigate the hot electron transport, led to the further study of the electron-wave interference effect on the ballistic transmittance and device performance. Quantum-interference filters were designed and realized by using GaAs/Al$_{0.2}$Ga$_{0.8}$As as a heterostructure of choice [171]. The designed devices are in essence the GaAs/Al$_{0.2}$Ga$_{0.8}$As double barrier structures with one tunneling resonance (~ 50 meV above the Γ minimum of GaAs) and next above-barrier resonance (~ 200 meV above the Γ minimum of GaAs). The distance between Al$_{0.2}$Ga$_{0.8}$As barriers of 9 ML thickness was 22 ML (11 ML) to produce a constructive (destructive) interference at the above-barrier quasi-bound state. It was shown that the SD-BEEM spectra accurately reproduce the transmittance functions of the designed half- and quarter-wavelength structures at 77 and 300 K
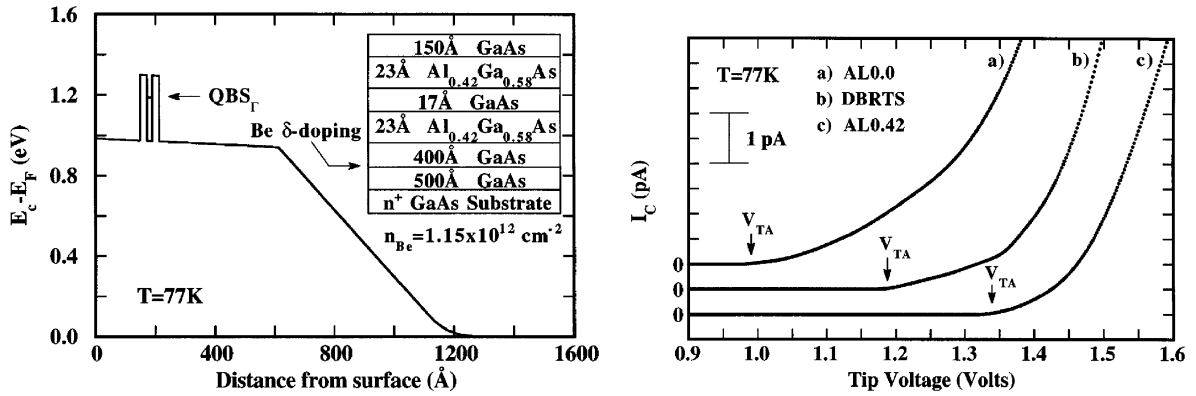
Fig. 42. Left panel shows the layer structure and calculated band profile of the DBRTS structure whose design included the δ-doped Be sheet to flatten the band profile at room temperature. Right panel shows the BEEM spectra at 77 K for (a) the reference GaAs sample, (b) DBRTS, and (c) GaAs/Al$_{0.42}$Ga$_{0.58}$As single barrier sample [33].

(attaining nearly temperature-limited resolution) (see Fig. 43). The tunneling resonance was identified with a first peak (from low-energy side) in the SD-BEEM spectrum for both devices, whereas the above-barrier quasi-bound state position coincided with the higher-energy peak (dip) for constructive (destructive) interference. Recently, the 77 K SD-BEEM spectra of a half-wavelength filter were used to measure fluctuations in the thickness of buried GaAs and Al$_{0.2}$Ga$_{0.8}$As layers [172]. By performing BEEM spectroscopy at several different spatial locations and by utilizing the relation between the thickness of the device and the energy of the quasi-bound states, single-monolayer fluctuations were detected in the thickness of both the GaAs quantum well and the surrounding Al$_{0.2}$Ga$_{0.8}$As barriers.

5.3.2. Superlattices

A miniband in a short period superlattice (SL) covers a rather broad energy range compared to a double barrier resonant tunneling diode and, therefore, electron transport through its states is expected to be more pronounced and better resolved.

Cheng et al. [135] have applied BEEM to study electron transport in InAs/AlSb SLs. The barrier was too low for the SL to allow consistent probing by BEEM spectroscopy. However, the SL BEEM signal was elevated above the background noise after repeated stressing of the metal surface. A BEEM threshold of 0.8 eV was observed for the Au/24 Å-period SL system after the stress treatment.

Smoliner et al. [35,173] have used a buried 10-period 30 Å GaAs/25 Å Al$_{0.4}$Ga$_{0.6}$As SL (with one below-barrier miniband) on Au/GaAs Schottky diodes to study the energetic current distribution in BEEM at $T = 100$ and 300 K (GaAs cap layer is 300 Å). The authors showed that the miniband results in a BEEM current threshold clearly below the height of the Al$_x$Ga$_{1-x}$As barriers, as shown in Fig. 44. In contrast to the Au/GaAs reference sample, where the BEEM current follows the 2 or 5/2 power law, the SL spectrum is almost linear up to a sample bias of 1.3 eV (above this bias, electrons start to overcome the AlGaAs barriers). The theoretical calculations, based on the SK model (with the incorporation of an additional SL transmission coefficient
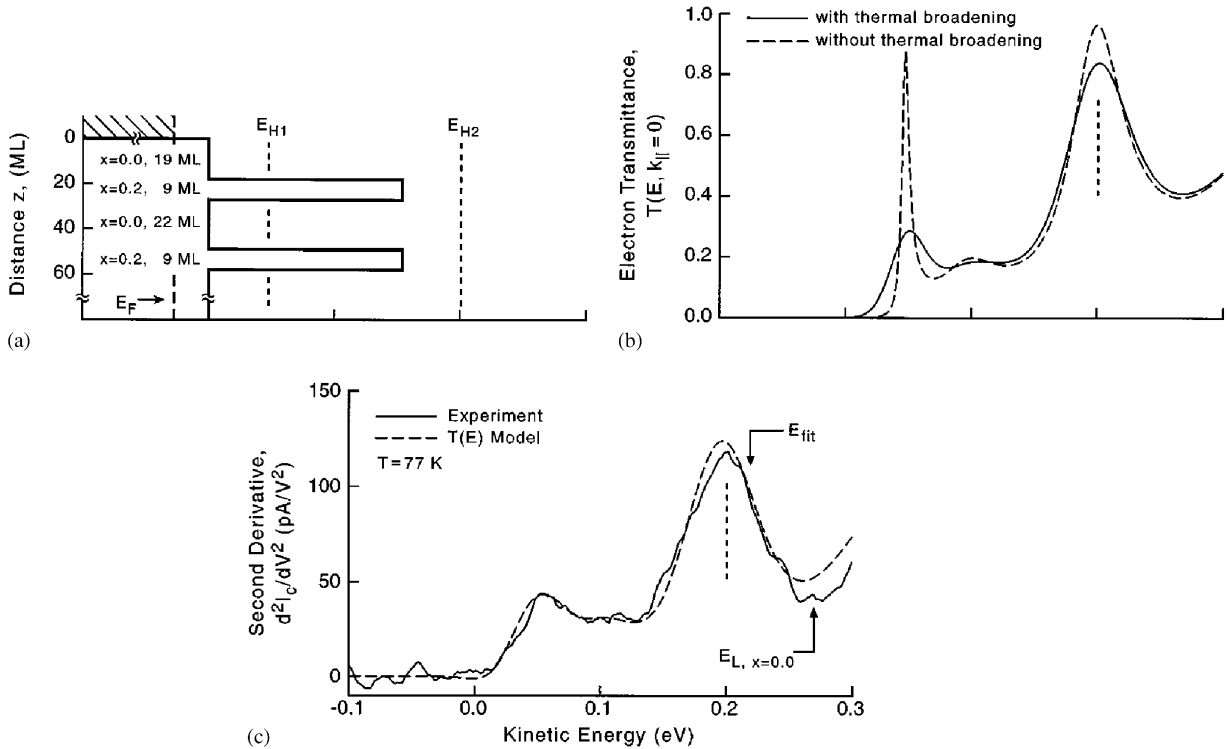
Fig. 43. (a) The band diagram and (b) the corresponding normal-incidence electron transmittance function $t(E, k_{||} = 0)$ with and without thermal broadening for the designed half-electron-wavelength resonant device which has one tunneling resonance E_{H1}, and one above-all-barriers resonance E_{H2}. (c) Second derivatives of the experimental spectrum and of the BEEM $t(E)$ model spectrum for data acquired at $T = 77$ K. The spectrum accurately reproduces the shape of the thermally broadened $t(E, k_{||} = 0)$, which represents the resolution limit of BEEM spectrum [171].

into it) are in a good agreement with the experiment and confirm the linear BEEM spectral shape in the SL energetic range. It was shown that it is an electron refraction at the Au/GaAs interface (taking into account the $k_{||}$ conservation and difference in the electron effective masses) that leads to the almost inversion of the hot electron distribution (in Au, the electron distribution is peaked toward the Fermi energy of the STM tip, but in GaAs the electron distribution is peaked toward the Schottky barrier). Thus, as the tip-to-base voltage increases, an increasing number of electrons are available at the SL energy, and the BEEM current increases continuously, leading to the almost linear dependence on the tip-to-base bias. However, if the resonant structures are located directly below the metal base, the authors observed a step-like behavior of the BEEM spectrum that is explained by direct coupling (tunneling) of ballistic electrons in the Au base to the resonant level underneath [174]. It was also argued that assuming $k_{||}$ conservation, the direct tunneling into the resonant state, when there is no intermediate refraction at the Au/GaAs interface, would provide effective filtering for both $k_{\perp}$ and $k_{||}$. Thus one would expect better spatial resolution of BEEM. However, there are no experimental data confirming this prediction.
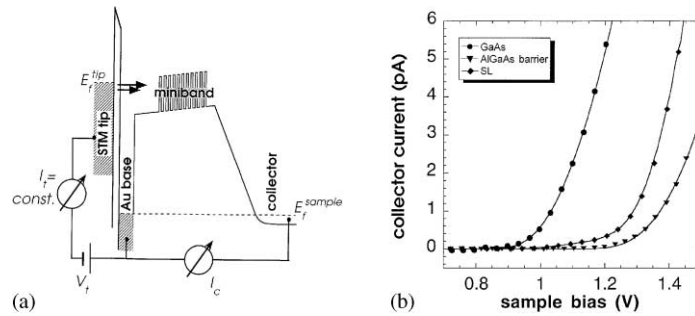
Fig. 44. (a) BEEM setup and conduction band profile with miniband regime of the superlattice sample. For a high enough bias V_t, carriers can be injected into the subsurface semiconductor structure and will be collected at the highly doped collector region. No external bias is applied across the semiconductor. (b) BEEM spectra obtained at room temperature on a sample with a conventional Au/GaAs(3 1 1)A Schottky barrier, a 100 Å thick AlGaAs barrier buried 300 Å below the interface, and on a superlattice sample. Solid curves show thermally broadened power-law fits for the GaAs and the AlGaAs sample, and a weighted fit to the data of the superlattice sample [173].

Heer et al. [34] showed that for biased 10-period 30 Å GaAs/25 Å $Al_{0.4}Ga_{0.6}As$ SL (buried 300 Å below the Au/GaAs interface), both the position of and the transmission of the miniband are a function of the applied base-to-collector bias. In the SD-BEEM spectrum numerically extracted from the original BEEM spectrum, the miniband manifests itself as clear peak. Biasing the SL results in a shift of the miniband peak position in the SD-BEEM spectra, in accord with the transmission calculations based on the SK model. In addition, the BEEM current magnitude is reduced as soon as a base-to-collector bias is applied, and it was explained in terms of the bias-dependent energy width of the miniband. This result is in accord with hot electron spectroscopy results, that in biased superlattice, a significant decrease of the miniband transmission with increasing electric field occurs due to the localization of the electron wave function [175]. As useful application of this experiment, the GaAs/AlGaAs SL can be employed as energy filter to study the energetic distribution of ballistic electrons in BEEM experiments by deconvolution of the transmitted electron current with the calculated miniband transmission as a function of collector bias.

5.4. BEEM imaging to study defects and nanostructures

5.4.1. Study of buried defects and dislocations

One example of the buried dislocation imaging in BEEM experiments was presented in Section 3.3. for the $In_xGa_{1-x}As/GaAs$ interface buried 400–700 Å below the m–s interface. For silicide–silicon systems, in-situ BEEM technique was successfully applied by Fernandez et al. [72,73] ($NiSi_2$/Si at room temperature) and Sirringhaus et al. [78,80–82,176] ($CoSi_2$/Si at 77 K) to investigate the contrast mechanisms by which individual interfacial defects (misfit dislocations and point defects) can be resolved. It was found that in $NiSi_2$/n-Si(111) and $CoSi_2$/n-Si(111) systems, misfit dislocations and point defects buried ~ 25–30 Å beneath the surface locally enhance the scattering probability at the interface, as shown in Fig. 45. The increase of the BEEM current at the dislocation was explained by increased electron scattering at the dislocation core. The scattering broadens the $k_{||}$ momentum distribution, and thus facilitates the electron transmission into the
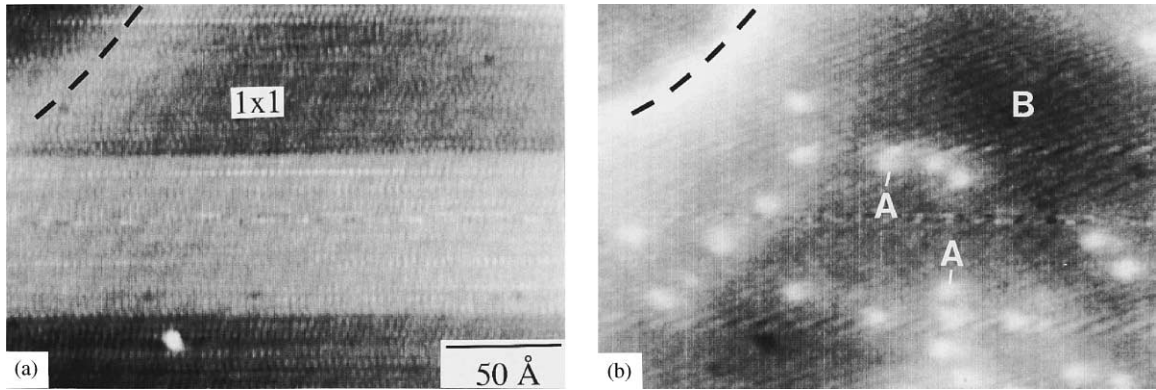
Fig. 45. STM topography (a) and BEEM image (b) of a 32 Å $CoSi_2$/n-Si(1 1 1) film. The corrugation in the STM topography image is not due to the unreconstructed (1×1) atomic surface structure but due to small mechanical vibrations. The BEEM current is enhanced at individual interfacial dislocations (dashed line) and subsurface point defects (A) due to hot carrier scattering. ($V_t = 1.8$ V, $I_t = 10$ nA) [81].

off-axis conduction bands of Si(111). The sharp BEEM dislocation profiles (in favorable cases a spatial resolution below 10 Å has been obtained [77,81]) and observation of the quantum size effect [79] imply that the electron transport in the metal is ballistic, and, therefore, most of the electrons reach the interface with $k_{\parallel} \sim 0$. Increased BEEM current at dislocations indicates that the $k_{\parallel}$ is mostly conserved in dislocation-free regions, although to some extent the probability for scattering exists everywhere at the epitaxial $CoSi_2$/Si interface [81]. Assuming $k_{\parallel}$ conservation, the electron scattering at interfacial defects should increase the BEEM current in the case of $CoSi_2$/n-Si(111) and decrease the BEEM current in the case of $CoSi_2$/p-Si(111) (where holes are transmitted into the zone centered valence band minimum), in accordance with the experiment [77,80]. The same mechanism was invoked to explain the enhancement of the BEEM current observed in the vicinity of structural defects in the $NiSi_2$/Si(111) [72]. Note that no variations of the Schottky barrier have been observed at the silicide/Si(111) interface. In contrast, on $CoSi_2$/Si(100), certain interface dislocations and other defects lower the Schottky barrier by up to 0.1 eV on a nanometer scale [81]. In the future study, the observed Schottky barrier reduction will help to understand the effect of the presence of such defects on the average Schottky barrier height extracted from the transport characteristics of a macroscopic diode.

5.4.2. Study of lateral quantum structures

The laterally patterned quantum wires fabricated on modulation-doped GaAs/AlGaAs hetero-structures were studied by BEEM at $T = 4.2$ and 300 K [37,46,177]. In contrast to bulk samples, the collector electrode consists of a 2D-electron layer at the AlGaAs/GaAs interface. After evaporation of ~ 70 Å Au film, wires were directly observed both in STM and BEEM images, as shown in Fig. 46. At $T = 4.2$ K, no decrease of STM resolution was found in comparison with room temperature measurements. The on-wire BEEM current was characterized by increased magnitude due to the lowering of the Schottky barrier (in contrast to the off-wire case, where the Schottky barrier is defined by $Al_xGa_{1-x}As$ ($x \sim 0.3$), the BEEM onset for the on-wire case is defined by the Au/GaAs Schottky barrier).
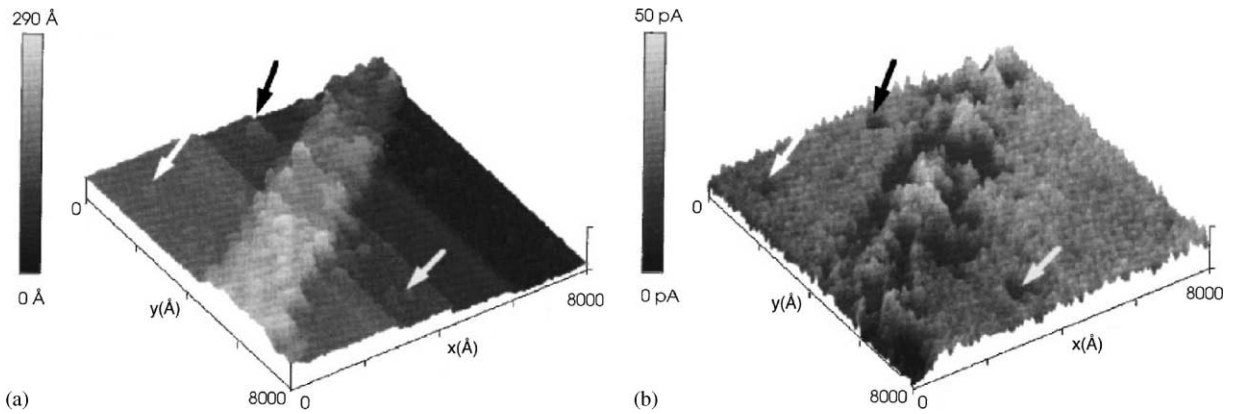
Fig. 46. (a) 3D topographic image of a single quantum wire ($V_t = 1.8$ V, $I_t = 5$ nA). (b) Simultaneously measured BEEM current image. The arrows indicate accumulated Au clusters in the etched region [37].

Westwood et al. [178] had applied BEEM to study GaAs/AlAs buried lateral period SLs (100 Å GaAs cap layer). While the STM image shows the usual grained surface due to the Au clustering during deposition, the BEEM image is dominated by striations aligned with the surface steps. A spectroscopic examination of the potential barrier across the sample surface reveals a bimodal distribution consistent with a modulation of $Al_xGa_{1-x}As$ mole fraction perpendicular with the surface steps.

5.4.3. Study of single quantum dots

5.4.3.1. InAs quantum dots. The first BEEM study of buried single quantum dots (QDs) was conducted on InAs self-assembled QDs buried spatially beneath a Au/GaAs interface [38]. For BEEM experiments, the InAs dots were grown on top of a 300 Å undoped GaAs buffer layer and covered with 50–85 Å GaAs cap layer. Fig. 47 shows a 7500 Å × 7500 Å STM image taken with a 1 nA tunnel current which shows the surface features above several dots covered by a 50 Å GaAs cap layer. The features are ~ 1000 Å in diameter and 30–50 Å high (the dip near the center of each dot was attributed to the strain-induced preferential buildup of the cap GaAs layer away from the center of the dot during the growth process). Gold grains, with diameter ~ 200 Å are also visible. Fig. 48 shows a high-resolution room-temperature STM image of a single InAs QD, capped with a 75 Å GaAs layer. Also shown is the corresponding BEEM image taken with $I_t = 2$ nA and $V_t = 1.5$ V, well above the Schottky barrier height. A strong enhancement of the BEEM current is observed on the QD buried beneath the surface. To estimate quantitatively the BEEM transport across the QDs, the BEEM spectra were taken on and off a single dot (right window in Fig. 48). The measured current spectra exhibit fine structure consistent with resonant tunneling through two 0D states of the dot (with energetic separation of ~ 0.1 eV). The BEEM images and spectra clearly show the power of BEEM to probe energetic states of individual, nanometer scale, semiconductor quantum structures buried beneath the surface.
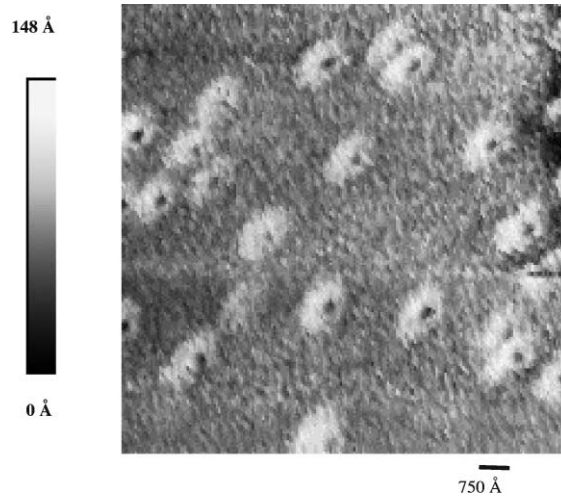
Fig. 47. STM image of surface features in a region where several InAs quantum dots are present and capped with a 50 Å GaAs layer and 85 Å Au layer. The dips near the center of each feature represent the positions of the dots beneath the surface [38].
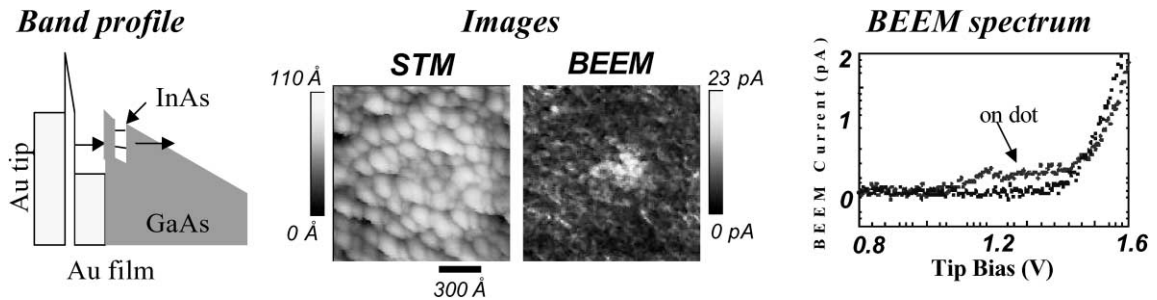

Fig. 48. (from left to right) Schematic of band profile, STM and BEEM images, and characteristic BEEM spectra for InAs/GaAs self-assembled single quantum dots [38].

5.4.3.2. GaSb quantum dots grown on GaAs. GaSb self assembled QDs grown by MBE on GaAs exhibit a staggered (type II) band lineup with a potential barrier in the conduction band [179–181]. Therefore, electron–hole recombination in these structures is spatially indirect, so that optical measurements do not provide adequate information about the conduction band offset between the GaSb dots and GaAs. Along with that, traditional transport methods cannot measure this local band offset because of the small (~ 500 Å) lateral dot size, and any offset measurement would average over areas with and without dots. In BEEM, however, carriers are locally injected into semiconductor structures to spectroscopically probe buried interfaces on a nanometer scale.

Fig. 49 shows STM and BEEM images of a single, GaAs capped, GaSb dot. In the STM image, a roughly circular feature ~ 500 Å in diameter and ~ 50 Å tall, marks the lateral position of the buried dot. The area in the BEEM image aligned with the dot profile in STM is darker than the surrounding region, implying that the BEEM current through the dot is reduced due to electron
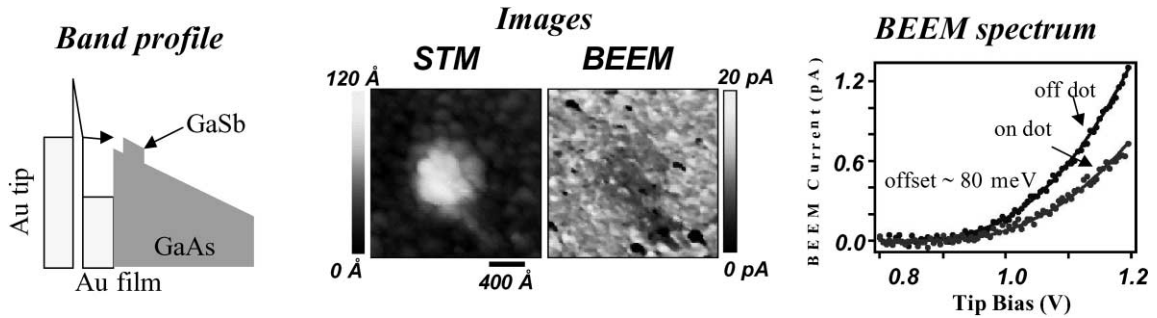
Fig. 49. (from left to right) Schematic of band profile, STM and BEEM images, and characteristic BEEM spectra for GaSb/GaAs self-assembled single quantum dots [39].

reflection off the dot's potential barrier. The height of this barrier, i.e. the local band offset, can be extracted from the changes in BEEM spectra between the on and off cases. The on-dot and off-dot BEEM spectra of several dots were fitted by using a modified Bell-Kaiser planar tunneling model [2,58], giving a local conduction band offset for GaSb dots on GaAs of 0.08 ± 0.02 eV. For details of this study, see Ref. [39].

5.4.3.3. Phosphide-related quantum dots. Phosphide materials are widely used to fabricate light-emitting diodes and injection lasers emitting in the visible spectrum. The BEEM study of the properties of pseudomorphic $Al_{0.3}In_{0.7}P$ QDs grown by low-pressure MOCVD on GaP was recently reported in Ref. [40]. AlInP self-assembled QDs were grown on top of a thick undoped GaP buffer layer (grown on the n^+-GaP substrate) and covered with 50 Å GaP cap layer. Finally, a 60 Å Au film was thermally evaporated to form a good base layer for BEEM measurements. From the STM images, scanned at room temperature with a tunneling current of 4 nA, a characteristic QD was estimated to be approximately 700 Å width and 50 Å of height. In simultaneously taken BEEM images, with the tip bias of 1.5 V, the self-assembled QD-induced contrast was observed, with a reduced BEEM current for the on-dot electron injection. Fig. 50(a) displays the spectroscopic data that are obtained when the STM tip is positioned on and off a single $Al_{0.3}In_{0.7}P$ QD. The solid line represents the theoretical fit to the experimental data using the BK model. When the tip is away from the dot, it essentially measures the barrier height of the Au/GaP interface, which is determined to be 1.27 ± 0.05 eV. However, when the tip is on the dot, the situation is quite different. The ballistically emitted electron will experience two different interfaces, which are Au/GaP and $GaP/Al_{0.3}In_{0.7}P$. Since the threshold for the BEEM current on the dot is approximately measured as 1.4 ± 0.05 eV, a local conduction-band offset between GaP and $Al_{0.3}In_{0.7}P$ can thus be determined to be 0.13 ± 0.1 eV.

Another example is the BEEM study of the self-assembled InP QDs on $Al_{0.5}In_{0.5}P$ (50 Å) grown on a GaAs matrix [182]. The dots are covered with $Al_{0.5}In_{0.5}P$ (50 Å) and finally capped with 50 Å of GaAs. Thus the InP quantum dots are sandwiched in a double barrier heterostructure of $GaAs/Al_{0.5}In_{0.5}P/InP$-QD$/Al_{0.5}In_{0.5}P/GaAs$. The BEEM spectra taken while the tip is away from the dot, as shown in Fig. 50(b), reveal the presence of a single threshold at 1.44 eV corresponding to the charge transport over the $Al_{0.5}In_{0.5}P$ barrier. However, when the tip is positioned on the QD, an additional threshold is observed at 1.12 eV, which is attributed to the

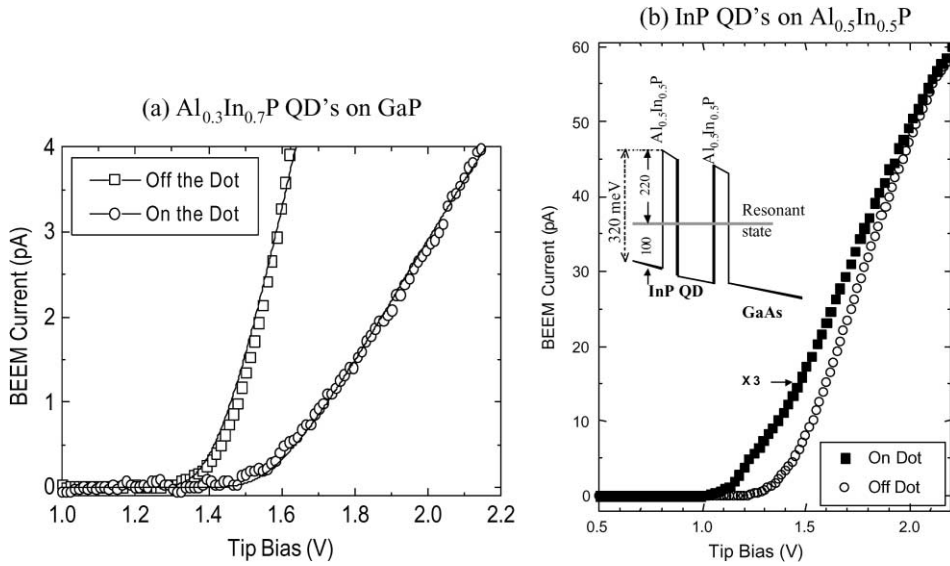Fig. 50. BEEM current spectra taken on and off the QD for the case of (a) $Al_{0.3}In_{0.7}P$ QDs on GaP and (b) InP QDs on $Al_{0.5}In_{0.5}P$ grown on a GaAs matrix. A band diagram is shown in the inset [40,182].

resonant state in the double barrier heterostructure. The relative intensity of the BEEM current magnitudes above the thresholds further suggests that the transmission through the resonant state is significantly higher than over the barrier itself. By taking 0.92 eV as the Schottky barrier on GaAs, the band offset for $GaAs/Al_{0.5}In_{0.5}P/GaAs$ is determined as 1.24 eV. Further, assuming the band offset for $InP\text{-}QD/Al_{0.5}In_{0.5}P$ barrier as 0.34, the relative position of the resonant state is determined as 0.10 ± 0.02 eV with respect to the GaAs conduction band minimum. A band diagram thus constructed is shown as an inset in Fig. 50(b).

5.4.4. BEEM study of magnetic structures

The spin-dependent electron scattering behavior of thin ferromagnetic films and the spin-filtering effects on transport across ferromagnetic/nonferromagnetic metal interfaces are fundamental to the understanding and application of the magnetotransport properties of magnetic multilayered systems. With the ever-shrinking size of magnetic devices and the promise of novel magnetic behavior there is a strong need to study magnetism at smaller and smaller scales, below the resolution limit of standard magnetic imaging techniques available today.

Following the initial study of a magnetic multilayer by BEEM spectroscopy [183], a variation of BEEM has been developed to image the magnetic structure in thin-film multilayers with nanometer resolution [97,184]. In the nominally uncoupled Co/Cu/Co (25 Å/45 Å/12 Å) trilayer system magnetic domains are found to occur on a ~ 0.5 μm-length scale and less. The Co/Cu/Co trilayer, a ferromagnetic-normal-metal-ferromagnetic system that is the basic component of spin-valve and GMR devices, was grown on Si(111) substrate precoated with a thin Cu/Au bilayer to form a high-quality Au/Si Schottky barrier interface, and a Cu seed layer for the Co growth.

When the unpolarized current from the STM is incident upon the top ferromagnetic layer, the spin-dependent scattering results in strong attenuation of one of the spin components. When
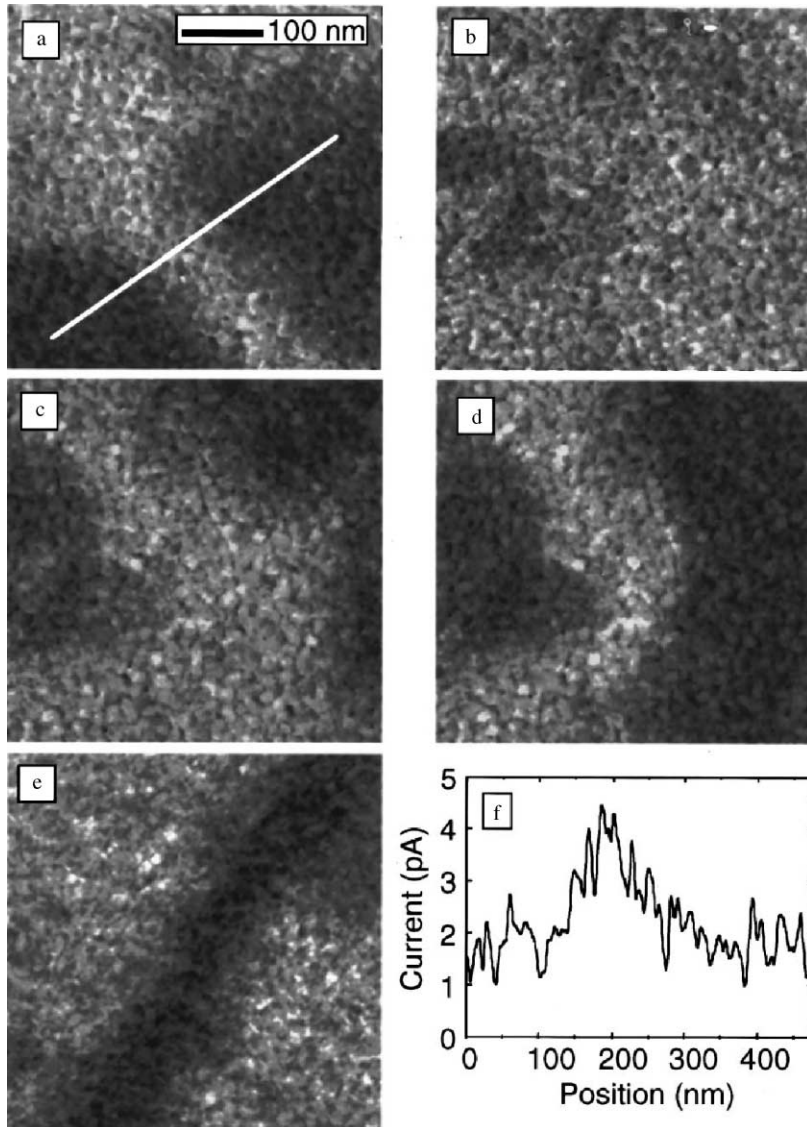
Fig. 51. (a)–(e) BEEM images (500×500 nm^2) taken at a fixed position in a varying magnetic field applied parallel to the film plane, (a) before the applied field, and in applied fields of (b) -40 Oe, (c) 10 Oe, (d) 20 Oe, and (e) 40 Oe. The linear gray-scale range for each is from 1.0 pA (black) to 5.0 pA (white). $V_t = 1.5$ V and $I_t = 2$ nA. (f) is a cross-sectional view of the position indicated in (a) [184].

the magnetization directions of the two layers are aligned, only one of the spin components will be heavily scattered in passing through them, yielding a comparatively high BEEM current. In the case of misalignment between ferromagnetic layers, both components will be strongly attenuated. This process is very analogous to "polarizer-analyzer" experiments in optics. It was found that by applying magnetic field ~ 40 Oe, the BEEM contrast disappears indicating a saturated state of magnetic alignment, when the parallel alignment of two layers occurs [97,184], as shown in Fig. 51.

It was shown also that complete antialignment is never obtained over large, > 1 μm, areas for any values of magnetic field, indicating some residual coupling between the Co layers.

By hot electron (1–2 eV) BEEM spectroscopy taken as a function of Co layer thickness and relative magnetic alignment, the spin-dependent attenuation length of thin Co films and the energy dependence of the relative transmission factors for tunneling-injected electrons with different spin orientation were estimated [97]. The electron attenuation length in Co was estimated to be ~ 8 Å for electrons with spin orientation opposite to the Co layer magnetization, and ~ 21 Å for their parallel orientation, that are much smaller than the hot electron attenuation lengths found in free electron metals [86].

The filtering effect of the Co/Cu interface was demonstrated by studying the Co/Cu/Co trilayers by BEEM [97]. The strong reduction of the BEEM current when ~ 2–3 Å of Co is evaporated on top of Cu/Au/Si system was attributed to the band structure mismatch at the Co/Cu interface [Cu(111) has no propagating momentum states in a much larger cone around the film normal than Co(111)].

6. Metal–insulator–semiconductor systems

Study of electron transport in insulators (e.g. oxides) is very demanding for MIS (MOS) device performance and reliability. In the presence of an additional insulator layer between the metal and semiconductor, the distribution of electrons entering the semiconductor is modified by the insulator band structure as well as by electron–phonon scattering in the insulator layer. The electronic charge trapping and breakdown characteristics, which are determined by defects and impurities in the bulk insulator or at its interfaces, become increasingly sensitive to local fluctuations in material properties as device dimensions are reduced. The standard techniques (such as Fowler–Nordheim tunneling injection and internal photoemission [185–187]) to characterize the degradation mechanisms are still macroscopic (0.01–1 mm^2) and require high fields across the oxide to energize the injected electrons.

So far two insulators, SiO_2 and CaF_2, were extensively studied in BEEM experiments. SiO_2 is a material of natural choice for today's Si-based MOS devices. It is a chemically stable dielectric, it has excellent passivating and dielectric properties and its quality can be consistently controlled during production [188]. The performance and reliability of modern MOS devices is ultimately dependent on the electronic properties of SiO_2. Although both intrinsic and extrinsic electronic properties of SiO_2 have been the subject of extensive studies by using macroscopic techniques [185], the ongoing minimization of electronic devices requires the atomic-scale control and characterization of the material properties. CaF_2, in its turn, is an excellent choice for an epitaxial insulating layer in silicon-based MIS structures due to its large bandgap (12.1 eV) and its small lattice mismatch with Si (0.6%) allowing a growth of ultrathin flat CaF_2 layers as the insulating film in MIS devices. Si segregation to the surface, as observed in case of Au/Si interface, is strongly reduced by the CaF_2 intralayer [25]. Epitaxial CaF_2 films on Si(111), grown at elevated temperatures under UHV conditions, are considered to be promising candidates for replacement of SiO_2 in MOS technology. Because of the layer-to-layer growth of CaF_2, the more homogeneous insulator film can be grown with less density of interface states at the epitaxial CaF_2/Si(111) interface [189].

Cuberes et al. [25] first used the BEEM technique as a new, microscopic method to study electronic properties of very thin CaF_2 insulating films, and later BEEM was applied to study SiO_2 properties in MOS devices [26,64]. In this section we will review the main BEEM results for metal/SiO_2/Si and metal/CaF_2/Si systems.

6.1. Insulator conduction band effect

6.1.1. Metal/SiO_2/Si MOS system

Ludeke et al. [26,190] observed a BEEM current threshold near $V_t = 3.9$ V in 32 Å Pt/(27-62 Å) SiO_2/Si(100) structure, and it was interpreted in terms of current transport through the SiO_2 conduction band. The same threshold position was observed later by Kaczer et al. [191] in 40 Å Pt/27 Å SiO_2/Si(100) system. In the BEEM imaging mode, the first detection of high transmission regions in thin oxide was presented [190]. These were characterized by relatively small 1–2 nm patches that exhibited much lower thresholds (~ 1.1 V) than those observed for normal oxides (~ 4 V). It was explained in terms of defect-related or direct tunneling through the oxide bandgap.

In the case of thin SiO_2 (30 Å), the very well-defined thresholds (with essentially zero BEEM current below the threshold) were observed for Au/SiO_2/n-Si(100) (4 eV) and Ir/SiO_2/n-Si(100) (5.6 eV) [192], as shown in Fig. 52. In the case of ultrathin SiO_2 (10 Å), a different behavior was observed. For Ir/SiO_2/Si, a much lower threshold was observed at 1.5 eV. Since this threshold is different from the Schottky barrier at the Ir/Si interface (0.9 eV) and the signal is strong, it was explained not by direct tunneling through the barrier, but through a possible resonant state in the SiO_2 layer.

The oxide contribution to the BEEM transport was obtained by subtraction of the BEEM spectrum with zero SiO_2 thickness from the spectrum with finite SiO_2 thickness, after its correction for the electron impact ionization in Si (see Fig. 53). The authors studied the derived-from-experiment transmission probabilities across the SiO_2 layer as a function of tip-to-base bias and bias applied across the oxide. It was found that the SiO_2 transmission probability depends on the electron energy, and it was explained in terms of electron–phonon scattering in SiO_2. A good agreement with complementary Monte Carlo simulations that included details of the SiO_2 band structure and energy-dependent electron–phonon scattering effect was obtained [190].

In 30 Å Pd/75 Å SiO_2/Si(100), BEEM was applied to estimate the dielectric constant in SiO_2 layer by studying the barrier lowering (due to the image force effects) as a function of applied oxide bias [193].

6.1.2. Metal/CaF_2/Si MIS system

Cuberes et al. [194] have performed BEEM experiments in Au/14 Å CaF_2/Si(100) structure under UHV conditions. The authors observed a BEEM current onset at $V_t = 3.3$ V, and it was interpreted in terms of current transport through the CaF_2 conduction band. No irreversible loss of ballistic transmittance was observed (up to $V_t \sim 8$ V). Also the authors found a strong effect of the DOS of the CaF_2 film on the BEEM spectral shape, in reasonable accord with the theoretical predictions [195].

LaBella et al. [196,197] have characterized the hot electron transport properties of ultrathin Pt/CaF_2/Si(111) system by in-situ BEEM and STM. The 2–10 ML CaF_2 was grown epitaxially on Si(111) at 770°C, that gives many atomically flat, relatively defect-free terraces and steps. The Pt
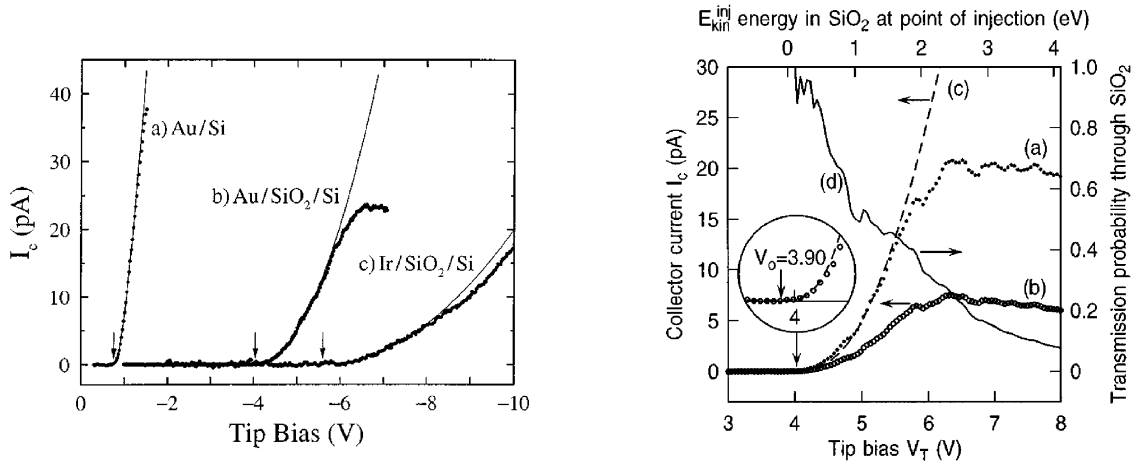
Fig. 52. (a) BEEM spectrum measured on a Au/Si sample without an oxide barrier, with $d_{Au} = 50$ Å and $I_t = 1$ nA. The solid line is a fit to the Bell and Kaiser model giving $eV_s = 0.76$ eV. (b) and (c) BEEM spectra measured on samples with a thin oxide barrier ($d_{ox} \approx 30$ Å). The solid lines are fits to a quadratic law $I_c \propto (V - V_s)^2$. (b) Case of a Au base with $d_{Au} = 100$ Å and $I_t = 10$ nA, giving $eV_s = 4.0$ eV. (c) Case of an Ir base with $d_{Ir} = 100$ Å and $I_t = 10$ nA, giving $eV_s = 5.6$ eV. The arrows indicate the threshold position [192].

Fig. 53. BEEM spectra of a 62 Å SiO_2 layer biased at $V_{ox} = 2$ V before [curve (a)] and after [curve (b)] the removal of contributions from impact ionization in the Si. Curve (c) is a model fit to the threshold region of (b) for an oxide transmission probability $T_{ox} = 1$. Curve (d), the ratio of (b)/(c), represents T_{ox} determined from the data. The inset depicts the fitted curve in the threshold region magnified $2\times$ along the abscissa and $20\times$ along the ordinate [190].

morphology consists of nodules, which nucleate at step edges and at defects ascribed to F vacancies on the CaF_2 surface. Changes in the tip bias provide a significant change in the imaged topography. The STM images at biases well above 3.3 eV (conduction band minimum of CaF_2) show similar features to bare CaF_2/Si(111), while images at the CBM show features of the deposited Pt. These topography results correlate well with the BEEM spectroscopy. Indeed, the BEEM spectra of 10 Å Pt/5 Å CaF_2/Si(111) show a peak at ~4.5 eV (the increase starts at ~3–3.5 eV) due to the DOS of the CaF_2 intralayer and an additional peak at 2 eV, indicating transmission through defects at the Pt/CaF_2 interface.

Recently, Sumya et al. [198,199] conducted BEEM studies of the electron transport phenomena across Au/CaF_2/n-Si(111) heterostructures as a function of the CaF_2 growth temperature (20°C, 550°C and 700°C). It was shown that the Au growth and electron transport properties depend strongly on the 2 ML CaF_2 growth temperature. The threshold voltage for an insulating CaF_2 intralayer, which is about 3.3–3.6 eV, is obtained only in the sample in which CaF_2 was deposited at 700°C, whereas for lower CaF_2 growth temperatures, the BEEM onset starts at ~1 and ~0.7 eV for 20°C and 550°C, respectively, as shown in Fig. 54. The complementary Fourier-transform infrared spectroscopy shows the presence of Ca–Si–F bonds for the 550°C deposition, and this implies that the CaF_2 heteroepitaxial growth at 550°C is unsuccessful in obtaining a high-quality CaF_2 layer. The nonepitaxial growth of CaF_2 at low temperatures creates defect states in the CaF_2 layer and/or at the interface below the CaF_2 conduction band that facilitate electron transport and lower the BEEM threshold.
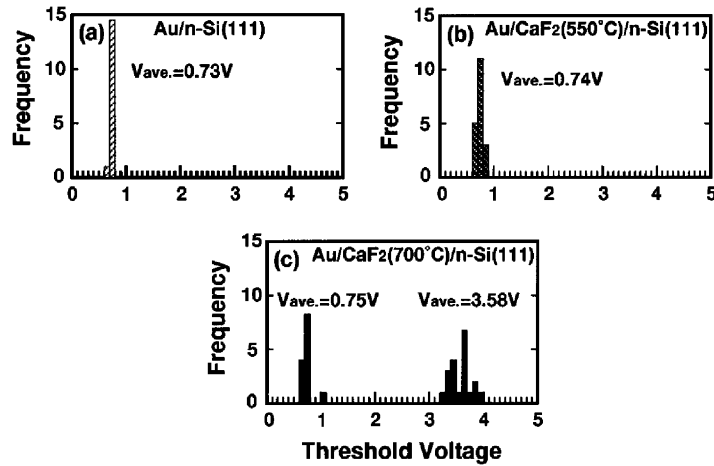
Fig. 54. Distributions of measured threshold voltages of (a) 25 ML Au/Si(1 1 1), (b) 50 ML Au/2 ML CaF$_2$ (550°C)/Si(111), and (c) 50 ML Au/2ML CaF$_2$ (700°C)/n-Si(1 1 1) [199].

6.2. Charge trapping (build-up) and MOS device degradation

A large portion of present reliability issues in MOS-based technology is related to the presence of hot electrons in the gate SiO$_2$ layers. Problems range from undesired buildup of trapping charge in the oxide film to degradation and breakdown of the dielectric.

BEEM was used to locally inject electrons into thick $\sim$250 Å SiO$_2$ film built into a MOS structure [27,200]. Some of these electrons are trapped in the bulk of the oxide and cause an increase in the local barrier height and local time-dependent suppression of the BEEM current, consistent with a build-up of trapped BEEM electrons in the oxide. By studying the lateral extent of the current suppression caused by injection of charge at one point, the authors concluded that generation of traps created in the oxide by hot BEEM electrons is a likely dominant trapping mechanism. Measured variations in the BEEM threshold voltage with the voltage applied across the SiO$_2$ film can be used to estimate the local trapped charge density and the approximate depth of the trapped charge in the oxide.

The high current densities ($\sim 10^3$ C/cm^2 s) and choice of energy make BEEM an attractive method to study breakdown phenomena in dielectrics. By local stressing of thin SiO$_2$ layers ($\sim$25–40 Å) by injecting hot electrons into the conduction band of SiO$_2$, it is possible to inject very high charge densities of very hot electrons into the oxide film without damaging the MOS structure, as was found in Pd/SiO$_2$/Si(100) [201] and Pt/SiO$_2$/Si(100) [191]. A successful breakdown sequence for a 38 Å oxide stressed with 6 eV (kinetic energy) electrons is shown in Fig. 55. It was found that the total charge injected at breakdown exceeds by several orders of magnitude the values obtained by conventional Fowler–Nordheim tunnel injection under high field conditions. It was concluded that the observed breakdowns are still controlled by impurities/defects. Similar effect of the BEEM current build-up was also observed by Wen et al. [202] under even modest exposures (several single scans up to $V_t = 7$ V at $I_t = 2$ nA) in Pd/28 Å SiO$_2$/Si(100). This is in contrast to the suppression of the BEEM current observed on thicker SiO$_2$ films ($d > 40$ Å) due to

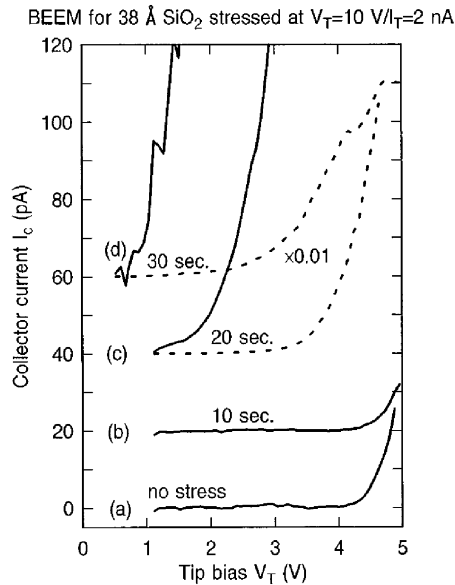BEEM for 38 Å SiO$_2$ stressed at V$_T$=10 V/I$_T$=2 nA

Fig. 55. A successful breakdown sequence for a 3.8 nm oxide stressed with 6 eV (kinetic energy) electrons. The shift to higher V_s between curve (a) and (b) is due to negative charge at the SiO$_2$–Si interface. Total injected charge to breakdown (defined by reaching $V_s \sim 1$ V, as in curve (c) is $\sim 6 \times 10^{13}$ C/cm^2 [201].

the buildup of negative charge in the oxide [27,200,203]. One possible explanation for this enhancement is related to an electron-leakage-induced buildup of positive charge at the SiO$_2$/Si interface accompanied by a decrease of the barrier in the oxide due to image force lowering effects. However, the experimental results are inconclusive because of relatively large noise in the BEEM current.

Degradation processes initiated by defect generation in device-grade SiO$_2$ were studied by locally injecting hot electrons from a STM tip into Pd/SiO$_2$/Si(100) MOS structure [204]. By analyzing the obtained BEEM results within the framework of a sheet charge model, charge densities in the oxide film were estimated. For the sample with 71 Å SiO$_2$ thickness, it was found that the SiO$_2$ film contains $\sim (0.7$–$2.8) \times 10^{13}$ cm^2 density of electron traps that are distributed within a 30 Å region adjacent to the Pd/SiO$_2$ interface. By additional stressing at high tip voltages up to 10 V, new traps characterized by a charge density of $\sim (1.9$–$3.6) \times 10^{13}$ cm^2 were created within a 40 Å region near the SiO$_2$/Si interface when the kinetic energy of the electron injected into the SiO$_2$ conduction band exceeds 1.9 eV. This energy is close to a minimum threshold of ~ 2 eV in order to break H–Si bonds. This result suggests that the initial defect generation, which eventually leads to a destructive breakdown of the oxide, is associated with the trap creation by releasing hydrogen at the anode.

6.3. Quantum-size effect

Kaczer et al. [191] have attempted to determine the SiO$_2$ layer thickness from the BEEM spectra. In the case of the BEEM transport above the SiO$_2$ CBM, the BEEM current is only a weak
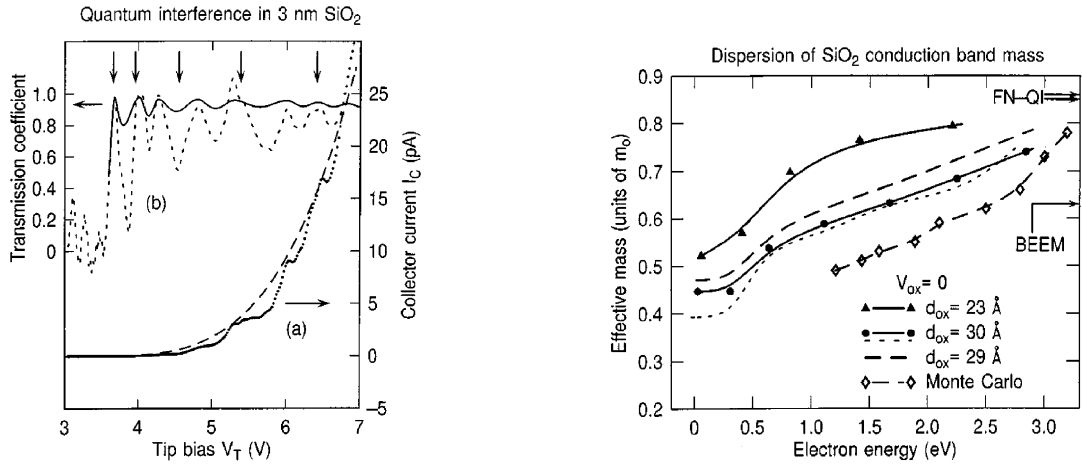
Fig. 56. (a) BEEM spectrum I_c V_t for 1.8 nm W/3.0 nm SiO_2/p-Si(1 0 0) MOS structure (dotted curve), with I_c^0 shown by a dashed line. (b) Experimental transmission coefficient, $t(E) = I_c/I_c^0$ (dotted curve), compared to $t(E)$ calculated with a dispersive mass (solid curve). Vertical arrows mark QI maxima for $t(E)$ calculated with a fixed mass $m_{ox} = 0.42$ m_0. The threshold is at 3.77 V [205].

Fig. 57. Conduction band mass dispersions $m_{ox}(E)$ for SiO_2 determined from quantum interference oscillations in BEEM spectra (top four curves), compared to dispersion derived from Monte Carlo simulations of experimentally determined electron mean free paths (lowest dash-dotted curve) [205].

function of the film thickness. In the case of ultrathin SiO_2 (< 30 Å) when the tip voltage is below the SiO_2 CBM, a thickness-sensitive direct tunneling through the oxide will become considerable. However, in the BEEM experiment with 27 Å SiO_2, the BEEM current signal was too small to produce a measurable signal in this regime. It was discussed that the alternative method for estimating local thickness variations of the ultrathin SiO_2 layer is based on measurement of possible quantum-mechanical resonances of BEEM electrons in the conduction band of the SiO_2 film. The authors demonstrated that with some experimental care the oscillations could actually be observable in the first-voltage-derivative BEEM spectra (extracted numerically from the original BEEM spectra), in reasonable agreement with the theoretical expectations for hot electron resonance.

In 50 Å Pd/28 Å SiO_2/Si(100) system, quantum-interference oscillations of electrons (these oscillations arise from the constructive/deconstructive interference of electron waves reflected at the Pd/SiO_2 and SiO_2/Si interfaces of the SiO_2 cavity) in a thin SiO_2 layer were observed by BEEM using $I_t = 2$ nA [28,202]. Oscillations with up to four peaks in the energy region of 0–3 eV above the injection threshold were observed. The magnitude of the oscillations is $\sim 30\%$ of the underlying BEEM current. It was noted that the observation of pronounced oscillations due to the quantum-interference effects in SiO_2 is somewhat surprising because the SiO_2 film is quite leaky, with allowed states in both cladding regions (metal and Si) and extensive electron–phonon scattering losses in SiO_2 (electron mfp in SiO_2 at $T = 300$ K is ~ 10–20 Å).

Quantum interference oscillations in BEEM spectra were also observed for MOS structures with 23 and 30 Å SiO_2 interlayers [205,206]. The authors present an approach based on quantum interference effects of electrons injected directly into the conduction band of SiO_2 from which it is

possible to derive the energy dispersion of the electron effective mass m_{ox}. On the virgin surface, very well-pronounced oscillations (steps) in the BEEM current were observed during the first scan. However, with next scans at the same location, it was observed that the BEEM current increases and smoothens due to the stress-induced positive charging of the SiO_2 film at high voltages. For over-the-barrier transmission, maxima in the transmission probability for a rectangular barrier occur at the following energies $E = (n\pi\hbar/d_{ox})^2/2m_{ox}$ with $n = 1,2,3,\dots$, from which m_{ox} can be deduced by matching theoretical maxima to those obtained experimentally (after correction on the SiO_2 band bending and image potential effects) (see Fig. 56). Using this approach, the 23 and 30 Å oxides exhibit initial (zero kinetic energy) m_{ox} values of $0.52m_0$ and $0.45m_0$, respectively, that disperse upwards by $\sim 0.3m_0$ over a 0–2.5 eV range in kinetic energies, as shown in Fig. 57.

7. Conclusion

In this article, we reviewed briefly recent progress in BEEM experiment and theory for the study of metal/semiconductor and metal/insulator/semiconductor devices. Excellent spatial resolution and independent control of the hot electron energy over a wide range make this technique a powerful tool for nanometer-scale characterization of the spatial and electronic properties of semiconductor (insulator) structures. In BEEM experiments, the hot electron transport is affected drastically by the integrated electron propagation and scattering in the metal layer, at the m–s interface and in the semiconductor itself. As a consequence, BEEM can be characterized by its spatial, energetic and depth resolutions.

Although the BEEM technique was originally invented as a unique microscopic and spectroscopic method to probe the Schottky barriers on a local scale, it has been successfully used for imaging and spectroscopy of buried quantum objects as well as for nondestructive local characterization of buried semiconductor heterostructures. Since BEEM spectra exhibit thresholds at energies where semiconductor states become available for transport, the SD-BEEM spectroscopy is very effective in identifying these thresholds and correlating them to semiconductor band structure. Significant progress was accomplished in establishing BEEM as an effective method for measuring semiconductor heterojunction offsets and for measuring resonant transport through double barrier and superlattice resonant tunneling heterostructures. Based on recent research, we demonstrated BEEM capability for imaging and electron spectroscopy of buried nanosized structures such as single self-assembled quantum dots as well as interfacial dislocations buried below the surface, by exploiting the lateral resolution of BEEM.

References

[1] L.D. Bell, W.J. Kaiser, Phys. Rev. Lett. 61 (1988) 2368 ∗∗∗.
[2] M. Prietsch, Phys. Rep. 253 (1995) 163 ∗∗∗.
[3] L.D. Bell, W.J. Kaiser, Annu. Rev. Mater. Sci. 26 (1996) 189 ∗∗.
[4] Fernandez, H.D. Hallen, T. Huang, R.A. Buhrman, J. Silcox, Appl. Phys. Lett. 57 (1990) 2826 ∗∗.
[5] M. Kozhevnikov, V. Narayanamurti, C. Zheng, Y.-J. Chiu, D.L. Smith, Phys. Rev. Lett. 82 (1999) 3677 ∗∗.
[6] P. Niedermann, L. Quattropani, K. Solt, A.D. Kent, O. Fischer, J. Vac. Sci. Technol. B 10 (1992) 580.
[7] Bauer, M.T. Cuberes, M. Prietsch, G. Kaindl, Phys. Rev. Lett. 71 (1993) 149.
[8] H. Sirringhaus, E.Y. Lee, H. von Kanel, Surf. Sci. 331–333 (1995) 1277.
[9] K. Reuter, F.J. Garcia-Vidal, P.L. de Andres, F. Flores, K. Heinz, Phys. Rev. Lett. 81 (1998) 4963 ∗.
[10] R.H. Williams, Appl. Surf. Sci. 70–71 (1993) 386.
[11] L.D. Bell, S.J. Manion, M.H. Hecht, W.J. Kaiser, R.W. Fathauer, A.M. Milliken, Phys. Rev. B 48 (1993) 5712.
[12] L.D. Bell, A.M. Milliken, S.J. Manion, W.J. Kaiser, R.W. Fathauer, W.T. Pike, Phys. Rev. B 50 (1994) 8021.
[13] R. Ludeke, Phys. Rev. Lett. 70 (1993) 214.
[14] Chahboun, R. Coratger, F. Ajustron, J. Beauvillain, I.M. Dharmadasa, A.P. Samantilleke, J. Appl. Phys. 87 (2000) 2422.
[15] J.J. O'Shea, C.M. Reaves, S.P. DenBaars, M.A. Chin, V. Narayanamurti, Appl. Phys. Lett. 69 (1996) 3022.
[16] M. Kozhevnikov, V. Narayanamurti, A. Mascarenhas, Y. Zhang, J.M. Olson, D.L. Smith, Appl. Phys. Lett. 75 (1999) 1128.
[17] L.D. Bell, R.P. Smith, B.T. McDermott, E.R. Gertner, R. Pittman, R.L. Pierson, G.L. Sullivan, J. Vac. Sci. Technol. B 16 (1998) 2286.
[18] E. Brazel, M.A. Chin, V. Narayanamurti, Appl. Phys. Lett. 74 (1999) 2367.
[19] L.D. Bell, R.P. Smith, B.T. McDermott, E.R. Gertner, R. Pittman, R.L. Pierson, G.J. Sullivan, Appl. Phys. Lett. 76 (2000) 1725.
[20] M. Kozhevnikov, V. Narayanamurti, C.V. Reddy, H.P. Xin, C.W. Tu, A. Mascarenhas, Y. Zhang, Phys. Rev. B 61 (2000) R7861.
[21] H.-J. Im, B. Kaczer, J.P. Pelz, W.J. Choyke, Appl. Phys. Lett. 72 (1998) 839.
[22] B. Kaczer, H.-J. Im, J.P. Pelz, J. Chen, W.J. Choyke, Phys. Rev. B 57 (1998) 4027.
[23] W.J. Kaiser, L.D. Bell, Phys. Rev. Lett. 60 (1988) 1406.
[24] For review, see, e.g., V. Narayanamurti, Sci. Rep. Res. Inst. Tokohu Univ. A, Phys. Chem. Metall. 44 (1997) 165.
[25] M.T. Cuberes, A. Bauer, H.J. Wen, M. Prietsch, G. Kaindl, J. Vac. Sci. Technol. B 12 (1994) 2646.
[26] R. Ludeke, A. Bauer, E. Cartier, Appl. Phys. Lett. 66 (1995) 730.
[27] B. Kaczer, J.P. Pelz, J. Vac. Sci. Technol. B 14 (1996) 2864.
[28] R. Ludeke, H.J. Wen, A. Schenk, Appl. Phys. Lett. 73 (1998) 1221.
[29] J.J. O'Shea, E.G. Brazel, M.E. Rubin, S. Bhargava, M.A. Chin, V. Narayanamurti, Phys. Rev. B 56 (1997) 2026 ∗∗.
[30] S. Bhargava, C. Zheng, J. Ko, M.A. Chin, L.A. Coldren, V. Narayanamurti, Appl. Phys. Lett. 73 (1998) 3271.
[31] S. Bhargava, H.-R. Blank, E. Hall, M.A. Chin, H. Kroemer, V. Narayanamurti, Appl. Phys. Lett. 74 (1999) 1135.
[32] D.K. Guthrie, P.N. First, T.K. Gaylord, E.N. Glytsis, R.E. Leibenguth, Appl. Phys. Lett. 71 (1997) 2292.
[33] T. Sajoto, J.J. O'Shea, S. Bhargava, D. Leonard, M.A. Chin, V. Narayanamurti, Phys. Rev. Lett. 74 (1995) 3427 ∗∗.
[34] R. Heer, J. Smoliner, G. Strasser, E. Gornik, Appl. Phys. Lett. 73 (1998) 3138.
[35] J. Smoliner, R. Heer, C. Eder, G. Strasser, Phys. Rev. B 58 (1998) R7516.
[36] J. Smoliner, C. Eder, G. Böhm, G. Weimann, Appl. Phys. Lett. 69 (1996) 52.
[37] C. Eder, J. Smoliner, G. Strasser, Appl. Phys. Lett. 68 (1996) 2876.

[38] M.E. Rubin, G. Medeiros-Ribeiro, J.J. O'Shea, M.A. Chin, E.Y. Lee, P.M. Petroff, V. Narayanamurti, Phys. Rev. Lett. 77 (1996) 5268 **.
[39] M.E. Rubin, H.R. Blank, M.A. Chin, H. Kroemer, V. Narayanamurti, Appl. Phys. Lett. 70 (1997) 1590.
[40] C.V. Reddy, V. Narayanamurti, J.H. Ryou, U. Chowdhury, R.D. Dupuis, Appl. Phys. Lett. 76 (2000) 1437.
[41] H. Sirringhaus, E.Y. Lee, U. Kafader, H. von Kanel, J. Vac. Sci. Technol. B 13 (1995) 1848.
[42] E.Y. Lee, S. Bhargava, K. Pond, K. Luo, M.A. Chin, V. Narayanamurti, Appl. Phys. Lett. 69 (1996) 940.
[43] E.Y. Lee, S. Bhargava, M.A. Chin, V. Narayanamurti, J. Vac. Sci. Technol. A 15 (1997) 1351 **.
[44] A. Bauer, R. Ludeke, J. Vac. Sci. Technol. B 12 (1994) 2667.
[45] G.N. Henderson, P.N. First, T.K. Gaylord, E.N. Glytsis, B.J. Rice, P.L. Dantzscher, D.K. Guthrie, L.E. Harrell, J.S. Cave, Rev. Sci. Instr. 66 (1995) 91.
[46] C. Eder, J. Smoliner, G. Strasser, E. Gornik, Appl. Phys. Lett. 69 (1996) 1725.
[47] J.G. Simmons, J. Appl. Phys. 34 (1963) 1793.
[48] R. Ludeke, M. Prietsch, J. Vac. Sci. Technol. A 9 (1991) 885 **.
[49] Mao-long Ke, D.I. Westwood, C.C. Matthai, B.E. Richardson, R.H. Williams, Phys. Rev. B 53 (1996) 4845.
[50] G.N. Henderson, P.N. First, T.K. Gaylord, E.N. Glytsis, Phys. Rev. Lett. 71 (1993) 2999.
[51] M.T. Cuberes, A. Bauer, H.J. Wen, D. Vandre, M. Prietsch, G. Kaindl, J. Vac. Sci. Technol. B 12 (1994) 2422.
[52] E.Y. Lee, L.J. Schowalter, J. Appl. Phys. 66 (1989) 4903.
[53] R. Menegozzi, P.-G. Reinhard, M. Schulz, Appl. Phys. A 66 (1998) S897 **.
[54] R. Menegozzi, P.-G. Reinhard, M. Schulz, Surf. Sci. 411 (1998) L810.
[55] C.A. Ventrice, V.P. LaBella, G. Ramaswamy, H.-P. Yu, L.J. Schowalter, Phys. Rev. B 53 (1996) 3952.
[56] L.J. Schowalter, E.Y. Lee, Phys. Rev. B 43 (1991) 9308.
[57] C. Manke, Y. Bodschwinna, M. Schulz, Appl. Surf. Sci. 117/118 (1997) 321.
[58] D.L. Smith, S.M. Kogan, Phys. Rev. B 54 (1996) 10354 ***.
[59] D.L. Smith, M. Kozhevnikov, E.Y. Lee, V. Narayanamurti, Phys. Rev. B 61 2000 13914 **.
[60] M.H. Hecht, L.D. Bell, W.J. Kaiser, L.C. Davis, Phys. Rev. B 42 (1990) 7663.
[61] L.D. Bell, W.J. Kaiser, M.H. Hecht, L.C. Davis, in: J.A. Stroscio, W.J. Kaiser (Eds.), Methods of Experimental Physics 27: Scanning Tunneling Microscopy, Academic Press, New York, 1993.
[62] E.Y. Lee, L.J. Schowalter, Phys. Rev. B 45 (1992) 6325.
[63] E.Y. Lee, H. Sirringhaus, U. Kafader, H. von Kanel, Phys. Rev. B 52 (1995) 1816.
[64] R. Ludeke, A. Bauer, J. Vac. Sci. Technol. A 13 (1995) 614 ***.
[65] E. Cartier, M.V. Fischetti, E.A. Eklund, F.R. MsFeely, Appl. Phys. Lett. 62 (1993) 3339.
[66] R.C. Alig, S. Bloom, C.W. Struck, Phys. Rev. B 22 (1980) 5565.
[67] E.Y. Lee, L.J. Schowalter, J. Appl. Phys. 70 (1991) 2156 **.
[68] A. Davies, H.G. Craighead, Appl. Phys. Lett. 64 (1994) 2833.
[69] K. Reuter, U. Hohenester, P.L. de Andres, F.J. Garcia-Vidal, F. Flores, K. Heinz, P. Kocevar, Phys. Rev. B 61 (2000) 4522.
[70] L.J. Schowalter, E.Y. Lee, Phys. Rev. B 43 (1991) 9308.
[71] H.D. Hallen, A. Fernandez, T. Huang, J. Silcox, R.A. Buhrman, Phys. Rev. B 46 (1992) 7256.
[72] A. Fernandez, H.D. Hallen, T. Huang, R.A. Buhrman, J. Silcox, Phys. Rev. B 44 (1991) 3428.
[73] A. Fernandez, H.D. Hallen, T. Huang, R.A. Buhrman, J. Silcox, J. Vac. Sci. Technol. B 9 (1991) 590.
[74] W.L. Kaiser, M.H. Hecht, R.W. Fathauer, L.D. Bell, E.Y. Lee, L.C. Davis, Phys. Rev. B 44 (1991) 6546.
[75] H. Sirringhaus, E.Y. Lee, H. von Kanel, J. Vac. Sci. Technol. B 12 (1994) 2629.
[76] M.D. Stiles, D.R. Harmann, J. Vac. Sci. Technol. B 9 (1991) 2394.
[77] T. Meyer, D. Migas, L. Miglio, H. von Kanel, Phys. Rev. Lett. 85 (2000) 1520; H. Sirringhaus, E.Y. Lee, H. von Kanel, Phys. Rev. Lett. 73 (1994) 577 ***.
[78] T. Meyer, H. Sirringhaus, H. von Kanel, Thin Solid Films 318 (1998) 195.
[79] E.Y. Lee, H. Sirringhaus, H. von Kanel, Phys. Rev. B 50 (1994) 5807.
[80] H. von Kanel, E.Y. Lee, H. Sirringhaus, U. Kafader, Thin Solid Films 267 (1995) 89.
[81] H. Sirringhaus, T. Meyer, E.Y. Lee, H. von Kanel, Phys. Rev. B 53 (1996) 15944 **.
[82] H. von Kanel, T. Meyer, H. Sirringhaus, Jpn. J. Appl. Phys. 37 (1998) 3800 **.
[83] M.D. Stiles, D.R. Hamann, Phys. Rev. Lett. 66 (1991) 3179.

[84] D.K. Guthrie, L.E. Harrell, G.N. Henderson, P.N. First, T.K. Gaylord, E.N. Glytsis, R.E. Leibenguth, Phys. Rev. B 54 (1996) 16972.
[85] D.L. Smith, E.Y. Lee, V. Narayanamurti, Phys. Rev. Lett. 80 (1998) 2433 ∗∗∗.
[86] L.D. Bell, Phys. Rev. Lett. 77 (1996) 3893 ∗.
[87] L.D. Bell, J. Vac. Sci. Technol. A 15 (1997) 1358.
[88] P.M. Solomon, S.L. Wright, C. Lanza, Superlattices Microstruct. 2 (1986) 521.
[89] E.E. Mendez, E. Calleja, C.E.T.G. da Silva, L.L. Ghang, W.I. Wang, Phys. Rev. B 33 (1986) 7368.
[90] H.C. Liu, Appl. Phys. Lett. 51 (1987) 1019.
[91] Z.S. Gribnikov, O.E. Raichev, Soc. Phys. Semicond. 23 (1989) 1344.
[92] C. Girardin, R. Coratger, R. Pechou, F. Ajustron, J. Beauvillain, J. Phys. III France 6 (1996) 661.
[93] M.K. Weilmeier, W.H. Rippard, R.A. Buhrman, Phys. Rev. B 59 (1999) R2521 ∗∗.
[94] F.J. Garcia-Vidal, P.L. de Andres, F. Flores, Phys. Rev. Lett. 76 (1996) 807.
[95] K. Reuter, P.L. de Andres, F.J. Garcia-Vidal, D. Sestovic, F. Flores, K. Heinz, Phys. Rev. B 58 (1998) 14036 ∗.
[96] L.D. Bell, M.H. Hecht, W.J. Kaiser, L.C. Davis, Phys. Rev. Lett. 64 (1990) 2679.
[97] W.H. Rippard, R.A. Buhrman, Phys. Rev. Lett. 84 (2000) 971.
[98] H. Sirringhaus, E.Y. Lee, H. von Kanel, Phys. Rev. Lett. 74 (1995) 3999 ∗∗∗.
[99] A. Davies, J.G. Couillard, H.G. Craighead, Appl. Phys. Lett. 61 (1992) 1040.
[100] A. Olbrich, J. Vancea, F. Kreupl, H. Hoffmann, J. Appl. Phys. 83 (1998) 358.
[101] E.Y. Lee, H. Sirringhaus, H. von Kanel, Surf. Sci. Lett. 314 (1994) L823.
[102] A.M. Milliken, S.J. Manion, W.J. Kaiser, L.D. Bell, M.H. Hecht, Phys. Rev. B 46 (1992) 12826.
[103] U. Hohenester, P. Kacevar, P. de Andres, F. Flores, Phys. Stat. Sol. (b) 204 (1997) 397.
[104] B.A. Morgan, K.M. Ring, K.L. Kavanagh, A.A. Talin, R.S. Williams, T. Yasuda, T. Yasui, Y. Segawa, J. Vac. Sci. Technol. B 14 (1996) 1238.
[105] J.G. Nunes, N.M. Amer, Appl. Phys. Lett. 63 (1993) 1851.
[106] M.W. Prins, R. Jansen, H. van Kempen, Phys. Rev. B 53 (1996) 8105.
[107] L.O. Olsson, C.B.M. Andersson, M.C. Hakansson, J. Kanski, L. Ilver, O.U. Karlsson, Phys. Rev. Lett. 76 (1996) 3626.
[108] J. Smoliner, C. Eder, Phys. Rev. B 57 (1998) 9856.
[109] J. Smoliner, R. Heer, C. Eder, Appl. Phys. A 66 (1998) S117.
[110] E.Y. Lee, Phys. Rev. B 59 (1999) 15332.
[111] E.Y. Lee, V. Narayanamurti, D.L. Smith, Phys. Rev. B 55 (1997) R16033.
[112] S. Bhargava, Ph.D. Dissertation, University of California at Santa Barbara, August 1998.
[113] M.H. Hecht, L.D. Bell, W.J. Kaiser, F.J. Grunthaner, Appl. Phys. Lett. 55 (1989) 780.
[114] G.M. Vanalme, L. Goubert, R.L.V. Meirhaeghe, F. Cardon, P.V. Daele, Semicond. Sci. Technol. 14 (1999) 871.
[115] C. Detavernier, R.L.V. Meirhaeghe, R. Donaton, K. Maex, F. Cardon, J. Appl. Phys. 84 (1998) 3226.
[116] J.L. Everaert, R.L.V. Meirhaeghe, W.H. Laflere, F. Cardon, Semicond. Sci. Technol. 10 (1995) 504.
[117] G.M. Vanalme, R.L.V. Meirhaeghe, F. Cardon, P.V. Daele, Semicond. Sci. Technol. 12 (1997) 907.
[118] L. Stockman, H. van Kempen, Surf. Sci. 408 (1998) 232.
[119] I.M. Dharmadasa, C.J. Blomfield, C.G. Scott, R. Coratger, F. Ajustron, J. Beauvillain, Solid State Electron. 42 (1998) 595.
[120] H. Sirringhaus, T. Meyer, E.Y. Lee, H. von Kanel, Surf. Sci. 357–358 (1996) 386.
[121] Y. Hasegawa, K. Akiyama, M. Ono, S.-J. Kahng, Q.K. Xue, K. Nakayama, T. Hashizume, T. Sakurai, Appl. Phys. Lett. 75 (1999) 3668 ∗.
[122] M.K. Weilmeier, W.H. Rippard, R.A. Buhrman, Phys. Rev. B 61 (2000) 7161.
[123] M. Prietsch, R. Ludeke, Phys. Rev. Lett. 66 (1991) 2511.
[124] H.D. Hallen, A. Fernandez, T. Huang, R.A. Buhrman, J. Silcox, J. Vac. Sci. Technol. B 9 (1991) 585.
[125] X. Qiu, G. Shang, C. Wang, C. Bai, Appl. Phys. A 66 (1998) S91.
[126] G.N. Henderson, T.K. Gaylord, E.N. Glytsis, P.N. First, W.J. Kaiser, Solid State Commun. 80 (1991) 591.
[127] R. Coratger, C. Girardin, J. Beauvillain, I.M. Dharmadasa, A.P. Samanthilake, J.E.F. Frost, J. Appl. Phys. 81 (1997) 7870.

[128] B.A. Morgan, K.M. Ring, K.L. Kavanagh, A.A. Talin, R.S. Williams, T. Yasuda, T. Yasui, Y. Segawa, J. Appl. Phys. 79 (1996) 1532.

[129] R. Coratger, F. Ajustron, J. Beauvillain, I.M. Dharmadasa, C.J. Blomfeld, K.A. Prior, J. Simpson, B.C. Cavenett, Phys. Rev. B 51 (1995) 2357.

[130] L.D. Bell, W.J. Kaiser, S.J. Manion, A.M. Milliken, R.W. Fathauer, W.T. Pike, Phys. Rev. B 52 (1995) 12,081.

[131] C.G. Van de Walle, R.M. Martin, Phys. Rev. B 34 (1986) 5621.

[132] Mao-long Ke, D.I. Westwood, C.C. Matthai, R.H. Williams, Surf. Sci. 352–354 (1996) 861.

[133] Mao-long Ke, D.I. Westwood, C.C. Matthai, B.E. Richardson, R.H. Williams, J. Vac. Sci. Technol. B 14 (1996) 2786.

[134] S. Bhargava, H.-R. Blank, V. Narayanamurti, H. Kromer, Appl. Phys. Lett. 70 (1997) 759.

[135] X.-C. Cheng, T.C. McGill, J. Vac. Sci. Technol. B 16 (1998) 2291.

[136] S.D. Lester, F.A. Ponce, M.G. Craford, D.A. Steigerwald, Appl. Phys. Lett. 66 (1995) 1249.

[137] L.D. Bell, R.P. Smith, B.T. McDermott, E.R. Gertner, R. Pittman, R.L. Pierson, G.L. Sullivan, Appl. Phys. Lett. 72 (1998) 1590.

[138] S.-H. Wei, A. Zunger, Appl. Phys. Lett. 56 (1990) 662.

[139] S.-H. Wei, D.B. Laks, A. Zunger, Appl. Phys. Lett. 62 (1993) 1937.

[140] Y. Zhang, A. Mascarenhas, P. Ernst, F.A.J.M. Driessen, D.J. Friedman, C. Geng, F. Scholz, H. Schweizer, J. Appl. Phys. 81 (1997) 6365.

[141] M.C. DeLong, D.J. Mowbray, R.A. Hogg, M.S. Skolnick, J.E. Williams, K. Meehan, S.R. Kurtz, J.M. Olson, R.P. Schneider, M.C. Wu, M. Hopkinson, Appl. Phys. Lett. 66 (1995) 3185.

[142] P. Ernst, C. Geng, F. Scholz, H. Schweizer, Y. Zhang, A. Mascarenhas, Appl. Phys. Lett. 67 (1995) 2347.

[143] B.T. McDermott, K.G. Reid, N.A. El-Masry, S.M. Bedair, W.M. Duncan, X. Yin, F.H. Pollak, Appl. Phys. Lett. 56 (1990) 1172.

[144] G.B. Stringfellow, G.S. Chen, J. Vac. Sci. Technol. B 9 (1991) 2182.

[145] D.J. Friedman, J.G. Zhu, A.E. Kibber, J.M. Olson, J. Moreland, Appl. Phys. Lett. 63 (1993) 1774.

[146] S.R. Kurtz, J. Appl. Phys. 74 (1993) 4130.

[147] S.H. Kwok, P.Y. Yu, K. Uchida, Phys. Rev. B 58 (1998) R13395.

[148] T. Kippenberg, J. Krauss, J. Spieler, P. Kiesel, G.H. Dohler, R. Stubner, R. Winkler, O. Pankratov, M. Moser, Phys. Rev. B 60 (1999) 4446.

[149] A. Zunger, private communications.

[150] S.-H. Wei, A. Franceschetti, A. Zunger, Phys. Rev. B 51 (1995) 13,097.

[151] S. Sakai, Y. Ueta, Y. Terauchi, Jpn. J. Appl. Phys. 32 (1993) 4413.

[152] M. Kondow, K. Uomi, K. Hosomi, T. Mozume, Jpn. J. Appl. Phys. 33 (1994) L1056.

[153] S.-H. Wei, A. Zunger, Phys. Rev. Lett. 76 (1996) 664.

[154] J. Salzman, H. Temkin, Mater. Sci. Eng. B 50 (1997) 148.

[155] W.G. Bi, C.W. Tu, Appl. Phys. Lett. 70 (1997) 1608.

[156] M. Kondow, K. Uomi, A. Niwa, T. Kitatani, S. Watahiki, Y. Yazawa, Jpn. J. Appl. Phys. 35 (1996) 1237.

[157] D.J. Friedman, J.F. Geisz, S.R. Kurtz, J.M. Olson, J. Crystal Growth 195 (1998) 409.

[158] H.P. Xin, C.W. Tu, Appl. Phys. Lett. 72 (1998) 2442.

[159] H. Gruning, L. Chen, T. Hartmann, P.J. Klar, W. Heimbrodt, F. Hohnsdorf, J. Koch, W. Stolz, Phys. Stat. Sol. (b) 215 (1999) 39.

[160] S. Francoeur, S.A. Nikishin, C. Jin, Y. Qui, H. Temkin, Appl. Phys. Lett. 75 (1999) 1538.

[161] W. Shan, W. Walukiewicz, J.W. Ager III, E.E. Haller, J.F. Geisz, D.J. Friedman, J.M. Olson, S.R. Kurtz, J. Appl. Phys. 86 (1999) 2349.

[162] J.D. Perkins, A. Mascarenhas, Y. Zhang, J.F. Geisz, D.J. Friedman, J.M. Olson, S.R. Kurtz, Phys. Rev. Lett. 82 (1999) 3312.

[163] T. Mattila, S.-H. Wei, A. Zunger, Phys. Rev. B 60 (1999) R11,245.

[164] N.A. Modine, unpublished.

[165] W. Shan, W. Walukiewicz, J.W. Ager III, E.E. Haller, J.F. Geisz, D.J. Friedman, J.M. Olson, S.R. Kurtz, Phys. Rev. Lett. 82 (1999) 1221.

[166] K. Uesugi, I. Suemune, Jpn. J. Appl. Phys. 36 (1997) L1572.

[167] G. Pozina, I. Ivanova, B. Monemar, J. Thordson, T.G. Andersson, Mater. Sci. Eng. B 50 (1997) 153.
[168] X.-C. Cheng, D.A. Collins, T.C. McGill, J. Vac. Sci. Technol. A 15 (1997) 2063.
[169] J.J. O'Shea, C.M. Reaves, M.A. Chin, S.P. DenBaars, A.C. Gossard, V. Narayanamurti, E.D. Jones, Mat. Res. Soc. Symp. Proc. 417 (1996) 79.
[170] S.L. Feng, J. Krynicki, V. Donchev, J.C. Bourgoin, M. Difortepoisson, C. Brylinski, S. Delage, H. Blanck, S. Alaya, Semicond. Sci. Technol. 8 (1993) 2092.
[171] D.K. Guthrie, P.N. First, T.K. Gaylord, E.N. Glytsis, R.E. Leibenguth, Appl. Phys. Lett. 72 (1998) 374 ∗∗∗.
[172] D.K. Guthrie, P.N. First, T.K. Gaylord, E.N. Glytsis, R.E. Leibenguth, Appl. Phys. Lett. 75 (1999) 283.
[173] C. Eder, J. Smolimer, R. Heer, G. Strasser, E. Gornic, Physica E 2 (1998) 850.
[174] J. Smoliner, R. Heer, G. Strasser, Phys. Rev. B 60 (1999) R5137 ∗.
[175] C. Rauch, G. Strasser, K. Unterrainer, W. Boxleitner, E. Gornik, Phys. Stat. Sol. (b) 204 (1997) 393.
[176] H. von Kanel, T. Meyer, H. Sirringhaus, J. Crystal Growth 175–176 (1997) 340.
[177] J. Smoliner, C. Eder, G. Strasser, E. Gornic, Phys. Stat. Sol. (b) 204 (1997) 386.
[178] D.I. Westwood, Mao-long Ke, F. LeLarge, F. Laruelle, B. Etienne, Surf. Sci. 352–354 (1996) 802.
[179] F. Hatami, N.N. Ledentsov, M. Grundmann, J. Bohrer, F. Heinrichsdorff, M. Beer, D. Bimberg, S.S. Ruvimov, P. Werner, U. Gosele, J. Heydenreich, U. Richter, S.V. Ivanov, B.Ya. Meltser, P.S. Kop'ev, Zh.I. Alferov, Appl. Phys. Lett. 67 (1995) 656.
[180] B.R. Bennett, R. Magno, B.V. Shanabrook, Appl. Phys. Lett. 68 (1996) 505.
[181] C.-K. Sun, G. Wang, J.E. Bowers, B. Brar, H.-R. Blank, H. Kroemer, M.H. Pilkuhn, Appl. Phys. Lett. 68 (1996) 1543.
[182] C.V. Reddy, V. Narayanamurti, J.H. Ryou, U. Chowdhury, R.D. Dupuis, Appl. Phys. Lett. 77 (2000) 1167.
[183] T. Kinno, K. Tanaka, K. Mizushima, Phys. Rev. B 56 (1997) R4391.
[184] W.H. Rippard, R.A. Buhrman, Appl. Phys. Lett. 75 (1999) 1001 ∗∗.
[185] S.M. Sze, Physics of Semiconductor Devices, 2nd Edition, Wiley, New York, 1981.
[186] D. Landheer, Y. Tao, D.X. Xu, G.I. Sproule, D.A. Buchanan, J. Appl. Phys. 78 (1995) 1818.
[187] E. Cartier, J.C. Tsang, M.V. Fischetti, D.A. Buchanan, Microelectron. Eng. 36 (1997) 103.
[188] R.W. Keyes, The Physics of VLSI Systems, Addison-Wesley, New York, 1987.
[189] M. Dahle-Prietsch, I. Manke, T. Kalka, H.J. Wen, G. Kaindl, J. Phys. D: Appl. Phys. 30 (1997) L48.
[190] R. Ludeke, A. Bauer, E. Cartier, J. Vac. Sci. Technol. B 13 (1995) 1830 ∗∗.
[191] B. Kaczer, H.-J. Im, J.P. Pelz, J. Vac. Sci. Technol. B 16 (1998) 2302.
[192] L. Quattropani, I. Maggio-Aprile, P. Niedermann, O. Fisher, Phys. Rev. B 57 (1998) 6623.
[193] H.J. Wen, R. Ludeke, D.M. Newns, S.H. Lo, J. Vac. Sci. Technol. A 15 (1997) 784.
[194] M.T. Cuberes, A. Bauer, H.J. Wen, M. Prietsch, G. Kaindl, Appl. Phys. Lett. 64 (1994) 2300.
[195] C. Arcangeli, S. Ossicini, O. Bisi, Surf. Sci. 269–270 (1992) 743.
[196] V.P. LaBella, L.J. Schowalter, J.C.A. Ventrice, J. Vac. Sci. Technol. B 15 (1997) 1191.
[197] V.P. LaBella, Y. Shusterman, L.J. Schowalter, J.C.A. Ventrice, J. Vac. Sci. Technol. A 16 (1998) 1692.
[198] T. Sumiya, T. Miura, S.-I. Tanaka, J. Vac. Sci. Technol. A 16 (1998) 2653.
[199] T. Sumiya, K. Honda, T. Miura, S.-I. Tanaka, J. Appl. Phys. 85 (1999) 941.
[200] B. Kaczer, Z. Meng, J.P. Pelz, Phys. Rev. Lett. 77 (1996) 91.
[201] R. Ludeke, H.J. Wen, E. Cartier, J. Vac. Sci. Technol. B 14 (1996) 2855 ∗.
[202] H.J. Wen, R. Ludeke, A. Schenk, J. Vac. Sci. Technol. B 16 (1998) 2296.
[203] B. Kaczer, H.-J. Im, J.P. Pelz, R.M. Wallace, Appl. Phys. Lett. 73 (1998) 1871.
[204] H.J. Wen, R. Ludeke, J. Vac. Technol. B 15 (1997) 1080.
[205] R. Ludeke, E. Cartier, A. Schenk, Appl. Phys. Lett. 75 (1999) 1407 ∗.
[206] R. Ludeke, A. Schenk, J. Vac. Sci. Technol. B 17 (1999) 1823.